Sample Injector Fabrication and Delivery Method Development for Serial Crystallography using Synchrotrons and X-ray Free Electron Lasers

by

Garrett Charles Nelson

A Dissertation Presented in Partial Fulfillment
Of the Requirements for the Degree
Doctor of Philosophy

Approved November 2015 by the
Graduate Supervisory Committee:

John Charles Spence, Co-Chair
Uwe Juergen Weierstall, Co-Chair
Kevin Edward Schmidt
Oliver Beckstein

ARIZONA STATE UNIVERSITY

December 2015

ABSTRACT

Sample delivery is an essential component in biological imaging using serial diffraction from X-ray Free Electron Lasers (XFEL) and synchrotrons. Recent developments have made possible the near-atomic resolution structure determination of several important proteins, including one G protein-coupled receptor (GPCR) drug target, whose structure could not easily have been determined otherwise (Appendix A). In this thesis I describe new sample delivery developments that are paramount to advancing this field beyond what has been accomplished to date. Soft Lithography was used to implement sample conservation in the Gas Dynamic Virtual Nozzle (GDVN). A PDMS/glass composite microfluidic injector was created and given the capability of millisecond fluidic switching of a GDVN liquid jet within the divergent section of a 2D Laval-like GDVN nozzle, providing a means of collecting sample between the pulses of current XFELs. An oil/water droplet immersion jet was prototyped that suspends small sample droplets within an oil jet such that the sample droplet frequency may match the XFEL pulse repetition rate. A similar device was designed to use gas bubbles for synchronized "on/off" jet behavior and for active micromixing. 3D printing based on 2-Photon Polymerization (2PP) was used to directly fabricate reproducible GDVN injectors at high resolution, introducing the possibility of systematic nozzle research and highly complex GDVN injectors. Viscous sample delivery using the "LCP injector" was improved with a method for dealing with poorly extruding sample mediums when using full beam transmission from the Linac Coherent Light Source (LCLS), and a new viscous crystal-carrying medium was characterized for use in both vacuum and atmospheric environments: high molecular weight Polyethylene Glycol.

DEDICATION

This work is dedicated to my good parents for my upbringing, to my wife for her support and patience, and to my children for the joy they bring me.

ACKNOWLEDGEMENTS

I would like to acknowledge my committee co-chairs Professors John Spence and Uwe Weierstall for their useful suggestions and encouragement throughout this work as well as Professor Bruce Doak for his excellent mentorship in the early stages of my research. I would also like to acknowledge Dr. Daniel James for many valuable discussions and shared beamtime experience, Dr. Michael Heymann for valuable discussions concerning the 3D printed nozzle research, The Max Planck Institute for Medical Research in Heidelberg, Germany for supporting early collaborations with Nanoscribe GmbH, and Chelsie E. Conrad who was particularly helpful during viscous injection development by providing both sample and sample medium preparation.

Early portions of this work were supported by a grant from the Agilent Foundation. Other portions of this work were supported by NSF STC award 1231306 and NIH award GM097463. The ANKA Synchrotron Radiation Facility is acknowledged for providing beam time for X-ray tomography imaging. Serial crystallography experiments were carried out at the Linac Coherent Light Source (LCLS), a national user facility operated by Stanford University on behalf of the U.S. Department of Energy (DOE), Office of Basic Energy Sciences. Correlation studies were carried out at the SPring-8 Angstrom Compact Free Electron Laser (SACLA) in Japan. The high-speed camera was purchased with a grant from the Arizona Technology Enterprises (AzTE) Catalyst program.

TABLE OF CONTENTS

Page

CHAPTER Page

CHAPTER Page

LIST OF FIGURES

Figure Page

Figure Page

Figure Page

1. INTRODUCTION

1.1 X-ray Free Electron Lasers

X-ray free electron lasers (XFEL's) generate extremely powerful X-ray pulses, providing peak intensities that are $10^8 – 10^{10}$ times greater than those of conventional sources (McNeil and Thompson, 2010). The Linac Coherent Light Source (LCLS) at the SLAC National Accelerator Laboratory at Stanford University is currently the most powerful XFEL, delivering approximately 10^{12} photons per pulse at 120 pulses per second with each pulse lasting less than 50 femtoseconds. Other operational facilities include the SPring-8 Angstrom Compact Free Electron Laser (SACLA) facility in Japan and FLASH in Hamburg, Germany. The European X-FEL in Hamburg, Germany, which is projected to be operational in 2016, will feature higher operational energy (17.5 GeV versus 14 GeV at the LCLS) and a maximum pulse delivery rate of 2,700-pulse bunches every 0.1 seconds (effectively 27,000 Hz). Additional XFELs either under construction or in the planning process include major upgrades to FLASH and the LCLS (LCLS II) and new facilities in Switzerland (SwissFEL), Italy, South Korea, and China (McNeil and Thompson, 2010; Schlichting and Miao, 2012).

The application of the XFEL in biological imaging has brought novel methodological advances to protein X-ray crystallography (Spence et al., 2012). This is particularly evident with the development of Serial Femtosecond Crystallography (SFX) (Spence and Doak, 2004; Bogan, 2013). In SFX, injected protein crystals in their mother liquor flow continuously across the pulsed X-ray beam. X-ray shapshot Bragg diffraction patterns of microcrystals lying in random orientations as they flow across the pulsed beam are produced. The multiple occurrences of Bragg diffraction from the same Bragg

reflection from many different crystals of different size must then be added together in software to produce the full reflections required. This is in contrast to conventional X-ray crystallography, where a protein crystal may be cryogenically frozen to mitigate radiation damage while mounted on a goniometer on a loop in front of a synchrotron radiation source. The crystal is slowly rotated through every Bragg condition as data are collected, producing "full" or angle-integrated reflections. These full reflection intensities are proportional to the structure factors, or Fourier Coefficients of change-density in the crystal. Radiation may still damage the sample (Burmeister, 2000; Carugo and Carugo, 2005). Furthermore, the freezing process is suspected to significantly change the structure of the protein being studied (Fraser et al., 2011). There is also the problem that crystals that are large enough to diffract sufficiently using synchrotron radiation (SR) can be difficult to synthesize (Mueller et al., 2007). Hence, many biologically important samples that are too sensitive to freezing and radiation damage and/or too difficult to grow into large crystals cannot be studied by SR (Shapiro et al., 2008) but are suitable for SFX at an XFEL.

XFEL pulses are so brilliant that much smaller crystals may be used (i.e. nanocrystals vs. microcrystals) (Chapman et al., 2011; Boutet et al., 2012). X-ray pulses are so brief in duration that only information about the unperturbed structure in its native environment may be captured before any appreciable X-ray damage occurs (Solem 1986; Neutze et al., 2000). Each individual sample is completely destroyed after providing a useful diffraction pattern in just a single snapshot, and the continuous stream of hydrated crystals along with the repetition rate of the pulses yields large amounts of data from which the structure of the protein can be determined (Kirian, 2012) (Figure 1).

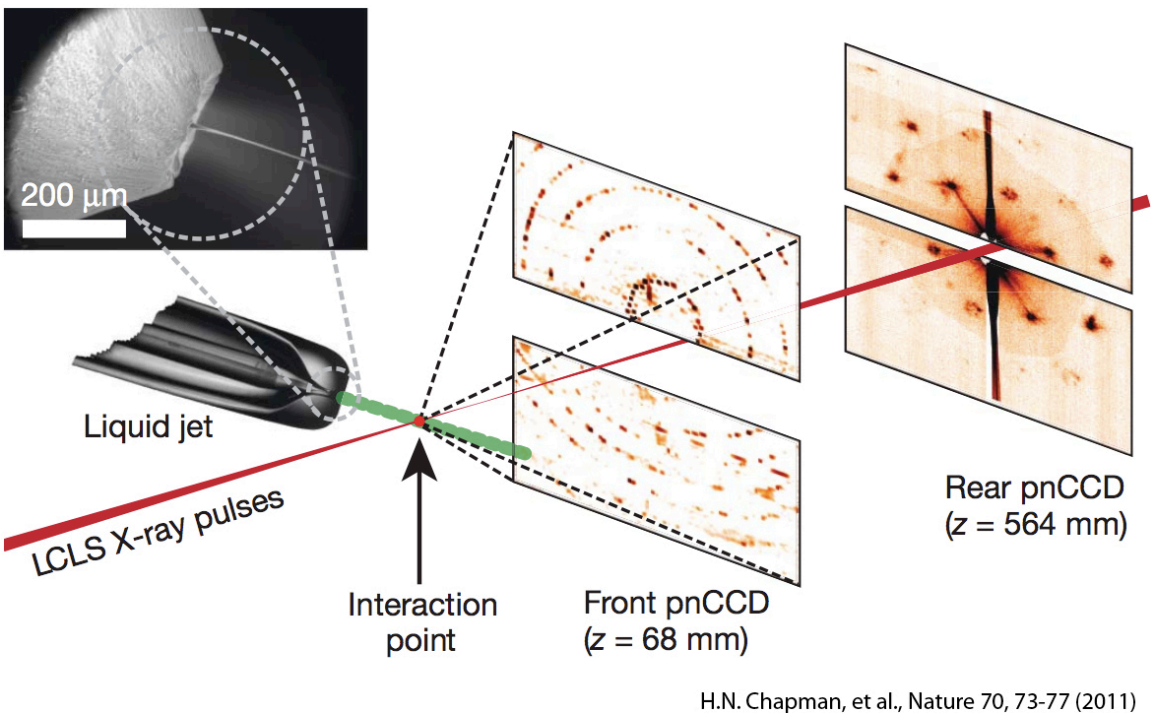

Figure 1: Femtosecond crystallography experiment at the Linac Coherent Light Source (LCLS).

Thus, obtaining high resolution structures from protein nanocrystals of delicate biological samples, including human membrane proteins, is now possible with SFX (Liu et al., 2013). Other reasons for using an XFEL include the higher time-resolution possible when using the pump-probe method for "molecular movies" and the observation of higher resolution data from some proteins.

Continuously transporting millions of environmentally sensitive protein crystals through high vacuum and into the pathway of the X-ray beam is accomplished with either the Gas Dynamic Virtual Nozzle (GDVN) (shown in Figure 1) or the "LCP injector". The X-ray beam hits the randomly dispersed particles by chance, leading to a variable "hit rate" which depends on particle concentration. The objective then is to optimize the

hit rate without clogging the injector. Both of these injectors were originally developed at Arizona State University (ASU) (DePonte et al., 2008; Weierstall et al., 2014) and undergo continuing development at ASU as well as other collaborating institutions.

1.2 Gas Dynamic Virtual Nozzles

The sample delivery requirement for SFX is to use a physical nozzle large enough to avoid clogging by bioparticles, yet fine enough to match the diameter of the X-ray beam focus, which, for example, can be either 0.1, 1, or 10 μm at the CXI hutch at the LCLS. By using a high pressure coaxial gas sheath to speed up a liquid stream, a method of gas focusing is obtained that reduces the diameter of the liquid stream to a much finer size than what is formed at the solid orifice from which it emerges due to shear and pressure forces (Gañán-Calvo, 1998; DePonte et al., 2008). Unlike conventional solid-walled nozzles, the walls that determine the jet diameter of this "virtual" nozzle are replaced by the sheath gas, which can reduce the jet diameter by a factor of 10 or more. Consequently, the GDVN can deliver a steady micron-sized jet of hydrated sample in vacuum for many hours without clogging. Liquid jets of between 2 and 5 μm in diameter are routinely achieved. Submicron jets down to about 0.3 μm in diameter have been demonstrated (DePonte et al., 2011), which are of importance to the development of single-particle imaging methods.

GDVNs commonly consist of one glass capillary situated concentrically inside another (Figure 2). The distal end of the inner capillary is tapered and carefully positioned with respect to converging inner walls near the end of the outer capillary. Protein solution is pressurized and flows through the inner capillary while high-pressure

gas (typically helium) is fed into the interstitial space. The large pressure difference between the inside of the nozzle and the surrounding environment ensures a choked-flow condition at the gas aperture whereby the helium gas undergoes nearly sonic expansion that is largely unaffected by the environmental pressure. Due to mass conservation and the incompressibility of the liquid, the mass flow rate is constant, and the liquid must accelerate. The accelerating liquid jet leaves the end of the outer glass capillary as a freely suspended contiguous stream that stays liquefied even in a high vacuum environment (Doak et al., 2012). It subsequently breaks up into droplets due to the Rayleigh – Plateau instability (Rayleigh, 1879) that can be acoustically triggered (Fig. 2).

Traditional GDVN fabrication begins by melting the end of the outer glass capillary with a flame to form the converging inner profile that chokes the gas flow. The capillary end is then ground with an abrasive polishing disk to create a beveled exterior that allows for wide-angle x-ray diffraction without shadowing the diffracted radiation (bevel was not placed on the nozzle shown in Figure 2). The opposite end of this outer

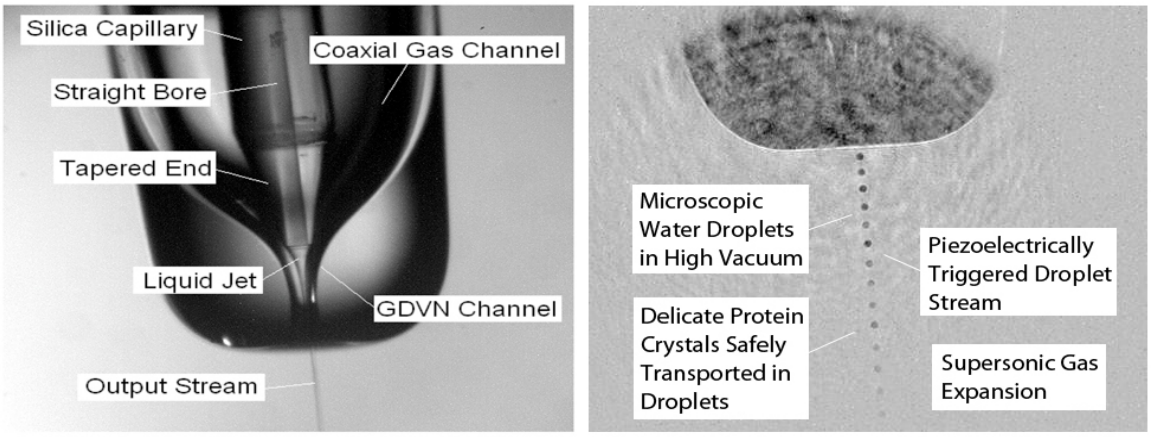

D P DePonte et al 2008 J. Phys. D: Appl. Phys. 41 195505

Figure 2: (Left) Basic components of the current GDVN. (Right) Snapshot of microscopic droplet stream.

capillary is inserted into a 5 cm section of stainless steel tubing and glued in place, such that the gas aperture protrudes from the end by several millimeters. The distal end of the smaller, polyimide-coated, glass capillary is ground into a truncated cone, which is inserted into the outer capillary and carefully positioned. The optimal position of the cone with respect to end of the outer glass capillary can vary from nozzle to nozzle, and so optimization of the axial position is facilitated by use of a system that allows for jetting operation without permanently sealing the inner capillary in place. One method utilizes dual-bore FEP tubing for a reversible cone fitting-based seal of the inner capillary as well as a gas supply capillary. Radial centering of the inner capillary is accomplished either with small, laser-cut Kapton® supports or by using an outer capillary with a square converging internal cross section, into which the round conical tip of the inner capillary self-centers (DePonte et al., 2008; Weierstall et al., 2011).

Jets are sensitive to fabrication asymmetry and alignment inaccuracy. This is especially the case with submicron jets, in which the capillary tip is placed flush with the end of the gas aperture. In this high-shear region, asperities on the tip of the ground cone may act as meta-stable detachment points, leading to instability as the jet switches from one detachment point to another. Off-axis jetting is also an effect in this situation. Both of these effects can be present in micron-sized jets as well, presumably due to asymmetry in the outer gas aperture and/or misalignment. Off-axis jetting can lead to ice forming where the off-axis stream hits a nearby wall and grows back along the stream until the nozzle is rendered inoperable. Furthermore, ice is a problem for sensitive detection equipment. If the intensity of the X-ray beam is maximized for a weakly diffracting

sample, the sudden introduction of strongly diffracting ice can cause damage to the detector. Sample-specific fluid properties can exacerbate all of these effects.

Improvements to these problems have been demonstrated. For example, to eliminate the problem of asperities on the ground inner capillary tip, the conical end of the inner capillary can be specially modified so that the liquid exits from the side of the capillary directly onto the face of the cone, traveling along the edge of the cone, and leaving the capillary from a single sharp point at the front. The geometry is roughly like that of a hypodermic needle made symmetric about the tip. This results in a stream that is very stable and that is centered (Weierstall et al., 2011).

However, even with this very creative solution the fabrication methods described above lack the reproducibility, design versatility, and capacity for rapid prototyping necessary to achieve the aims of ongoing nozzle development, e.g. micromixing and on-demand delivery for reduction of protein consumption. For this reason, alternative microfabrication techniques were explored.

1.3 Microfabrication Techniques

Automation has been extensively developed in traditional crystallography using SR. However the vision of SFX at XFEL facilities as a similar streamlined user experience cannot be realized until all major components of SFX experimentation become automated. Sample delivery is one of these components. The careful flame polishing, grinding, alignment, and optimization described above are tedious and time-consuming. Stable and straight submicron sized jets require especially finely tuned fabrication and yield is typically low. Specific jetting characteristics are difficult to

reproduce. High fidelity, automated fabrication using modern microfabrication techniques could provide an ideal solution to these problems.

Soft lithography, which is a highly developed method, offers the ability to pattern arrays of high-resolution structures on a wafer to produce a mold from which hundreds of devices can be formed in a matter of hours (Qin et al., 2010). Complex features in 2 dimensions up to about 1-μm resolution can be realized, opening up the possibility for incorporating new nozzle features, such as sample conserving systems. Higher resolution, if needed, is possible with e-beam lithography. One drawback for the application of soft lithography to the GDVN is it's planar nature. The GDVN tube-within-tube cylindrical geometry is not well adapted to planar lithography. At first glance, the 3-dimensional internal complexity of the GDVN suggests that such GDVN profiles are only amenable to special methods in soft lithography. In particular, the functionality of the inner capillary profile near the focusing region is difficult to introduce using standard photolithography, since such methods can only produce complex profiles in 2D. But there are variations of soft lithography that provide limited 3D variation. These include multilayer lithography and inclined lithography, both of which were explored in this work.

This thesis reports the investigation of standard soft lithography in a "composite" fabrication approach that combined both traditional GDVN structures as well as polydimethylsiloxane (PDMS) structures fabricated using soft lithography. Basic GDVN functionality as published by the author (Doak et al., 2012) as well as new functionality are reported using this approach. This manuscript also reports prototyping for devices made with only PDMS using multilayer lithography and inclined lithography. Results

from multilayer lithography were not initially unfavorable and therefore prompted the more complicated inclined lithography approach, which required adaptations to existing cleanroom equipment, more thoughtful photomask design, and special water immersion inclined lithography techniques (Sato et al., 2006). In the course of the soft lithography research laid out in this manuscript an all-PDMS soft lithography GDVN was also realized elsewhere (Trebbin et al., 2014).

Building upon the work of Trebbin and associates, an additional sample-conserving technique was prototyped that makes use of water droplets immersed within an oil jet as means of conserving sample by matching droplet frequency with the pulse repetition rate of the XFEL beam. Another device was prototyped that makes use of the same principle, except with gas bubbles injected for segregating the sample in a periodic fashion to match pulse repetition rate. This device also makes use of inline bubble mixing chambers to simultaneously act as a micromixer.

A remaining potential drawback of the soft lithography approach is the durability of the bonding interfaces between PDMS and itself as well as between PDMS and other materials in the presence of the high and low pressures inherent in GDVN operation. An essential characteristic of the GDVN delivery method is continuous, reliable operation under this pressure duress. To the knowledge of the author, no SFX experiments using a PDMS GDVN have been reported. In an approach from another experimental group, injection molding and sintering has been used to form a strong, high-resolution ceramic outer gas aperture (Beyerlein et al., 2015). However, injection molding of a single unit containing both internal and external parts of the GDVN has not been demonstrated and may be difficult to achieve.

It is desirable to have both the complexity found in the soft lithography method and the robustness found in the injection molding approach. 3D printing has held the promise of achieving complexity in 3 dimensions in robust materials for some time, but has in the past not been able to match the resolution found in lithography within a reasonable writing time. However, this is no longer the case when using recent commercial writing developments with 2-Photon Polymerization (2PP). 3D printing utilizing 2PP technology offers submicron resolution. With reasonable writing time, 2PP 3D printing has the potential to not only "stream-line" GDVN fabrication, but to bring about the realization of functionality in SFX sample delivery not currently achievable in any other way. In this work is reported the successful use of 2PP 3D printing to generate reproducible GDVN's. All critical GDVN components are printed in a single process at high resolution within hours. Results from use of the nozzles in serial crystallography experiments are reported.

1.4 Viscous Medium Extrusions

When using a GDVN at XFEL facilities currently in operation, sample waste is high. Flow rates for the GDVN range from about 1 to 20 μL/min, depending on the properties of the liquid medium and the specific GDVN geometry. For a 1 μm-sized liquid jet traveling at 10 m/s (typical) across the pathway of a beam with 120 Hz pulses and a beam focus of 1μm, only about 0.004% of the sample medium is illuminated. Therefore, 99.996 % of sample runs to waste. In fact, appreciable percentages of sample are illuminated only when data collection reaches the MHz range. With the European XFEL soon to offer 2,700-pulse bunches every 0.1 seconds (effectively 27,000 Hz), the

problem with sample waste in the GDVN may soon be substantially reduced with at one facility. In fact, in this case the high speed of the GDVN may be necessary. However, operation at ~100 Hz will remain the best available option at most XFEL facilities. Consequently, sample-conserving alternatives to the current GDVN operation are and likely will continue to be of interest. One of these alternatives is viscous medium extrusion of the "toothpaste" or "LCP injector".

In 2013, the "LCP Injector" was used to solve the room temperature structure of a human serotonin receptor at the LCLS using just 300 μg of protein with flow rates between 50 and 200 nL/min (Liu et al., 2013). Details of the development and operating principles of this viscous extrusion injector are reported elsewhere (Wang, 2014; James, 2015*). Results from the author's co-authored publication on viscous injection in serial crystallography that are not included in the main body of the text are summarized in Appendix A*. These include serial crystallography experiments that resulted in room-temperature structures of 1) human G Protein-Coupled Receptors (GPCRs) using LCP as the delivery medium at the LCLS: the 2.8-Å resolution structure the serotonin 5-HT_{2B} receptor bound to the agonist ergotamine (Liu et al., 2013) and the 2.9-Å resolution structure of the angiotensin II type 1 receptor, AT_1R, in complex with its selective antagonist ZD7155 (Zhang et al., 2015); 2) bacteriorhodopsin at 2.4-Å resolution using LCP as the delivery medium at the ESRF synchrotron microfocus beamline (Nogly et al., 2015); 3) phycocyanin at 2.5-Å resolution and using agarose as an alternative crystal-carrying medium at the LCLS (Conrad et al., 2015); and 4) 40-Å resolution data (not complete structure) from crystals of the Sindbis virus, an enveloped icosahedral RNA

virus with 700 A˚ diameter, delivered in agarose at the LCLS (40-Å is considered high resolution diffraction data for Sindbis) (Lawrence et al., 2015).

Results on viscous extrusion injection in this text will focus on a method for efficient data collection that was developed when using full beam transmission from the LCLS during atmospheric operation (helium-enriched atmosphere) and the development and implementation of an alternative viscous media: high molecular weight Polyethylene Glycol (PEG).

2. SOFT LITHOGRAPHY

2.1 Composite Device

Soft photolithography fabrication techniques were used to replace the outer glass aperture of the GDVN with a polydimethylsiloxane (PDMS) channel with a well-defined 2D profile terminating in a Laval-like nozzle. The most basic of Laval-like profiles was used for the gas aperture design. Figure 3 is a schematic comparison of the previously described glass-based GDVN to this composite version.

The first aim of this composite device was to determine whether or not the planar-like fabrication of single-layer soft lithography was at all compatible with GDVN operation. Of particular notice was the fact that, in contrast to the concentric traditional GDVN structures, the converging section of the PDMS nozzle has only 2-dimensional convergence, resulting in a slit-shaped exit aperture (Figure 3). Of lesser concern, but of significance, was the abrupt perpendicular routing of the focusing gas lines, which was a practical measure to assure that gas supply fittings could be adjusted by hand. The ability to rapidly prototype devices in a reproducible way would facilitate this kind of study.

Secondly, the composite device was made with the aim of exploring jet operation in a subsonic gas expansion. Of particular interest was the effect of droplet spacing. Whereas acceleration of droplets in the breakup region was observed with the near-sonic gas expansion of typical GDVN modes of operation, presumably a subsonic gas expansion would have the effect of decelerating the droplet train in the breakup region. In a situation where the droplets are the targets (usually the contiguous stream just upstream of droplet breakup is the target), deceleration should result in shorter droplet spacing and thereby provide a means of sample conservation by increasing hit probability

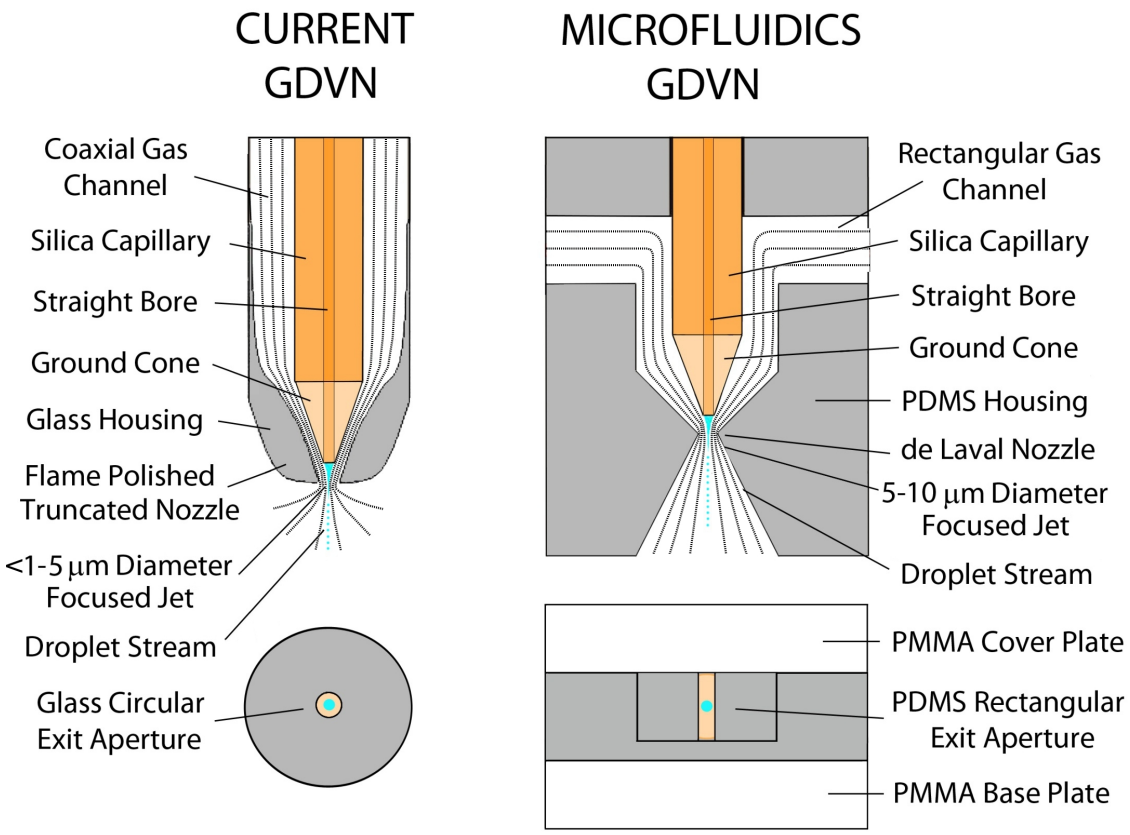

Figure 3: (Left) Current GDVN schematic; (right) microfluidics GDVN schematic.

without changing flow rate. Furthermore, a working understanding of what parameters affect droplet spacing could lead to the ability to tune the spacing for syncing droplets with XFEL pulses.

The first prototypes were successful in terms of basic GDVN operation, and subsonic operation was explored for the first time. However, no deceleration of droplets was observed. The results with the Laval-like profile led to the implementation of a special fast fluid switch for millisecond switching of the freely suspended liquid jet.

2.1.1 Fabrication

Fabrication of the composite devices began with a 2D CAD (AutoCAD 2010, Autodesk, Mill Valley, CA) design of a photomask. The area of the mask is 5 x 5 inches but the actual working area corresponds to a four-inch diameter silicon wafer. As shown in Figure 4, as many as 11 nozzles were worked into a single photomask. For the divergent section of the Laval section, 20°, 40°, and 60° (full angle) varieties were tested, while the convergent section was kept constant. The finished CAD file was sent to a commercial company (Fineline Imaging, Colorado Springs, CO) for production of the actual photomask. Both glass (chrome on soda lime) and Mylar (200 μm thick films) were investigated as mask material. Given the fast prototyping nature of these initial experiments, most of the devices reported here were fabricated using Mylar masks, laser-plotted at 10,160 dpi. Smaller features can be fabricated using higher density plotting on Mylar (up to ~40,000 dpi) or by using the glass masks. For this device (50 μm wide channel width, defined to about +/- 1 μm) the Mylar masks proved adequate.

Working in class 1000 cleanroom, a 4-inch silicon wafer was cleaned with Piranha solution (3:1 concentrated sulfuric acid to 30% hydrogen peroxide solution), then washed with pure water and dried with nitrogen gas. SU-8 2075 negative photoresist (MicroChem) was then spin-coated onto the wafer in 3 separate layers of approximately 120 μm each (final thickness of approximately 360 μm). Each layer was separately cured prior to depositing the subsequent layer. For this thickness, the manufacturer recommends curing for 3 minutes as 65° C then immediately for 9 minutes at 95° C. However, this procedure was found to result in wrinkling of the layer, apparently because the lower strata of photoresist never properly solidified. Wrinkling could be avoided

simply by placing a glass cover (inverted Petri dish) over the film while curing. It may be that curing without the glass cover results in a "skin" forming on the film, which then limits further evaporation of the solvent. Curing was always successful using the glass cover, but never in its absence.

The cured photoresist was covered with the photomask and exposed to near-UV light (~350 nm) for 60 sec. This dosage was not optimized during these initial trials to prevent overexposure, as no appreciable unfavorable effects on the wafer structures were detected. A subsequent post-exposure baking for 15 minutes at 95° C then cross-linked the exposed photoresist. The wafer was next immersed in SU-8 developer to chemically strip the unexposed negative photoresist, leaving behind a raised structure in the form of the "negative" of the desired nozzle channels. The patterned wafer was then "hard-baked" at 150° C for 5 minutes in order to "relax" the photoresist (anneal microscopic cracks remaining from the previous handling). This completed the soft lithography phase of the fabrication. The patterned wafer was then transferred from the clean room to a standard laboratory setting for further handling and use.

To prepare a PDMS wafer stamp, the finished photoresist was first treated with a salinization process to prevent lifting the SU-8 structure from underlying substrate during the molding process. This ½-hour process entailed exposing the finished wafer to a drop of trichlorosilane in a dessicator vessel, while pumping actively for 10 minutes and then valving off the pump but leaving the wafer under the residual vacuum for an additional 20 minutes. PDMS (Sylgard 184) was then prepared at a volumetric mixing ratio of 10:1 (elastomer base to curing agent) and poured onto the wafer.

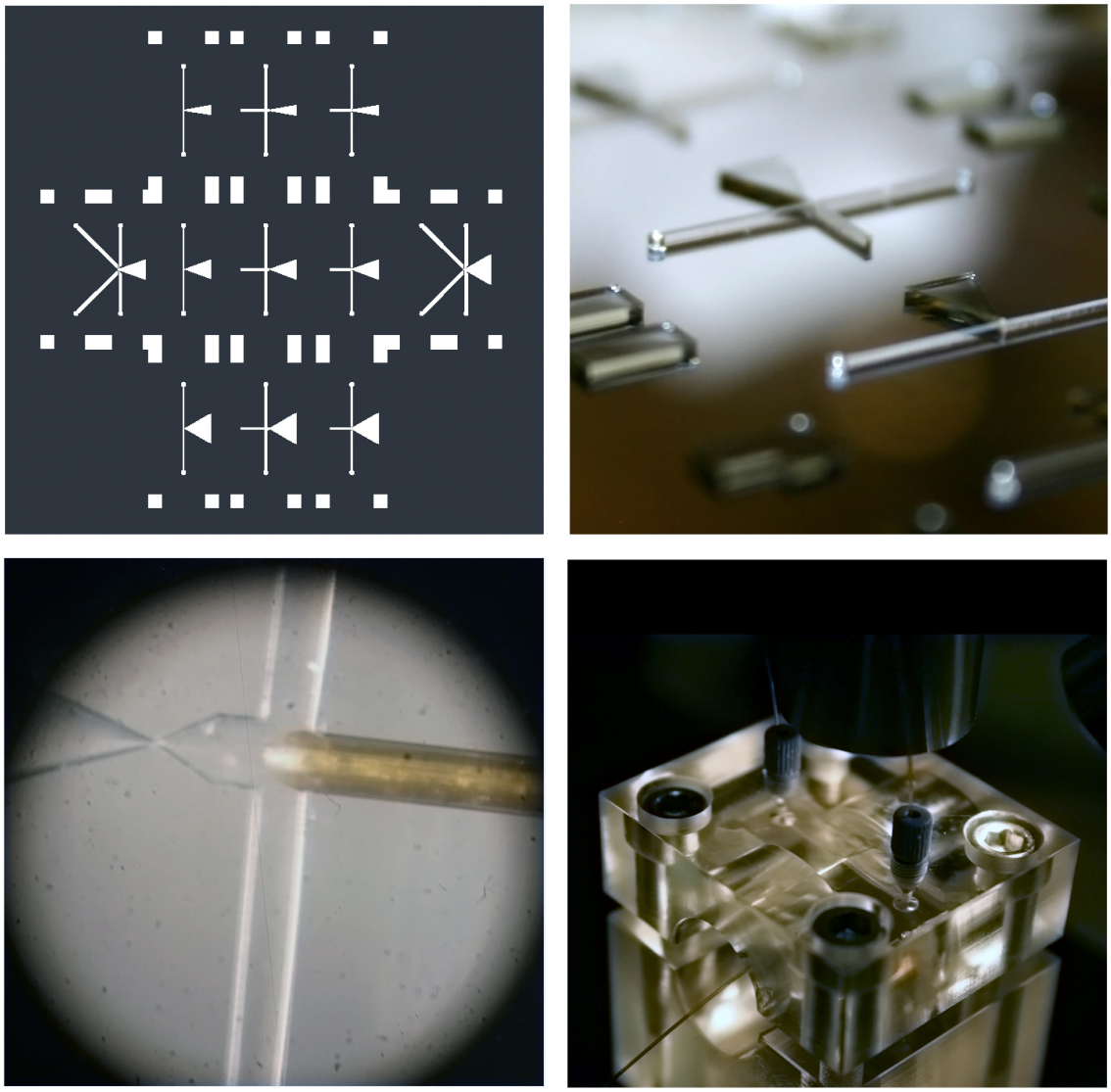

Figure 4: (Clockwise from upper left) AutoCAD photomask design, corresponding SU-8 nozzle structures patterned on silicon wafer, acrylic clamping device with machined receiving ports, installation of glass liquid capillary.

The PDMS was degassed carefully in a stainless steel vacuum chamber pumped by a rotary vane mechanical pump. Slow degassing was essentially to avoid explosive formation of bubbles in the PDMS. In addition, the degassing was continued only to the point of disappearance of all bubbles from the PDMS. Further degassing beyond this point was found to seal the PDMS-coated wafer to the bottom of its container, making it nearly impossible to remove the wafer without cracking it.

The degassed PDMS and wafer were then placed in an oven and baked at 80° C for 4 hours. The platform upon which the wafer sat within the oven was carefully leveled in order to maintain as uniform a thickness of PDMS as possible. The container was then allowed to cool, whereupon the slab of PDMS containing the desired microchannel structure could be peeled off of the wafer.

Both glass and PMMA sheets were tested as covers for the channels. Glass is a common choice for this purpose since it bonds strongly to PDMS after being treated with oxygen plasma, is optically clear, and provides structural rigidity. In standard microfluidics fabrication, the channel structure is often sealed with a glass sheet and attachments for gas and liquid supply are made on the PDMS side using commercial "glue-on" ports (e.g., IDEX Nanoports). Ports constructed in this fashion are able to withstand only low operating pressures however, typically only a few tens of psi. To operate at the higher pressures required for GDVN operation, it is therefore necessary to clamp the PDMS channel structure between robust transparent sheets on both the top (open) and the bottom (closed) sides of the PDMS layer. Since acrylic plastic sheets (PMMA) are flat, optically clear, and can easily be drilled and tapped for threaded ports to receive standard threaded tube fittings, it was therefore chosen for the support structure.

One-half inch thick PMMA sheets were found to supply sufficient structural rigidity. Although PMMA can be plasma-activated for bonding to PDMS, a simple clamping of the PDMS layer between two PMMA slabs was found to serve equally well, with the added advantage that the PDMS layer could then be removed and replaced simply by unclamping the PMMA slabs. The simple PMMA clamping device fabricated for this purpose is shown above in Figure 4. The liquid capillary was inserted from the side with the rubber-like PDMS forming a partial seal. This partial seal was useful, since the liquid capillary could first be adjusted to the optimal position for gas dynamic focusing before being permanently set in place and sealed with a drop of epoxy, which filled the cavity between to capillary and the PMDS channel. Although epoxy does not seal well to PDMS, this was found to be sufficient at all levels of operation.

2.1.2 Operation

Nozzle operation was successfully carried out in both atmosphere and vacuum environments with 100, 50, and 40-μm ID capillaries, focusing as far down as 5 μm. Subsonic GDVN operation was demonstrated for the first time. The theoretical transition from subsonic to supersonic flow occurs when the upstream to downstream pressure ratio reaches 1.89 (helium gas). Jetting was achieved with a ratios ranging from as low as 1.03 to beyond the transition point. (Fewer measurements were taken around the transition point due to shifting of the PDMS). The precise values of these low pressures were measured by routing one of the gas lines to a sensitive electronic pressure sensor for a stagnation pressure reading at the location just before focusing occurs.

Owing to the Coandă effect, the exiting stream tended to follow the sidewalls of the diverging section of the 2-dimensional Laval profile when exhausting into atmosphere. Switching from one sidewall to the other occurred frequently when using the 20° nozzle variety, whereas with the 60° nozzles spontaneous switching was rare. The switching behavior vanished entirely when exhausting into vacuum, during which the jet was remarkably straight. See Figures 5 and 6.

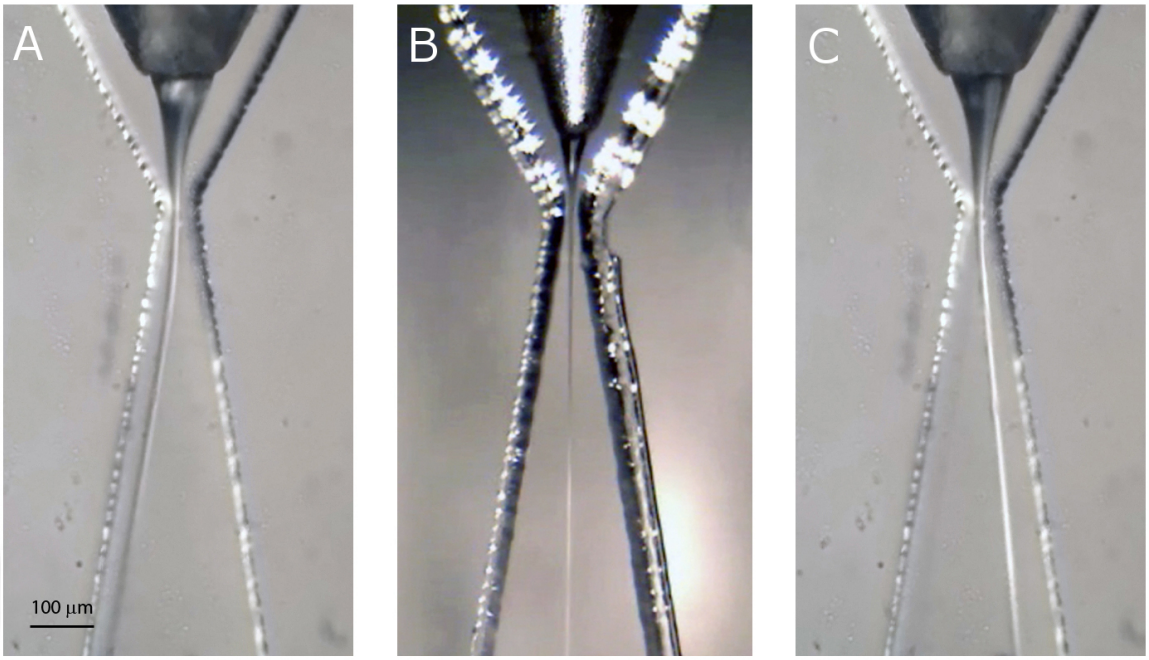

Figure 5: Various operating conditions demonstrated with the composite GDVN. A) and C) 13-µm subsonic jet exhausting into atmosphere and exhibiting sidewall switching. B) 5-µm jet exhausting into vacuum with a straight profile.

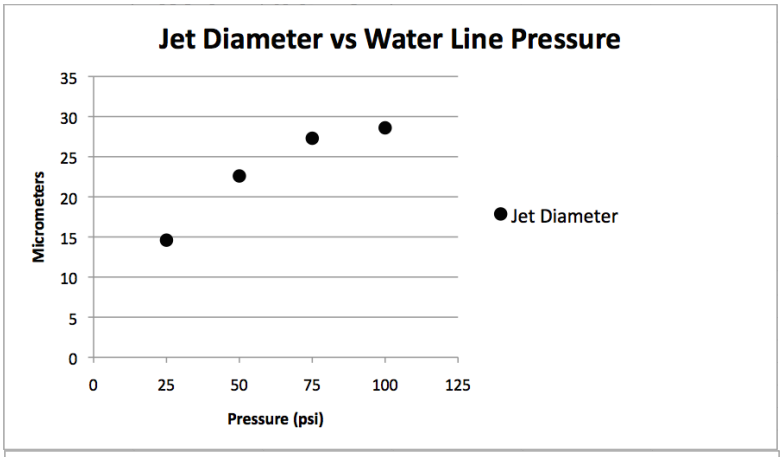

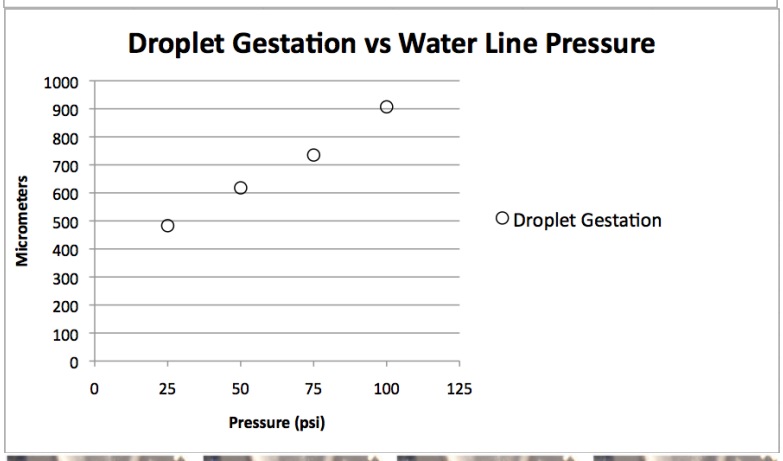

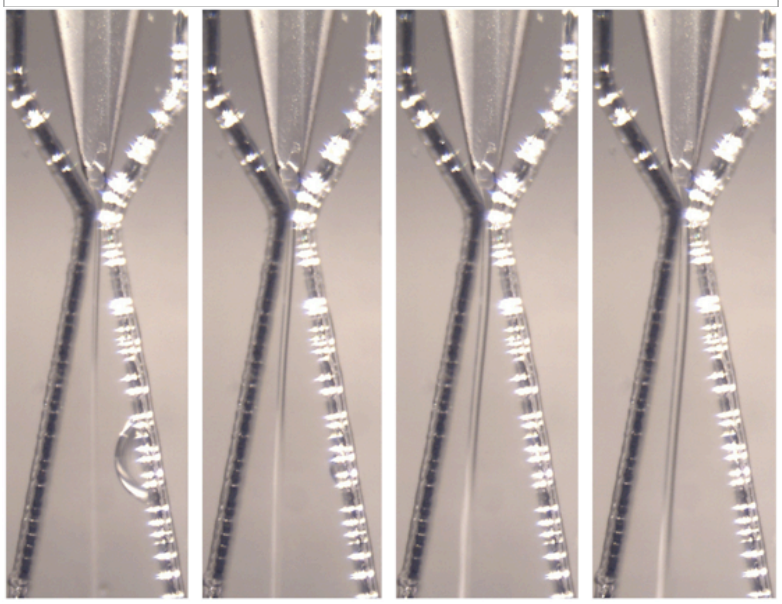

Figure 6: GDVN subsonic operation data for an upstream to downstream helium gas pressure ratio of 1.07 measured at increasing liquid line pressure values and exhausting into atmosphere. Stream diameter and the distance between the glass capillary tip and the point of droplet gestation are plotted. The photographs correspond left to right with the data points and give an idea of subsonic jet behavior at the lowest upstream-to-downstream pressure ratios.

2.2 Fast Fluid Switch

In X-ray investigations of biomolecules using XFELs the biological species of particular interest are available only in minute quantities, often only tens of microliters. Consequently, highly efficient sample injection into the XFEL beam becomes imperative. As mentioned earlier, as much as 99.996% of samples go to waste when using the GDVN. In principle this enormous inefficiency can be alleviated by increasing the XFEL repetition rate, but upcoming XFELs that will offer much higher pulse rates at beam energies comparable to current leading XFELs are very few in number; currently just one facility plans to offer this: the European XFEL. Hence operation at well under 1 kHz will remain a major mode of XFEL use in the foreseeable future. Sample consumption can be reduced significantly through injection based on very high viscosity free-streams, which will be addressed in Chapter 4. But that method has complications of its own, such as much larger jet diameter and limited jetting medium availability. The onus is clearly on the sample injection community to develop improved and much more efficient XFEL injection capabilities, particularly for low viscosity GDVN sample injectors.

Rapid switching of the jet offers routes around these impasses by switched diversion and collection of the unused sample stream in those intervals. The latter possibility is addressed in this section, showing that fluidic switching can be easily incorporated into the microfluidic GDVN technology described earlier, with switching times that are fast relative to the pulse repetition period ($\geq$ 8.33 ms) of current X-ray Free Electron Lasers (XFEL). As shown earlier, with the diverging channel present and when discharging the jet into an atmospheric ambient (as opposed to vacuum), the outgoing liquid jet tended to not flow along the symmetry axis of the diverging channel (i.e.,

equidistant from the two diverging walls), but rather to flow parallel to and slightly removed from one or the other of the two sidewalls. Recognizing the similarity of the divergent channel to the structure of a classical microfluidic switch (Tesař, 2009; Raymond, 1971), it was surmised that this was due to a fluidic switching effect, with the gas flow and entrained liquid jet finding a locally stable flow configuration along one or the other of the two walls instead of at the center of the channel.

In the preceding microfluidic GDVN tests, spontaneous switching of the liquid jet from one sidewall to the other occurred frequently when using nozzles with a 20° diverging channel (as in Figure 5 A and C), whereas with the 60° nozzles spontaneous switching was rare. Accordingly, switching control ports were added to 60° diverging PDMS nozzles, just downstream of the nozzle throat, and 40- and 50-µm inner diameter glass capillaries were used to test switching characteristics. Luer lock style fittings were used to connect disposable syringes to microcapillaries that were then inserted into the new side channels in the same manner as the central liquid capillary from Figure 4 (see Figure 7). With applied pressure on the control ports, it was possible to flip the stream from one sidewall to the other and back again (Figure 7), with the stream remaining stably on either side until shifted back by applying pressure. The underlying fluidic switching derives from the Coandă effect (Reba, 1966), in which a fluid flow can be directed back and forth between one output channel and a second by momentary input of suitable control flows. Although the effect is generally associated with single phase flow (either gas or liquid but not both co-flowing), in this case it is a two-phase flow – specifically, the flow of the GDVN liquid jet immersed in its co-flowing gas – that switches back and forth. In contrast to switching of a pure gas flow, the switching of this

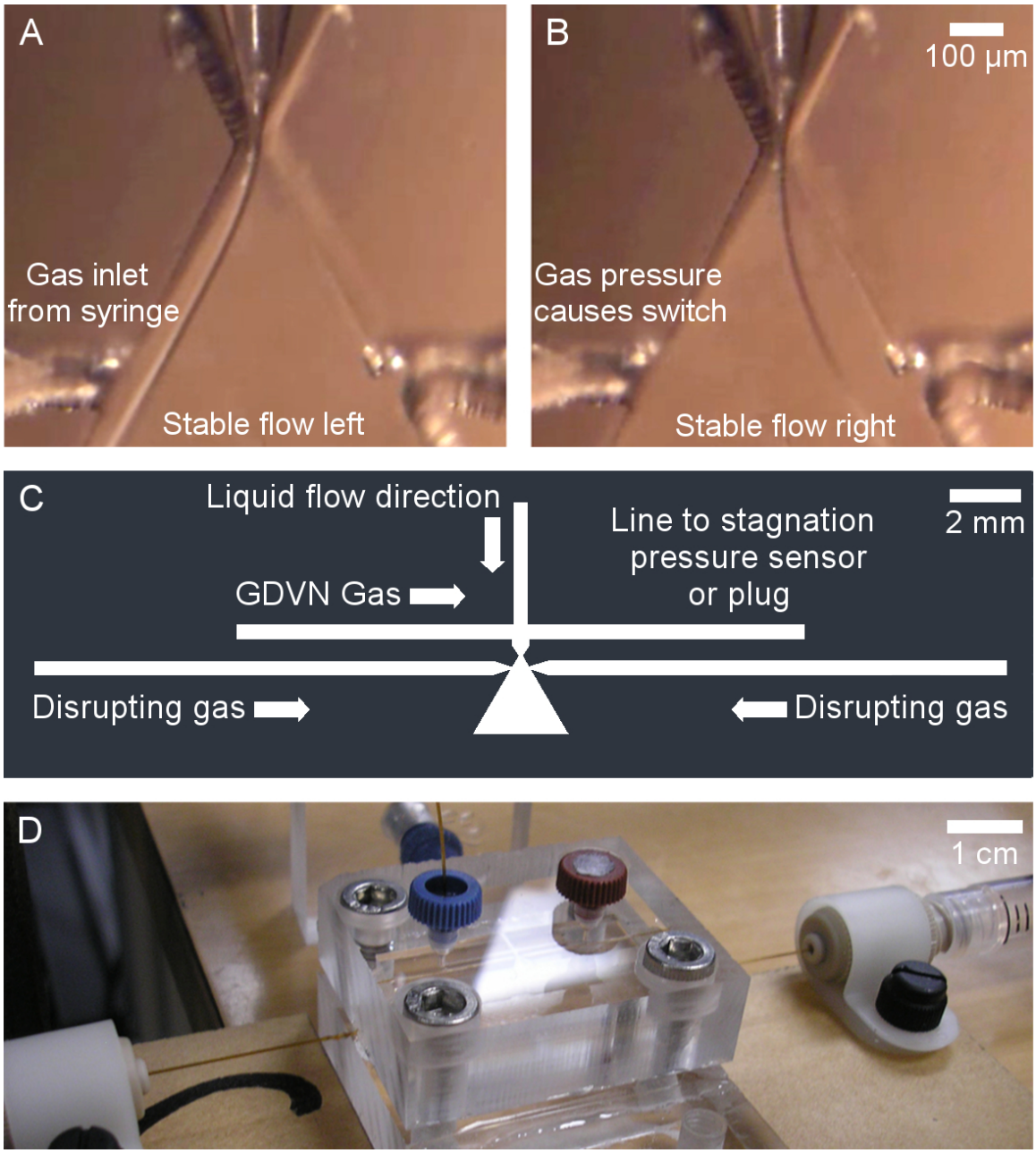

Figure 7: A) Switching device with jet running stably before switch; B) Switching device with jet running stably after switching has occurred. Switching was activated by hand, using the syringes seen in Figure D. Multiple hand-activated switches could be made, back and forth. High speed video indicated that it took about 2 ms to partially displace the jet (presumably by the hand syringe), after which a fast switch occurred in 80 to 220 µs. C) Photomask design for switching device (the various channels are labeled); D) Equipment in use. Syringes (left and right) are used to apply a pressure pulse to induce fluidic switching.

device is therefore quite easily discerned. A typical microfluidics switch has two fully separate and distinct output channels. However, this device clearly demonstrates that no physical separatrix is actually needed to achieve switching in a diverging channel. Switching did not occur immediately upon compression of the syringe plunger (3 mL syringe), but seemed to be delayed by up to 1 second. Partially compressing the syringe had the effect of displacing the jet part-way across the channel but then having it return immediately to its original path. This suggests that a critical pressure must be exceeded for the full switch to occur, and that this pressure lies in the vicinity of that attained by human-hand compression of the 3 mL syringe.

High speed camera footage at frame rates ranging from 1,000 to 100,000 frames per second was recorded to measure the switching time from one sidewall path to the other. Videos taken at 10,000 fps indicated switching times between 700 and 800 μs. In a video taken at 50,000 fps there appeared to be a "creeping" of the jet for about 2.2 milliseconds prior to its eventual jump to the other side, which occurred within just 80 μs. In another video recorded at 100,000 fps this "creeping" lasted for about 1.6 milliseconds, after which full switching transpired within 220 μs. During this fast switching interval, the stream clearly paused for 50 to 60 μs on the symmetry axis of the channel before completing the switch. Such a millisecond-scale "creeping" action always preceded the subsequent microsecond-scale jump.

Whether and how this "creeping" might relate to details of the pressure pulse supplied by syringes is currently unclear. Video footage of the hand-pressurization of syringes on such a small timescale is difficult to interpret. With the perceived 1-second delay between the beginning of syringe compression and the switching event, it seems

likely that several milliseconds are required to achieve the necessary compression by hand. Presumably some time interval is also required for the fluid flow through the channel to rearrange itself to induce and conform to the new jet position. A quick-release valve and pre-pressurized delivery system would help clarify the situation. It could be informative to compare the behavior (it's presence and perhaps the time scale) of the partial displacement of the jet from equilibrium ("creeping") when using a system like this that would both minimize ramping of the pressure and extend the pressure range.

The ability to rapidly switch the liquid jet from one path to another provides a way to conserve sample by delivering it only during an X-ray pulse. Of particular interest in this regard is partial transfer of the jet across the diverging channel upon momentary partial displacement of the syringe plunger. In the manner of standard fluidic switches (Tesař, 2009), the liquid jet could then be directed into a collection vessel except for an appropriate time interval centered on the XFEL pulse arrival time, when it would be flipped temporarily into the X-ray beam. Unused sample would then be collected and recycled through the injection system. This is entirely feasible for injection into an atmospheric environment. Injection into vacuum, by contrast, results in rapid desiccation and denaturing of biomolecular samples, rendering them unfit for any further use. To be useful, the switching method must prove more preferable than simply collecting the sample after X-ray interaction with a catcher. If the residual effects of the X-ray on unused sample are negligible, it may be that switching device is completely unnecessary. Even if this is the case, there may be other applications of the switching jet.

Additional study and development of this technology are clearly required, notably the installation and use of fast, reliable, triggerable control pulses for the fluidic

switching. High-pressure gas electrostatic microvalves with on or off times of 50 μs or less have been developed and are potential candidates for driving the device (Bae, et al., 2007).

2.3 Completely PDMS Device

2.3.1 Overview

Only with a completely PDMS GDVN are the niceties of soft lithography fully realized. For example, microfluidic devices for crystal size sorting have been demonstrated (Abdallah et al., 2013; Abdallah et al., 2015) and could be directly coupled to PDMS GDVN for live sorting of crystals during XFEL operation. For the purpose of preventing detector saturation from the illumination of unanticipated large crystals, integrating the crystal sorter just upstream the GDVN is potentially a fantastic alternative to using a standard inline filter, which may waste most protein that does not pass through the filter. Many other novel designs depend on the absence of the glass capillary that is present in the composite device.

But the functionality of the inner capillary profile near the focusing region is difficult, and perhaps impossible, to introduce using standard single-layered photolithography, since such methods can only produce varying profiles in two dimensions. But there are variations of soft lithography that provide limited three-dimensional variation. Multilayered lithography is perhaps the simplest alternative. However, initially this was though to be inadequate.

In the traditional GDVN the end of the capillary is finely ground so that it terminates in a sharp tip. In early testing of the hybrid GDVN it was thought that the

rectangular geometry of the surrounding PDMS structure in the focusing region might not be compatible with the cone shape of the central glass capillary. The ends of some of the capillaries were therefore given a wedge profile to match the sidewalls of the PDMS aperture. Specifically, a 100-µm inner diameter / 360-µm outer diameter capillary was used for the wedge profile test. In these initial tests water collected along the wedge planes, appearing stagnate, and no jetting occurred at all after cycling throughout the typical ranges of operating pressures. The standard coned design was used instead and worked well, and was used in the work reported in section 2.1 and 2.2. When approaching the fabrication of a completely PDMS GDVN, recollection of the results with this wedged capillary profile prompted pursuit of alternative lithography approaches instead of the multilayered approach. Grayscale lithography was considered but not pursued since it is said to be limited to low contrast resists, which may not be suitable for GDVN fabrication. Inclined lithography (Han et al., 2004), showing more promise, was pursued.

Inclined lithography alone is somewhat limited when it comes to the angle that can be achieved due to the sequence of refractive indices of materials the incident light experiences as it propagates. However by using a water immersion technique (Sato et al., 2006), this problem was bypassed. Preliminary devices were made and tested.

In April of 2013 an attempt was made to further verify that a simpler design using multilayer lithography is not a feasible approach. The wedge capillary design in the glass-based GDVN was retested with a 50-µm ID capillary. The grinding was done quite carefully to assure that the front face of the capillary was just more than 50 µm across as seen in Figure 8 (making the wedge too sharp would have resulted in a parabolic opening

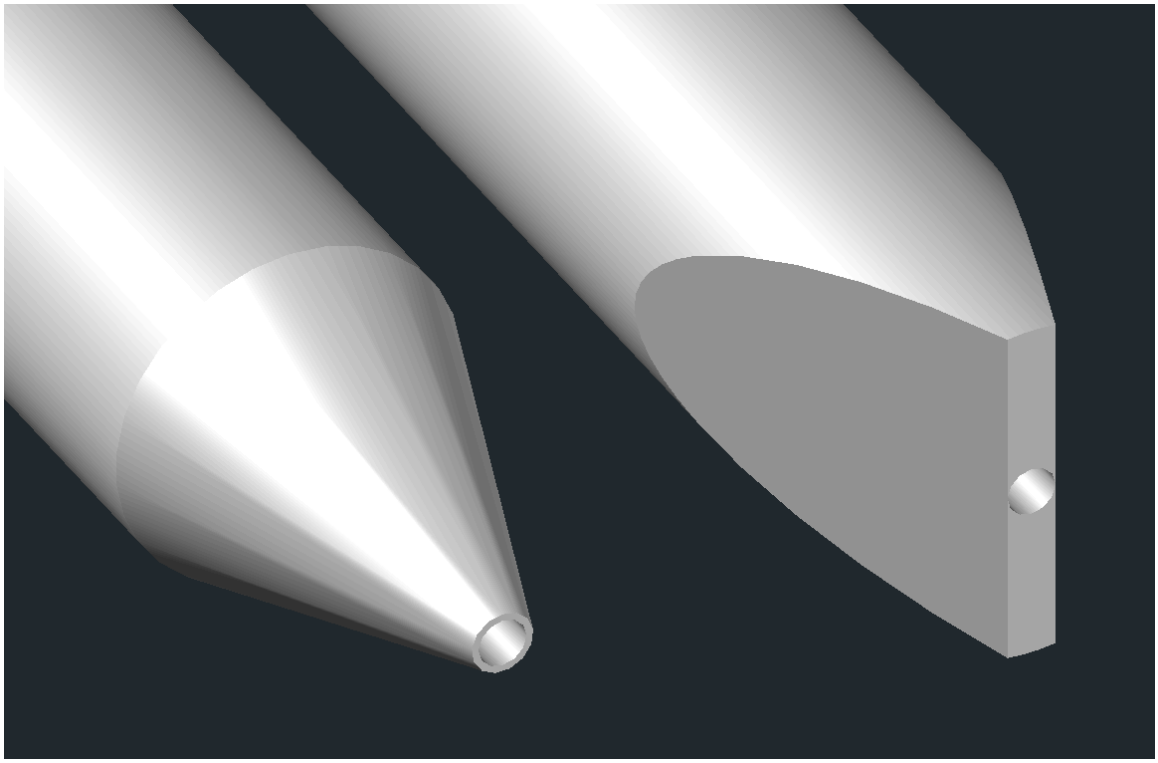

Figure 8: (Left) Cone profile type for central glass capillary used in the glass-based GDVN and the composite microfluidic GDVN. Right: Wedge profile type used in first and second phases of feasibility testing of the multilayer lithography approach to a PDMS-only GDVN.

to the side instead of a sharp edge). Contrary to prior tests, it was found that jetting did occur, although with a much higher liquid line pressure requirement for initiating the jet. Multiplayer lithography devices were fabricated, but were not initially successful. The use of 2PP 3D printing as an alternative means of wafer feature fabrication was considered. However, after a well-characterized PDMS GDVN device was fabricated by Trebbin and associates using multilayered soft lithography (Trebbin et al., 2014), the multilayer lithography, inclined lithography, and 2PP wafer feature printing work on the PDMS GDVN was accordingly halted.

Trebbin's approach was used in the prototyping of a number of PDMS GDVN devices with sample-conserving features. As described previously, these utilize oil/water

droplet immersion and gas bubble generation to segregate small amounts of sample in a periodic fashion within the liquid stream prior to being reduced in diameter by gas dynamic forces, the aim being to match the sample droplet or plug frequency with that of the X-FEL pulse repetition rate. As the use of gas bubbles may also provide a mean of micromixing, this kind of device was also pursued.

2.3.2 Inclined Lithography

Photomasks made of chrome printed on soda lime glass appeared to be more favorable for use in the inclined lithography approach, and were therefore used instead of the Mylar masks used previously. Taking into consideration the refractive indices of soda lime glass (1.53) and SU-8 (1.65) at the expected exposure wavelength (Parida and Bhat, 2009), reference to Snell's Law indicates that the maximum transmitted angle to be expected coming from air is 37°. This is for an incident angle that approaches 90°. For a more practical incident angle of 60°, the result is a 30° transmitted angle. With the PDMS GDVN devices being fabricated with their liquid flow axis lengthwise along the plane of the wafer, the complementary vertical taper angle from the wafer plane would be 60°, but capillary cones are typically ground to a 15° to 30° taper. Sato et al. show that by immersing the wafer in a water medium the maximum transmitted angle can be increased. By making the refractive index of the incident medium 1.33 with water, the maximum transmitted angle when approaching 90° incidence becomes 53°, and the transmitted angle from the more practical 60° incidence becomes 45°, so that the complementary taper angle would be 45°.

Figure 9 and 10 show the original design scheme with views of the negative of the final structure. This would have required two highly precise photomask aligning steps following the initial deposition, patterning, and deposition of a second layer. Accurate alignment of photomasks required the consideration of the shadowing effect of the thickness of the chrome layer and also the thickness for the second photoresist layer. Using specifications of chrome thickness provided by the manufacturer and by assuming a specific target thickness of second layer, these corrections were incorporated into the photomask designs.

The alignment steps were found to be extremely difficult using existing lithography equipment – a situation made somewhat complicated by the need to immerse the aligned photomask and wafer at a 60° angle in a bowl of water. More sophisticated mask aligners do not appear to be compatible with this kind of volume. A somewhat less demanding approach was therefore used, which required only a single alignment step following the initial deposition. Figure 11 is a schematic diagram showing the simpler protocol, indicating the steps taken in the fabrication of the master wafer and the predicted PDMS outcome. This provided the desired converging section for the liquid line with the diverging portion of the nozzle shown in Figures 9 and 10 omitted. A device was fabricated using this process.

The alignment of the resulting two PDMS halves was accomplished by placing a drop of methanol between the two halves and allowing them to "self-align" with surface forces. In principle, this method is best used after treating the two connecting surfaces with oxygen plasma, so that an irreversible bond is achieved when the methanol layer is evaporated away. However, for faster prototyping, the PMMA clamping device

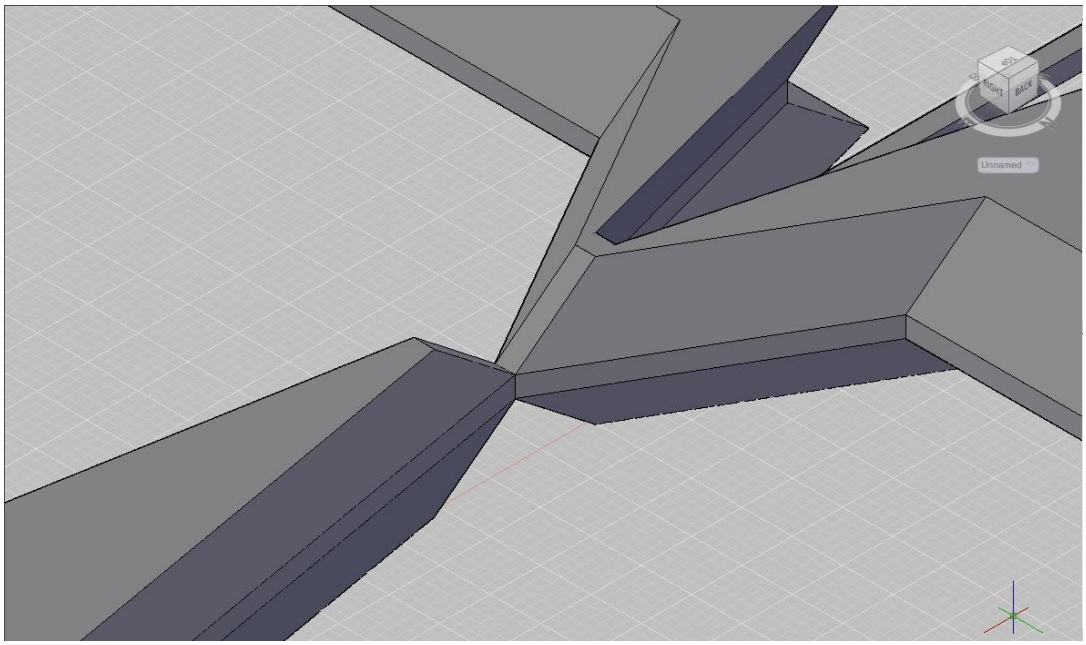

Figure 9: Conceptual design of (mirrored) inclined lithography wafer features. With the two resulting PDMS halves bonded together, the resulting device channels take on the negative this design. The cross section of the nozzle throat is 50 x 50 μm^2.

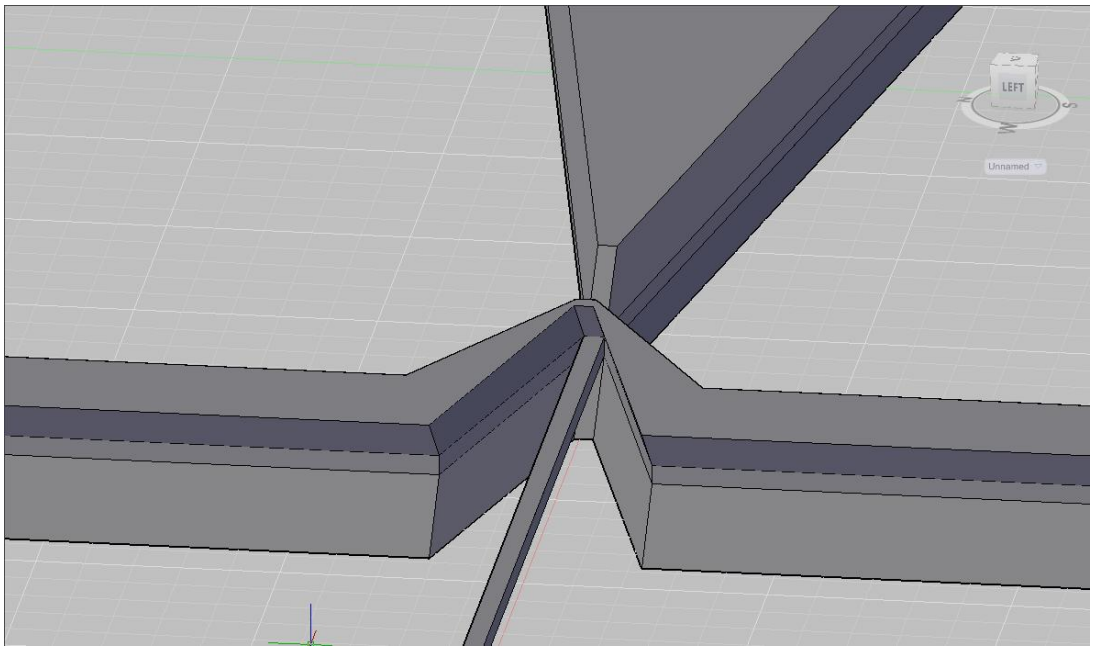

Figure 10: Different view of the converging section from Figure 9.

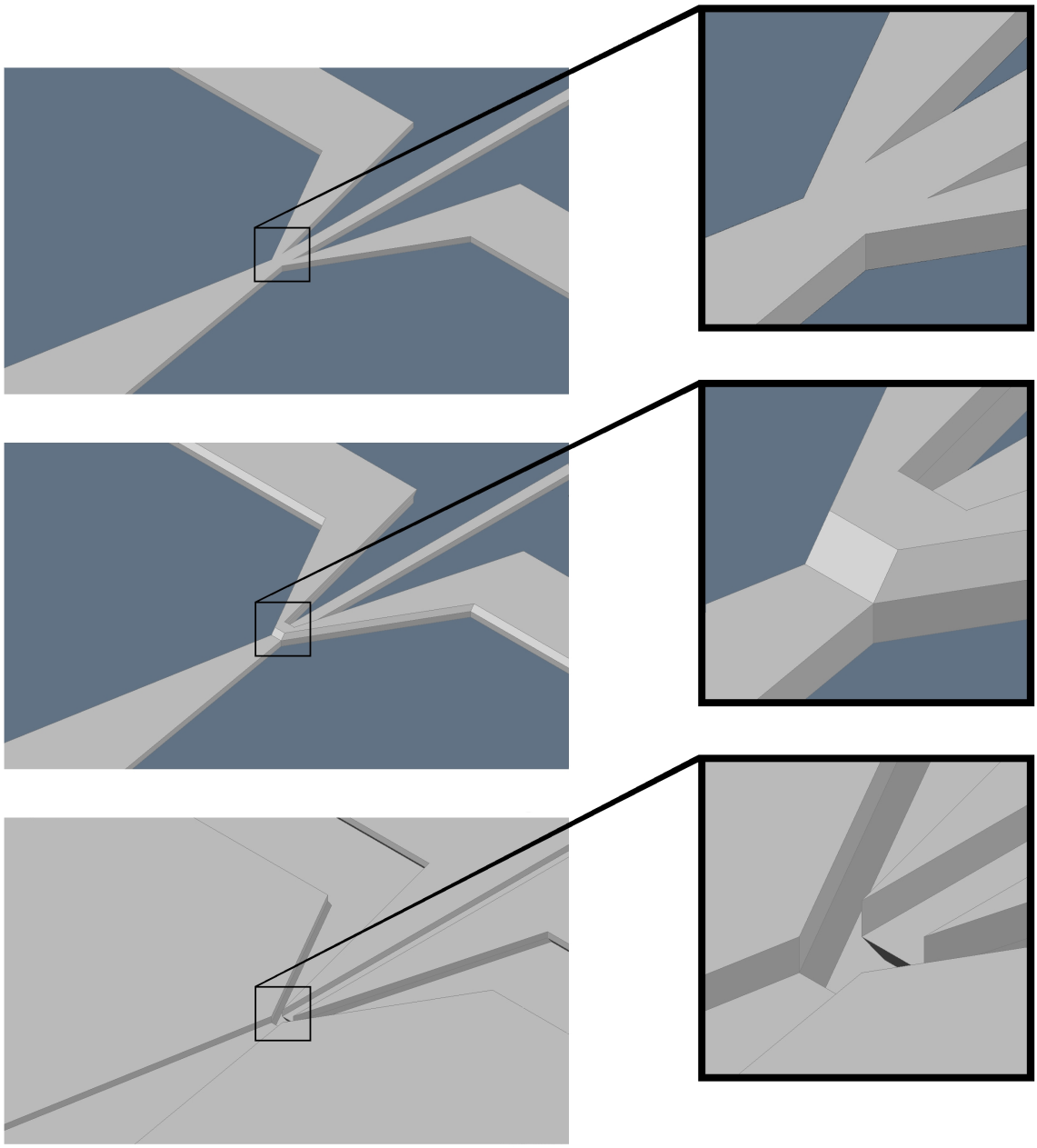

Figure 11: (From top) First layer of deposited photoresist on the master wafer made with using standard soft lithography; second layer of photoresist deposited using inclined lithography with water immersion; expected PDMS half, featuring with sharp terminations an all sides of the central line. Two of these PDMS halves are to be bonded together following oxygen plasma surface treatment. Alignment of the layers just prior to bonding may be accomplished with a temporary methanol layer that prevents bonding while surface forces cause the two symmetric halves allow to "self-align".

shown in Figure 4 was used after the methanol layer evaporated. Unlike the device tested in section 2.1, which required only one slab of PDMS, it was necessary to punch gas supply holes through one of the PDMS halves.

The test showed that higher-than-normal liquid line pressures were required to start the jet. The stream diameter was only reduced by about a factor of 2, compared to the typical case in which the stream is reduced by about a factor of 10. As can be seen in Figure 12, the profile of the PDMS device near the termination of the central line is not well defined, which likely contributes the less favorable performance. A true comparison of the performance of this design to the composite microfluidic GDVN from section 2.1 would require more successful fabrication.

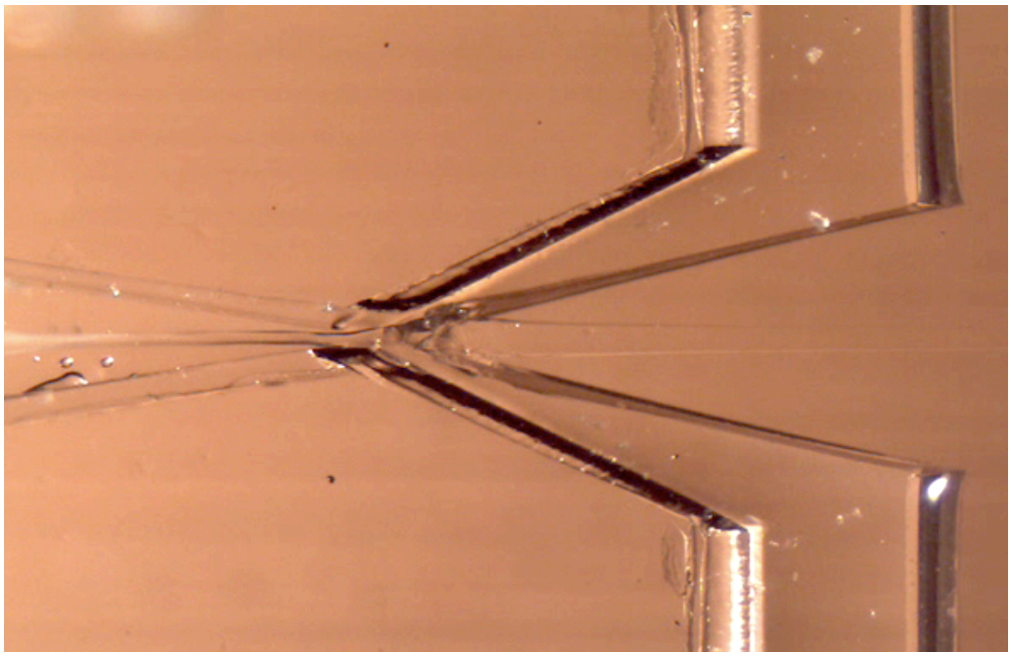

Figure 12: Prototype of microfluidic GDVN made using the inclined lithography approach shown in Figure 11. The device produces a large liquid jet (25 to 35 μm) and requires higher-than-normal pressure to the liquid line to initiate jetting. Instead of an oxygen plasma surface treatment, the PMMA clamp from Figure 4 was used to hold the two halves together following the "self-alignment" procedure described in Figure 11.

2.3.3 Multilayered Lithography Tests

Composite-style microfluidic GDVN tests that roughly resembled the expected geometry of a PDMS-only style device made with multilayered lithography were conducted both before and after the inclined lithography tests. The first tests were not extensive and indicated that the multilayered approach might not result in a working jet, while the tests that followed the inclined lithography work indicated to the contrary. Both tests involved using an inner capillary with a wedge profile (Figure 8 and 13). The most significant difference between the former test and the latter was the inner capillary inner diameter (100-µm inner diameter in the former test; 50-µm inner diameter in the latter).

The inner capillary that was used is shown in Figures 13. As can be seen in Figure 14, when the orifice of glass capillary has only two sharp edges, jetting is indeed possible. The only possible difference in performance was that it appeared to necessary to begin at a higher-than-normal liquid line pressure in order to initiate jetting, as compared to the previous microfluidic GDVN tests. One difference in the experimental parameters was that 50-µm inner diameter gas lines, as opposed to 100-µm inner diameter gas lines, were used in the second wedge experiment as a matter of convenience. Also, a stagnation pressure reading was not made, so that only the upstream meter pressure near the gas tank was read. More consistency in the experimental parameters is needed to give a fairer comparison. However, the conditions for the liquid line (except for the wedge profile) were the same for both experiments. In the coned-tip composite GDVN testing from section 2.1 the liquid line pressures that were testing ranged from 25psi to 200psi with jetting being typically initiated at 25 psi and never more than 50 psi

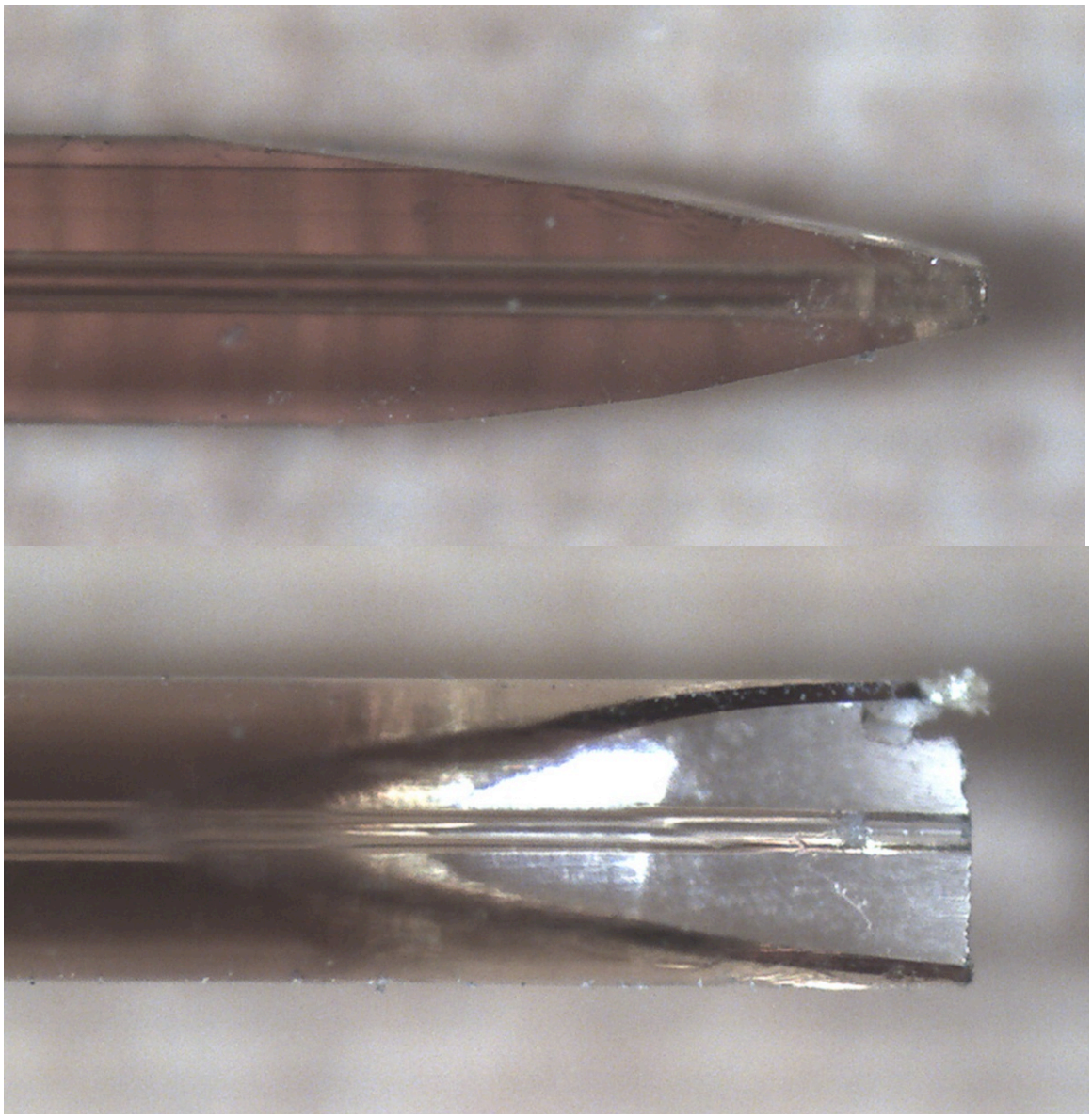

Figure 13: (Top) 50-µm ID ground capillary in wedge profile from above. (Below) side view of wedge capillary.

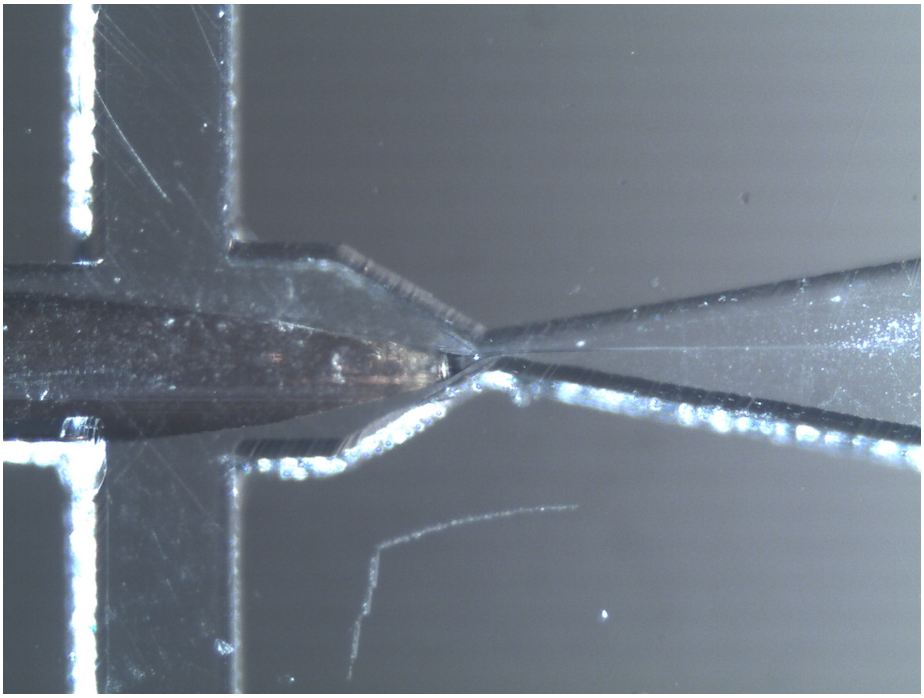

Figure 14: Composite microfluidic GDVN using the wedged-profile capillary shown in Figure 13.

over the entire range of gas focusing pressures that were tested. For the wedge design, a liquid pressure of 125 psi was required to initialize jetting. The resistive effect of using 50-µm inner diameter gas lines instead of the 100-µm inner diameter gas lines appears to suggest that even a higher liquid line pressure may have been necessary if testing conditions had been the same. However, this is not certain.

Figure 15 shows the multilayer lithography fabrication scheme that was originally devised. After the tests described above, a multilayered lithography master wafer was fabricated using an approach that was slightly different from the approach in Figure 15. The diverging section of the Laval-like profile was kept at the same level as the sample line channel, so that the cross section of the nozzle throat would match the cross section of the supply channel. This was accomplished by repurposing one of the photomasks used for the inclined lithography. Figure 16 is an image of the resulting master wafer (a

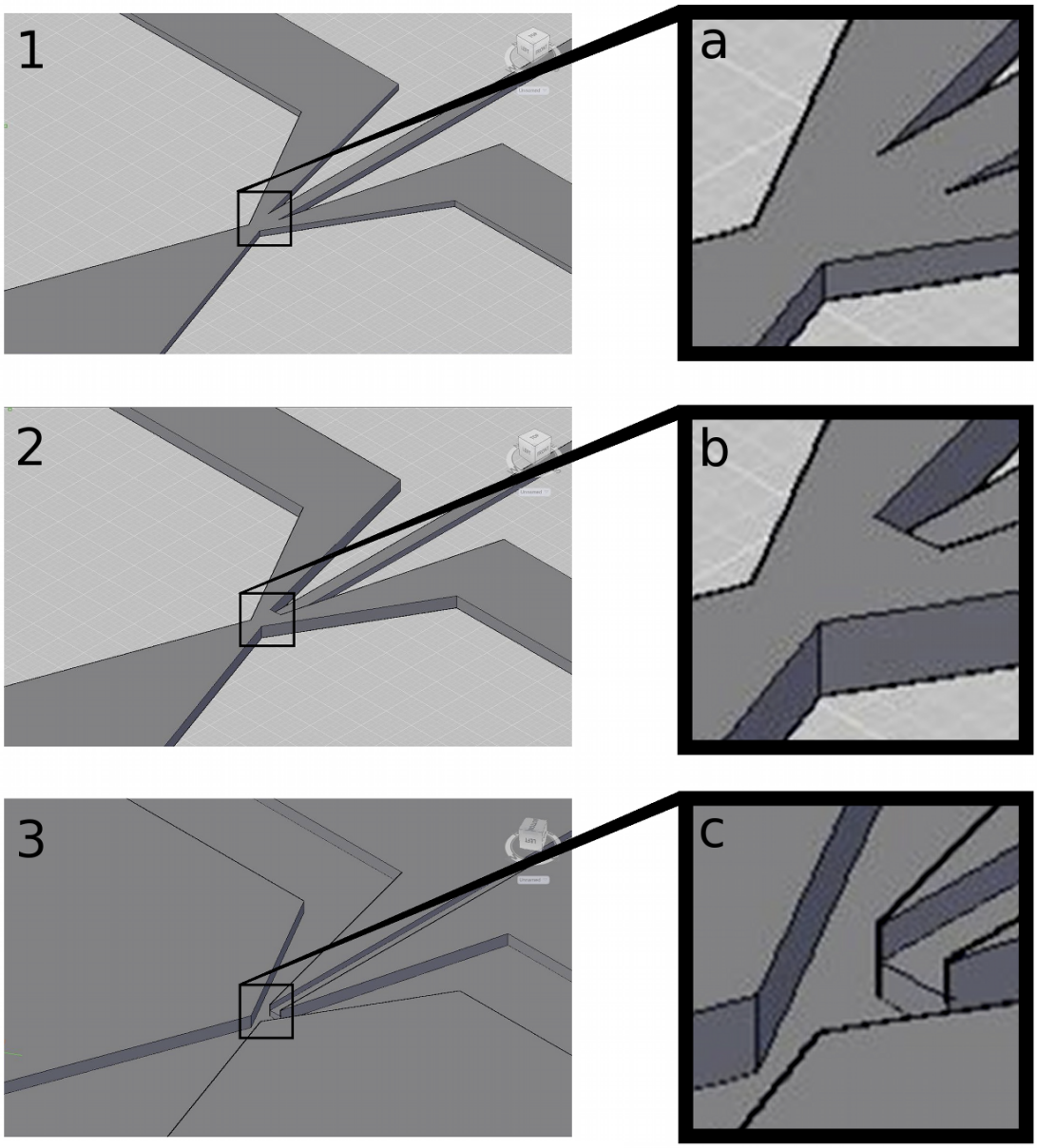

Figure 15: Conceptual drawings representing the primary steps in the fabrication of a PDMS-only microfluidic GDVN using multilayer lithography techniques. 1) The first SU-8 layer is patterned using the standard procedure, except that after post-exposure baking, another layer of photoresist is immediately spincoated in preparation for the second step. 2) The second SU-8 layer is patterned using a second photomask that is aligned with high precision before exposure. The usual chemical development procedure is then carried out to completion. 3) The resulting profile of the PDMS slab is the exact negative of the profile shown in part 2). Two of these half-pieces then were aligned using a drop of ethanol for "self-aligning", holes for the gas lines were punched, and the two aligned halves were placed in the PMMA clamping device from Figure 4.

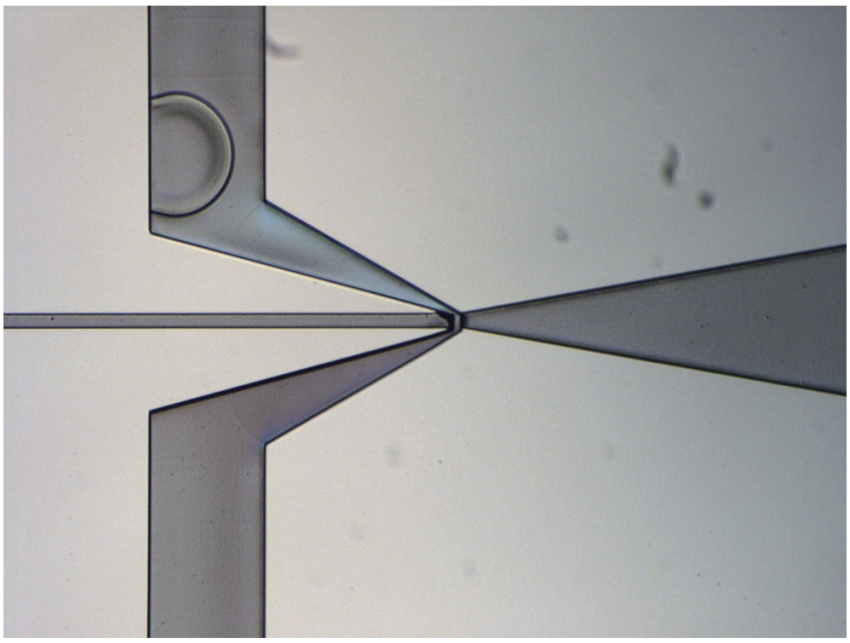

Figure 16: Actual fabrication of the step design shown in Figure 15, except that the diverging section was kept at the same height as the liquid line in this case.

negative of the PDMS device). In a single test of a PDMS nozzles made using this wafer, there was no jetting. The published PDMS GDVN developments of Trebbin and associates in early 2014 (which follow more closely the approach in Figure 15) put a stop to the multilayer lithography GDVN project.

2.3.4 Wafer Fabrication with 2-Photon Polymerization

There is an alternative strategy to GDVN wafer fabrication, which may turn out to enable the pursuit of GDVN devices with more complicated functionality. This involves the use of 2-Photon Polymerization (2PP) 3D printing to fabricate wafer features. (2-Photon Polymerization for direct printing of the GDVN is the subject of chapter 3, and so the printing technology will be cover more completely in that chapter.) Briefly, 2PP allows submicron resolution printing (features down to 150 nm), and through a stitching

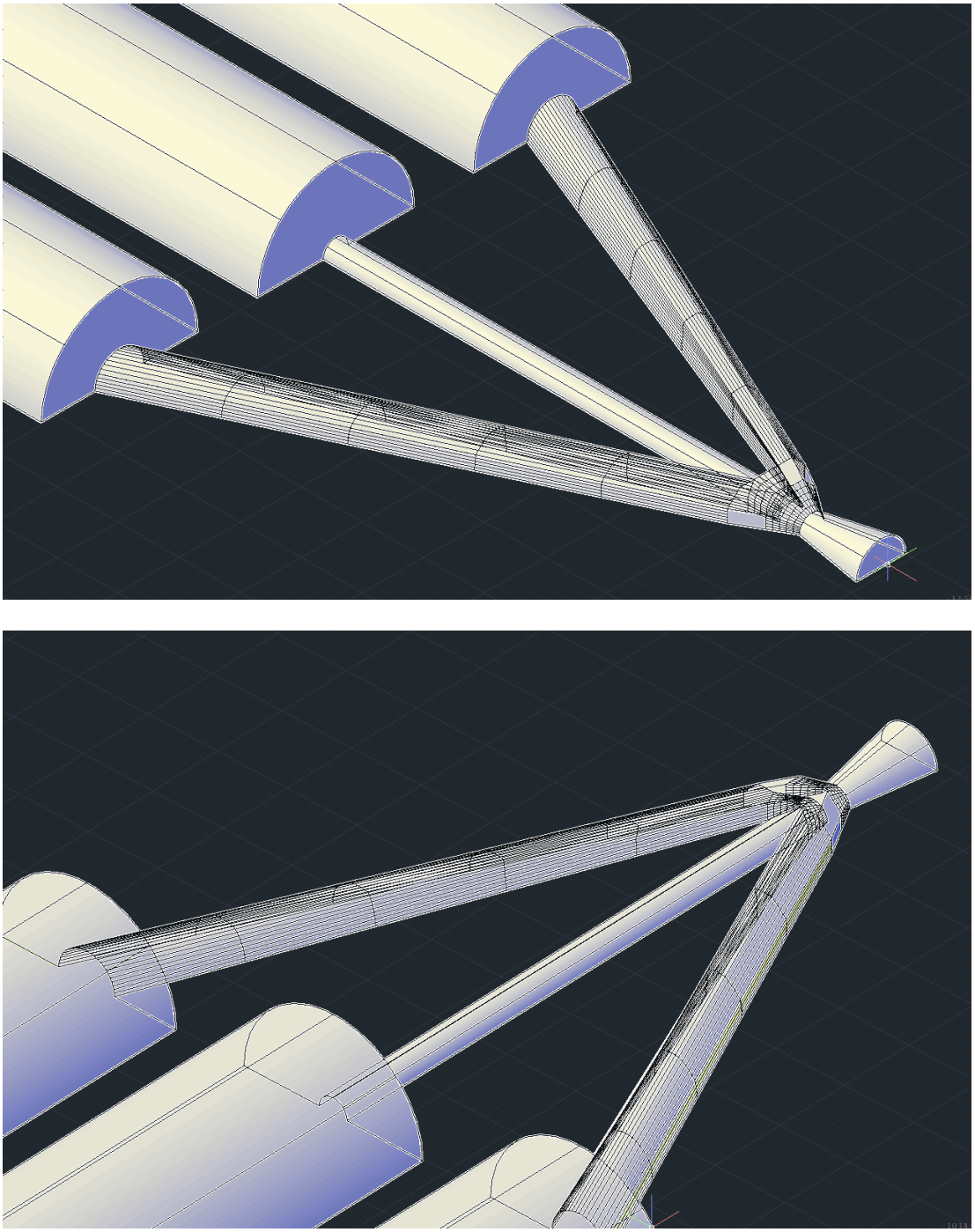

Figure 17: 2-Photon Polymerization allows complex 3D structures to be patterned directly onto a master wafer. However complex, it is necessary that features be made that will not be lifted off when PMDS is removed from the wafer. In this design the gas lines transition smoothly from 100-µm diameter semicircles to upside-down J-shaped cross sections to form the gas-accelerating region. A major advantage of this technique is the ability to have radial symmetry in the channels. Besides providing more radial symmetry in the jet generation region, the cylindrical ports for supply capillaries may allow for a strong bond using an oxygen plasma surface treatment.

technique covers an areal range of about 10 x 10 cm^2 with a reliable vertical range of about a 1 mm. Using this technology, the device attempted in section 2.3.3 could be accomplished easily, as suggested by the design shown in Figure 17.

Obviously it is necessary to limit the detail of the design to allow for the ability to peel off a piece of cured PDMS without lifting off the wafer structures. Besides providing more radial symmetry in the jet generation region, there are cylindrical ports for supply capillaries, which may allow for a strong bond using an oxygen plasma surface treatment.

2.4 Droplet/Bubble Jet

2.4.1 Overview

Studies of the physics behind the formation of droplets in immiscible fluids date back work by G. I. Taylor in 1934. More recently, Thorson et al. undertook to quantify the formation of emulsions in microfluidic devices (Thorson et al., 2001). Around the same time, studies were performed for gas bubble formation in liquid (Gañán-Calvo and Gordillo, 2001; Gañán-Calvo, 2004). In both cases the liquid droplets or gas bubbles the devices produced were highly monodisperse and regularly spaced.

This has an application in sample conservation in the GDVN by syncing the droplet/bubble formation according to the XFEL pulses (for instance, 120 Hz at the LCLS). In the case of droplets, the droplets may be made to hold the sample that is being probed, so that tuning of droplet size and spacing would allow for significant sample conservation. In the case of gas bubble formation, gas bubbles placed at regular intervals

function to temporarily turn the jet off at a frequency and duration that reduces sample consumption.

Both the droplet and bubble formation process typically involves the input of three sources: two channels feeding in the carrier fluid and a single channel feeding the medium that forms into either the liquid droplets or the gas bubbles. An assessment of the actual advantage in sample consumption that a droplet/bubble-supplied GDVN has over a GDVN supplied from a single reservoir is perhaps best given by simply comparing the depletion rate of whatever reservoir supplies sample. However, the possible utility of the droplet/bubble method may be considered beforehand by assuming identical linear velocity of the sample line flow rate for an oil/water droplet immersion GDVN and a water-based GDVN. In this case the reduction in sample consumption is given by the ratio of the volume of a droplet to the total volume between centers of droplets (cylinder of length *l*):

$$\frac{4}{3l} \times \frac{r_{droplet}^3}{r_{cylinder}^2} \qquad [1]$$

A flow rate of 5 μL per minute in a 50-μm inner diameter channel corresponds to a linear fluid speed of about 4.2 cm/s. In this case, 120 Hz droplets would correspond to a droplet spacing of about 350 μm between droplet centers. If the droplets are 25 μm in diameter, then the emulsion jet uses about 1% of the sample that would be used with a water-based GDVN. This depends on whether or not 25 μm droplets can indeed be generated with the said spacing at the said flow rate. However, even if the distance between edges of 25-μm droplets approached zero (840 Hz droplet frequency) this would result in about 8% the

sample consumption. Gas bubbles acting as spacers that define an off-on cycle would need to span the 300 μm between sample sections for optimal operation at a linear flow speed of about 4.2 cm/s. Elongated gas bubbles of this sort are in fact possible to generate, but whether or not the exact lengths at the desired flow speed can be achieved is a matter that needs to be explored experimentally.

In this section is set out preliminary results of the water/oil emulsion GDVN as well as a design for a device that combines gas bubble generation with micromixing. Two prototypes for the droplet jet were concurrently pursued. In one design the droplet generator is located 2 to 3 meters upstream of the GDVN, while in another design the droplet generation occurs a couple hundred microns upstream of the GDVN. Both designs are intended for in-vacuum operation in the CXI hutch at the LCLS. Each approach poses advantages and disadvantages.

The first approach allows the droplet generator to be any size, since it is located outside of the vacuum chamber. The freedom of space makes it possible to simply use a commercial droplet generator, which could then be coupled to the glass-based GDVN. However, the upstream distance of the droplet generator may make the droplets more susceptible to drift during their long transit. Also, after an adjustment to droplet generation parameters, one must wait a few minutes for the change to reach the X-ray/sample interaction region. With the second approach, on the other hand, the design dimensions are retrained by the need to fit inside of the chamber by way of a long cylindrical cavity that allows no more than about a half-inch radial clearance. However, changes to operating parameters would take effect at the interaction region essentially immediately. This is a significant advantage during data collection. Regular adjustments

may be essential if the phase of the droplets relative to the phase of the X-ray pulses drifts during the experiment. Furthermore, the second approach more easily allows for integration of other microfluidic features that must be positioned near the GDVN, such as for micromixing.

2.4.2 Droplet Generation

Oil was chosen to be the droplet carrier. Accordingly, the first part of development involved testing an oil jet, which had not previously been done. Oil was supplied to a glass-style GDVN, and jetting was successful. The only significant difference was the droplet gestation length, which was much larger than that of water (Figure 18).

In lieu of purchasing a commercial droplet generator for the first approach, a repurposed PDMS chip was used. Details on this phase of the study are reported in more detail elsewhere (Echelmeier & Nelson et al., 2015). Briefly, droplet generation was accomplished, but the frequency was not brought up to speed with the 120 Hz of the LCLS due to problems with the integrity of sample connections. This was also likely due to the fact that the geometry of the repurposed device was not optimal: the inner diameter of the capillary leading to the GDVN nozzle was much smaller than the output channel of the droplet generating device; an output channel that matches the capillary leading to the GDVN device would likely be capable of higher frequencies using the same input pressure. The PMMA device from Figure 4 was used to achieve an improved seal through clamping pressure, and a frequency of 30 Hz was achieved.

Future work for this device will likely be benefitted from the use of a commercial droplet generator in a more robust material such as glass or silicon. This should allow much stronger sample line connections, reusability, and an optimized geometry that may significantly improve performance.

Figures 19, 20, and 21 show the photomask designs for the second approach, which are based on the PDMS GDVN device made by Trebbin and associates, but with the added droplet/bubble generation device and a different approach to the supply line connections. The supply capillaries are meant to be inserted directly into the PDMS channels. This co-linear approach is motivated by the geometry of the injection system at the CXI station at the LCLS, which was originally designed to accommodate the glass-type of GDVN, and which contrasts with what is typically done with microfluidic device, which is to connect the sample lines perpendicular to the patterned channels of the device. There is no room to set up a perpendicular connection of this kind. Furthermore, typical methods for making microfluidics supply line connections are not sufficiently strong for reliable GDVN operation. The parallel connection approach described below aims to provide maximal bonding strength.

In thinking about making a parallel capillary connection to a PDMS device, the first consideration is that one would be placing a cylinder into a square or rectangular channel. If the PDMS channels are made smaller than the supply capillary, the PDMS may flex to create a seal, and uncured PDMS may be used as well to fill in any gaps (Kelly et al., 2014). However, the strength of the bond in this case is still in question when it comes GDVN operation. Since glass bonds very well to PDMS using an oxygen

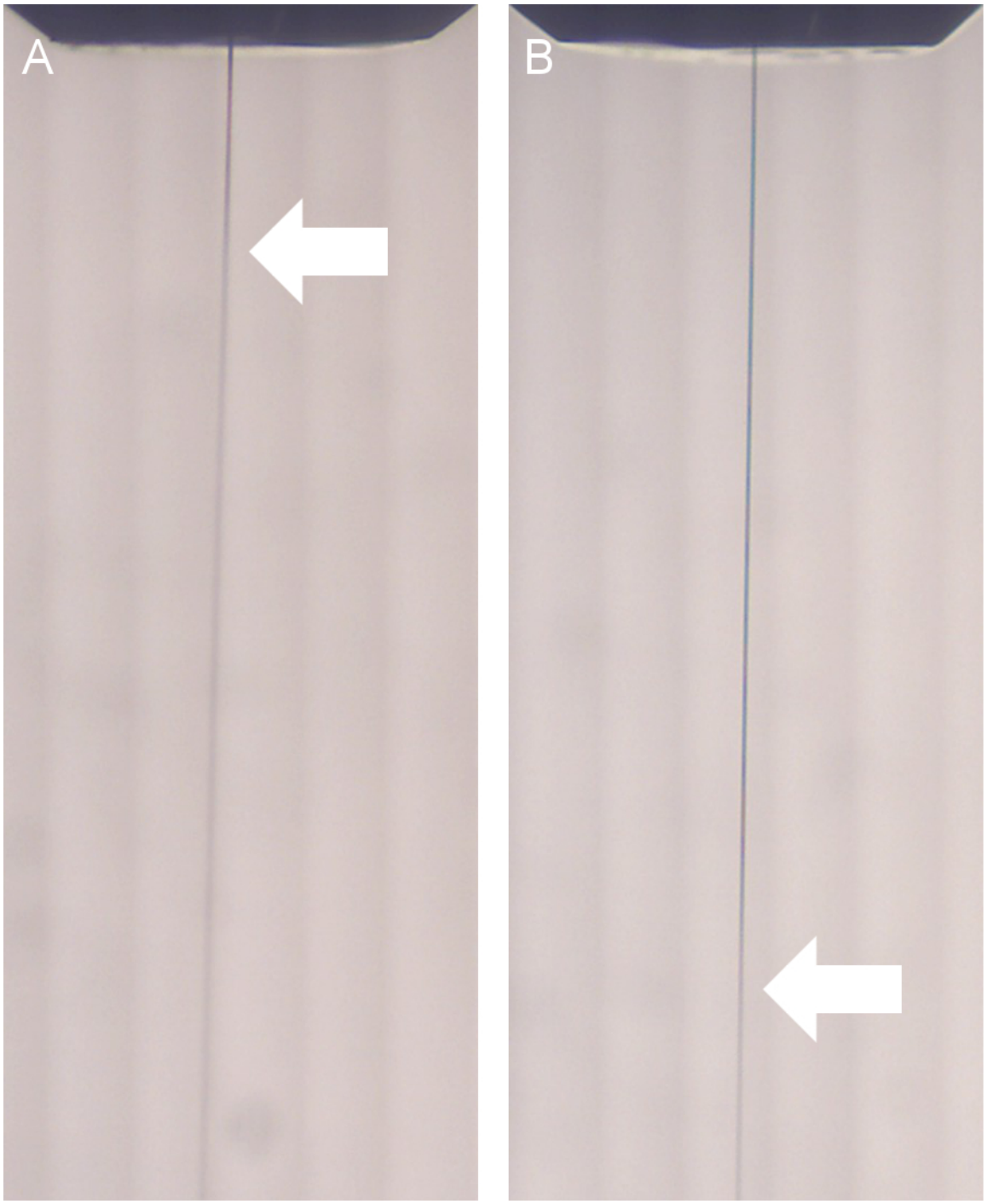

Figure 18: A) Water jet in a GDVN for comparison to B) an oil jet made with the same GDVN. The arrows in each picture identify the approximate point where droplet breakup begins, as suggested by fading of the jet stream. High speed video also confirmed this difference.

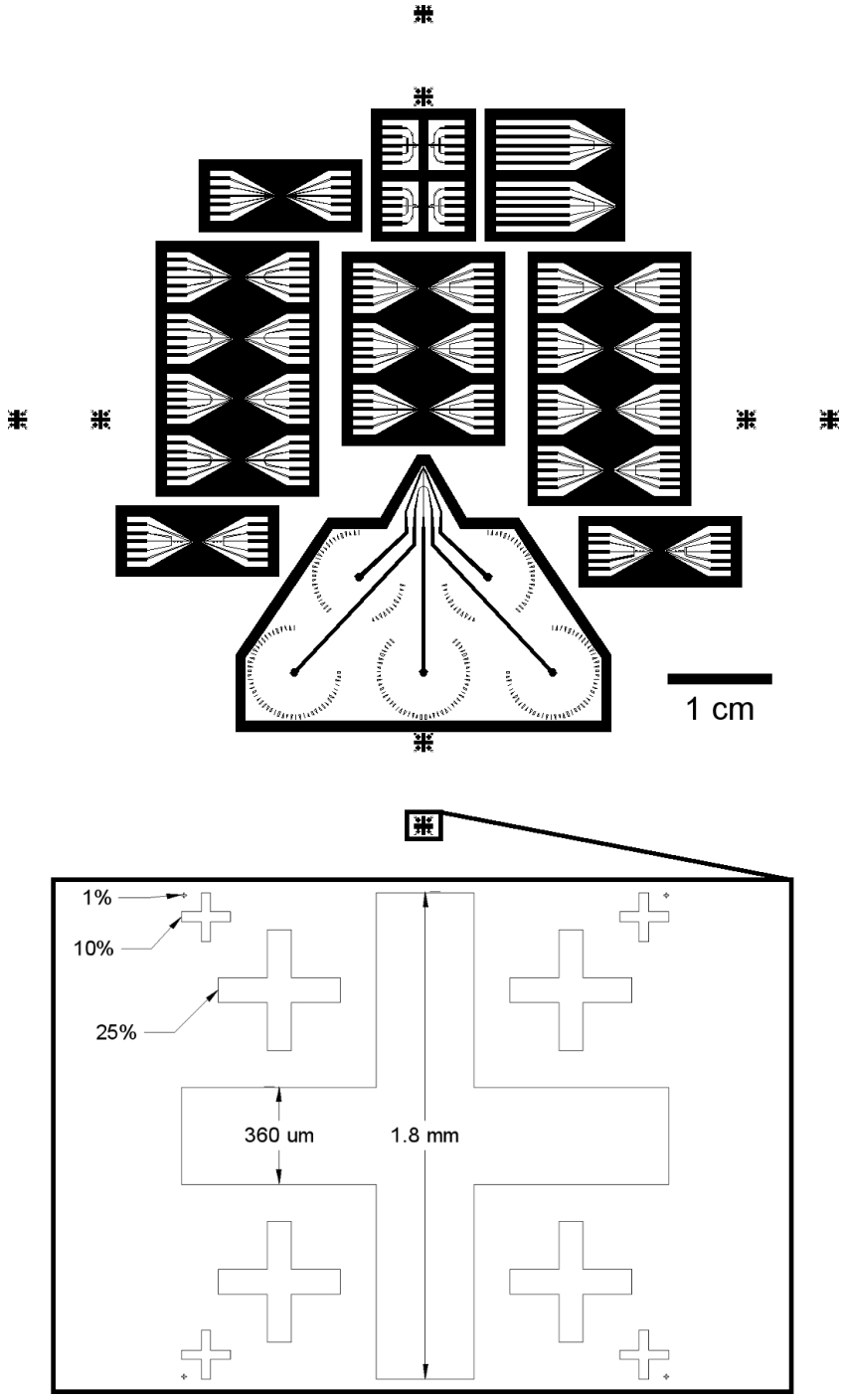

Figure 19: (Above) One of two photomasks used to pattern the master wafer for the second approach to the oil/water droplet generator GDVN. (Below) Close-up view of the alignment marks used. As shown, the cross pattern was repeated and scaled down to assist in finer alignment; the percentages are based on length. The second photomask (not shown) included marks that outline these crosses. Certain nozzle features were purposefully omitted in the design of the second photomask; the differences are depicted in Figure 20.

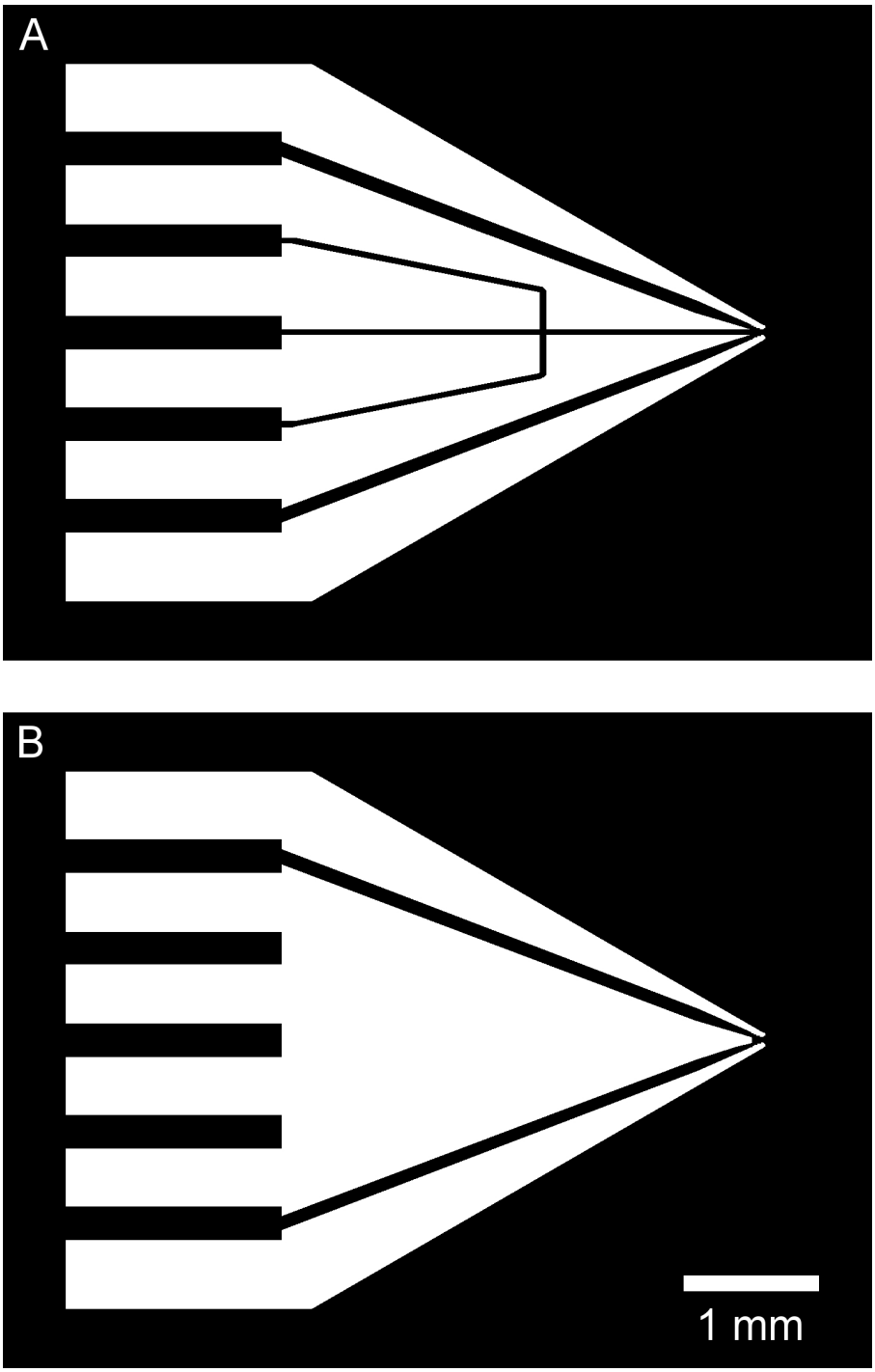

Figure 20: Oil/water droplet-generator GDVN photomask features used in the second approach to the droplet generator GDVN. A) Nozzle pattern from photomask 1 (see Figure 19); the central channel carries one immiscible fluid while the two adjacent channels carry the other immiscible fluid. The outermost channels supply gas. B) Nozzle pattern from photomask 2, indicating what features from photomask 1 were omitted (the fluid channels for oil/water droplet generation are not present).

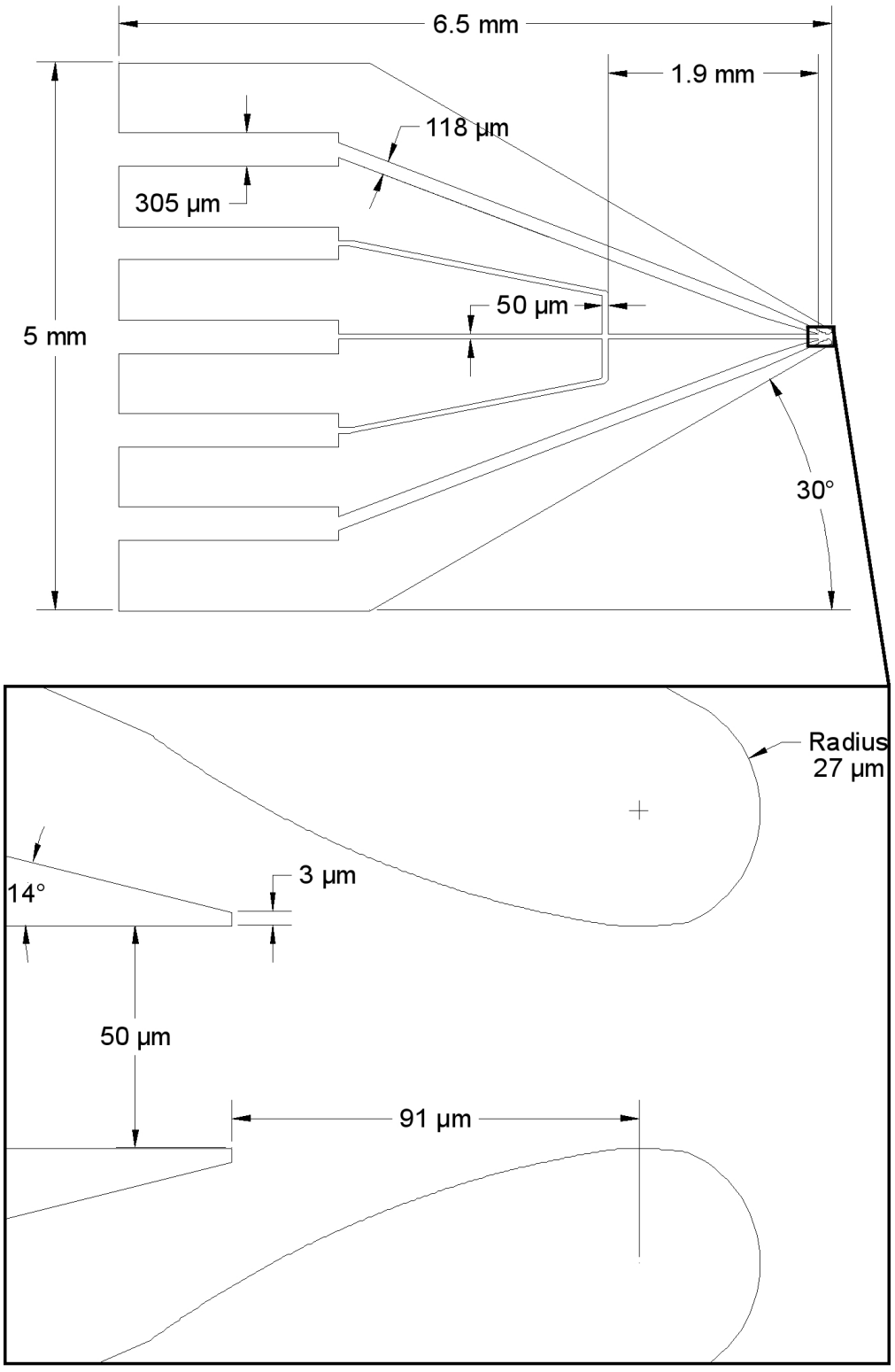

Figure 21: (Above) Dimensions for the photomask 1 feature shown in Figure 20. (Below) Close up view of photomask design of GDVN tip from photomask 1 with dimensions.

plasma surface treatment, one possible solution is to melt the polyimide coating off the capillary and attempt to bond the glass capillary to the PDMS channel. However, the stretching of the PDMS may present a problem in this case: stretching a microscopic PDMS square channel to fit a cylindrical glass surface without premature bonding of the surfaces would likely be extremely difficult, if not impossible. Even using a methanol layer may prove ineffective if the methanol were simply forced out of the interstitial space when the stretching occurs. An alternative is then to use square-profile glass capillaries that are just slightly smaller than the PDMS channels. Thorslund et al. show that bonding the square-profile capillary in place after oxygen plasma treatment is feasible (Thorslund et al., 2007). For sample injectors in serial crystallography experimentation it is important to use polyimide-coated glass capillaries to prevent breakage during handling, and there are polyimide-coated square profile capillaries commercially available. However, since it is desirable to bond the glass surface of the capillary to the PDMS channel, use of coated capillaries presents some complications. One obvious approach is to remove a small portion of the coating either with heat or chemical etching, but it is likely that stress/strain on the capillary will be experienced by part of the uncoated region, leading to breaking off of the capillary. One solution is to encase the entire device in epoxy after the lines are connected, with just the nozzle tip protruding, thus protecting any flexing that would lead to breakage where the coated capillary transitions into an uncoated capillary. What is left to do in this case is to somehow couple square-profile capillaries to fittings intended for cylindrical capillaries. This may be done by gluing the square-profile capillaries into larger cylindrical capillaries. In an alternative approach, the PDMS channel could be made a little bit

larger so as to receive a square-profile capillary with an inner wall-to-wall distance that is large enough to receive a standard coated cylindrical supply capillary. The square-profile capillary would then only act as the receptacle for the standard coated capillary and would terminate just outside the PDMS device. This provides a glass surface to which the inserted polyimide-coated cylindrical capillary could bond using epoxy that is pulled in by capillary action. In this sequence, PDMS is bonded to glass via oxygen plasma surface treatments, and polyimide is bonded to glass via fast curing epoxy, forming a strong bond that can handle the pressures needed to run a GDVN. Thus a collinear supply connection is accomplished with high bond strength. This strategy is depicted in Figure 22. Epoxy encasing could be performed in this case as well. In fact, this was done with a dummy model and was found to protect the supply lines very effectively.

A problem with this approach arose when something unfavorable was discovered about the tolerances of commercially manufactured square glass capillaries. SEM images revealed that the dimensions of the square cross section of the capillary tubing can vary substantially from published dimensions (Figure 23). The published interior wall-to-wall dimension for the capillary shown in Figure 23 is 200 μm with a wall thickness of 76 μm. Presumably then the total external wall-to-wall median dimension is 352 μm. The published tolerance, which was much more difficult to find, is +/- 20 μm. As shown in Figure 23, the actual external wall-to-wall dimension for one of the capillary cells was 305 μm and the internal wall-to-wall distance was 215 μm. Evidently the tolerance is additively applied to the inner dimension as well as to each wall for a total external wall-to-wall distance of 352 +/- 60 μm. Otherwise, it appears that manufacturers may be concerned with keeping the inner wall-to-wall dimensions within a specification, without

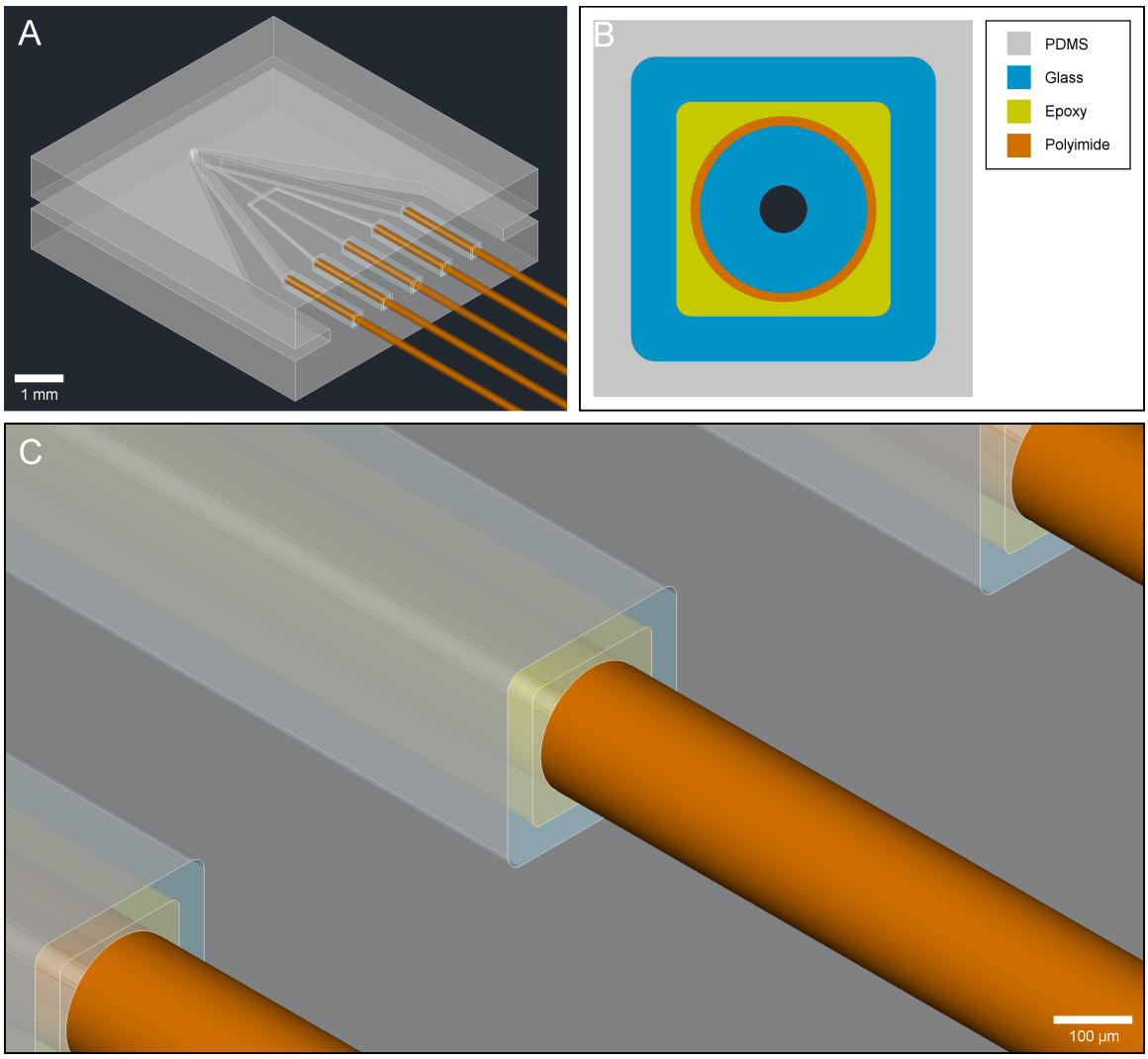

Figure 22: Depiction of strategy for in-line supply connections to oil/water droplet generator GDVN: A) overview of device; B) cross section of the connection within the PDMS device showing the bonding order of the materials and C) a close-up view of A. Following the "self-aligning" of the two PDMS halves as described in Figure 11, the square-profile glass capillaries may be inserted into the channels, with the bonding through surface activation with oxygen plasma delayed by the layer of methanol left within the channels. Note that in practice it is likely that the square-profile capillaries will protrude outside of the PDMS device. After the methanol layer is removed and bonding completed, the polyimide-coated capillaries are then inserted and bonded to the interior glass surface of the square capillary with epoxy, which is pulled into the interstitial space through capillary action. During curing of the epoxy the cylindrical capillary may not center itself within the square channel, leading to an offset of the actual supply line (solid black circle in B) with the interior PDMS channel at the abutment (note that the figure was drawn according to the actual dimensions of supplies that are commercially available without customized engineering). A customized cylindrical capillary that closely matches the square capillary would eliminate this problem.

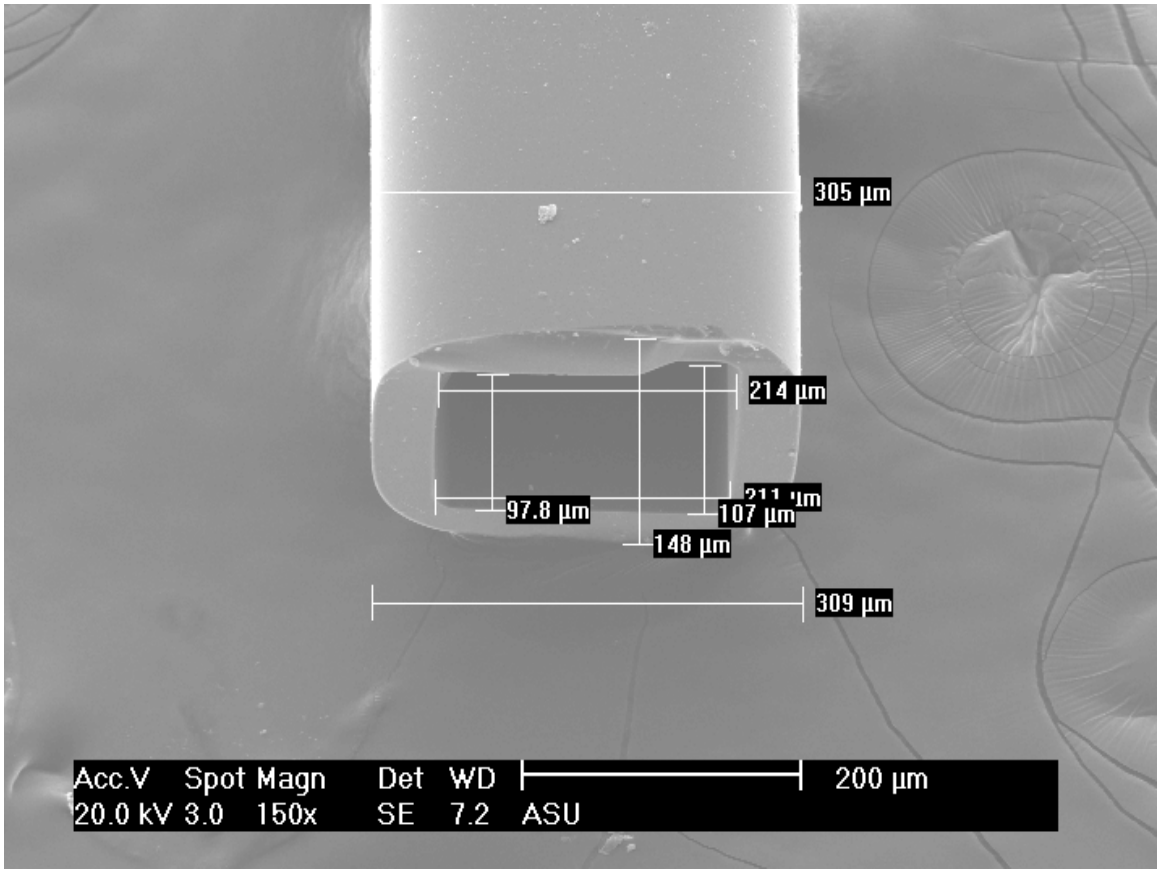

Figure 23: SEM image of square-profile capillary.

much regard to the outer wall-to-wall dimensions. This is a significant problem in this application. If the outer dimensions are too large, insertion of the square tubing may be impossible following oxygen plasma treatment. The methanol layer may be displaced too much, causing bonding before the capillary is fully inserted. Even if successfully inserted, the over-stretching of the PDMS may encourage failure of the oxygen plasma bond between the two PDMS halves. On the other hand, if the outer dimension of the square-profile capillary it too small, it may not be possible to make a complete seal about the periphery. The effect of these large variations is a decrease of the fast-throughput nature of soft lithography by requiring a new photomask to be made when supply

capillaries vary. Ways around this problem include purchasing long lengths of square tubing or large batches of precut tubing taken from the same sized tube and/or designing photomasks that vary the receptacle channel width. In this investigation the photomask from Figure 19 contained several such variations with channels that were either in agreement with, slightly larger, or slightly smaller than the square-profile capillary measured in the SEM image.

2.4.3 Micromixing Bubble Jet

Testing of gas bubbles as a spacing medium for sample is easily done with the devices on the wafer shown in Figure 19. A special device was included on the wafer that makes use of a technique shown by Mao, et al. (Mao et al, 2010), in which gas bubbles are introduced into a Y-junction of fluids to be mixed, shortly followed by multiple hexagonal chambers in line with the channel carrying the fluid-1/fluid-2/gas bubble medium. The bubbles act chaotically when passing through the hexagonal chambers, mixing the fluids. It appears that the bubbles then emerge from the chambers in a periodic fashion. These hexagonal chambers were incorporated into the droplet generator design (Figure 24), and may provide a device that both mixes fluids at millisecond resolution and conserves sample through gas bubble sample segregation.

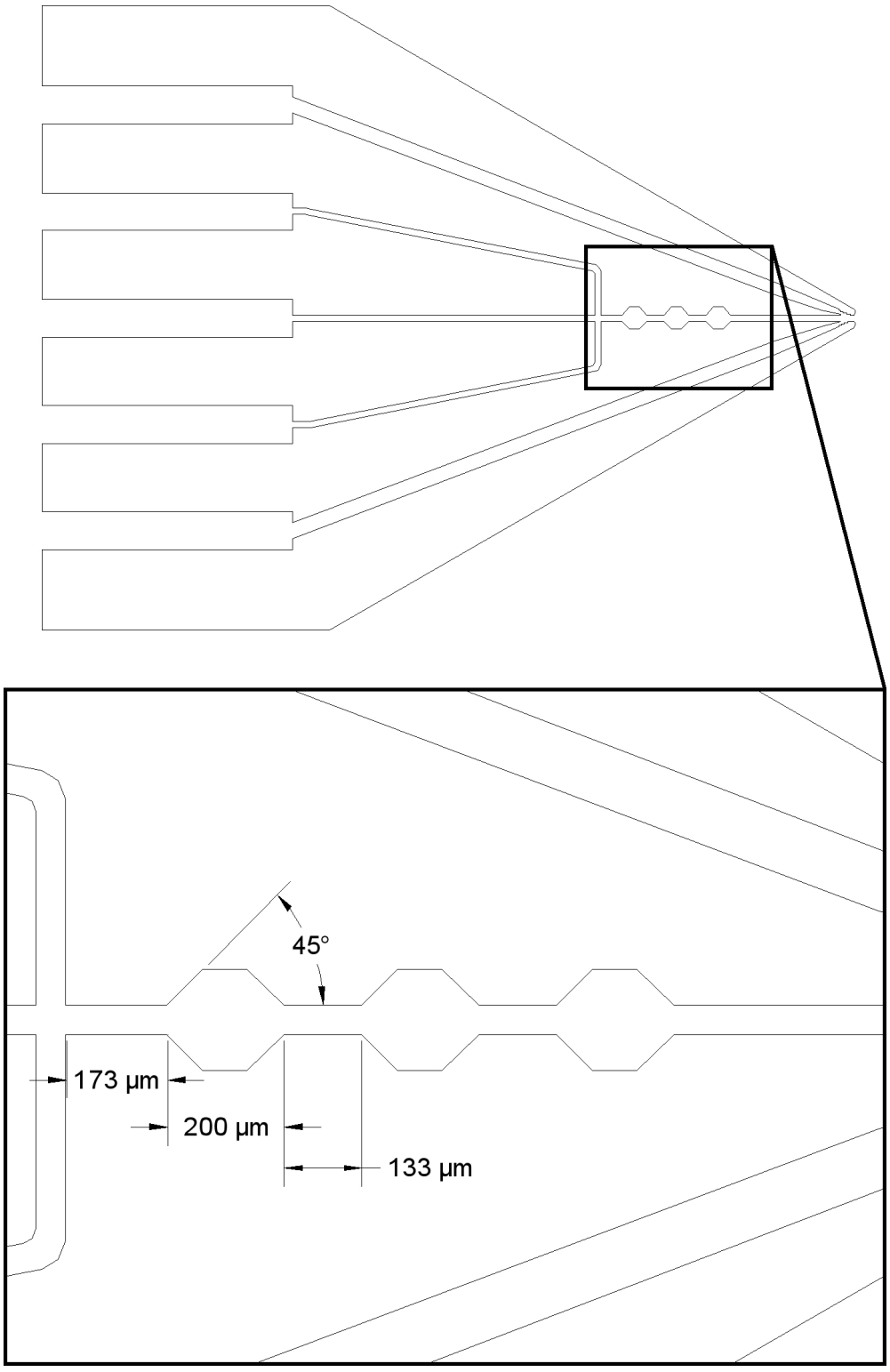

Figure 24: Design for gas bubble sample conserving microfluidic GDVN that also uses in-line hexagonal chambers for chaotic mixing of fluids with the gas bubbles. This is a modification of the design shown in Figure 21.

3. 3D PRINTING: 2-PHOTON POLYMERIZATION

3.1 Overview

A technique was desired which builds all the critical GDVN components in a robust material using a single process to an arbitrary design shape. Direct laser writing offers the ability to write both the internal and external GDVN structures at high resolution in robust polymer materials in an arbitrarily complex fashion. By utilizing a 2-photon polymerization (2PP) process, direct writing enables 3D printing of microstructures with a resolution well beyond other high-resolution 3D printing technologies like Stereolithography (SLA), for instance. This is achieved by tightly focusing a laser into a liquid transparent photoresist. Within a small region near the focus the light intensity is high enough to trigger a non-linear light absorption process that photopolymerizes, and hence solidifies, the resist locally. By moving the absorbing medium relative to the laser with nm-precision and employing special techniques, experimental groups have demonstrated reproducible resolutions ranging from 20 to 120 nm (see review by Zhang et al., 2010).

Until recently, the use of 2PP for GDVN fabrication has not been considered due to prohibitively long writing times. A traditional GDVN composed of 120 nm wide voxels is comparable to city composed of LEGO® blocks. However scale-variant this analogy may be (i.e. laser scanning a row of 10 nanometric voxels is undoubtedly faster than hand-laying 10 consecutive LEGO® bricks), the projected writing times for a single nozzle nevertheless ranged from several days to months depending on the technology considered. However, commercial developments in fast-writing mechanisms now make this technique an ideal match for GDVN fabrication.

The Photonic Professional GT (Nanoscribe GmbH, Karlsruhe, Germany) is capable of submicron resolution high-speed printing. As currently published by Nanoscribe (See specifications at http://www.nanoscribe.de), when using a 63x, NA=1.4 objective lens with IP-Dip photoresist, piezoelectric technology allows ultra-precise arbitrary 3D trajectories over a range of 300 x 300 x 300 μm^3, while a scanning unit based on pivoted galvo mirrors provides high speed (typically 10 mm/s) layer-wise writing over a range of 140 x 140 μm^2 (200 µm Ø). The total accessible writing area of piezo-mode and/or galvo-mode operation in this case is 100 x 100 mm^2. Other objective lenses are available in the Photonic Professional GT system, enabling alternative or extended functionality.

The immediate consideration was how much of the glass-type GDVN apparatus could be printed and how long it would take using this technology. The most ideal of outcomes involves printing a device that couples directly to microcapillaries via small commercial fittings, such as MicroTight® 6-32 headless nuts for 360µm OD tubing from IDEX. In other words, the device would have receptacles for these fittings printed directly into the device. This would result in a device that is immediately ready for use after the printing is complete and which may be disassembled for cleaning or replacements of parts and reuse. Figure 25 is a cut-away conceptual drawing of this device. The device (without the cut-away section) fits into a 2 x 1 x 0.5 cm^3 box, with an

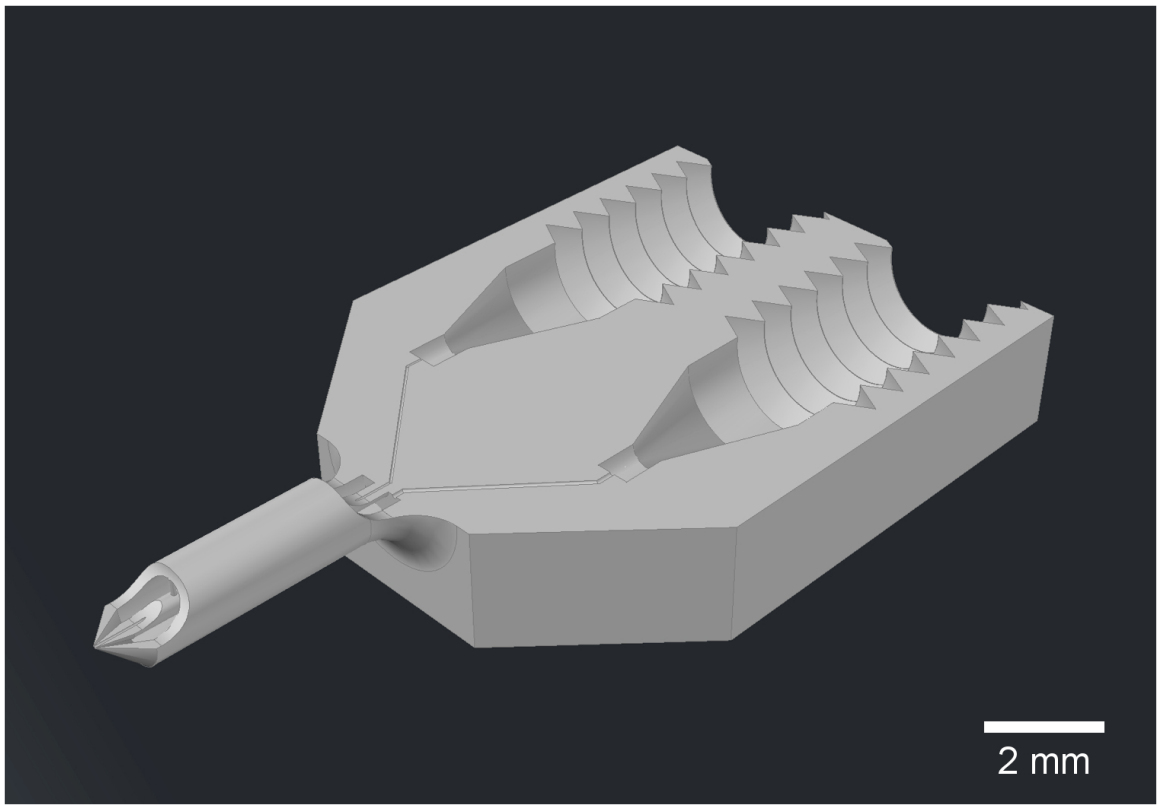

Figure 25: Conceptual drawing of 3D printed GDVN with supply fitting ports printed directly. A submicron resolution device of this size could take up to 2 months to build even with the fastest submicron printing currently available.

actual total volume of 0.47 cm^3. Unfortunately, even the Photonic Professional GT system described above would take no less than six months to print a device of this size.

To realize submicron resolution 2PP 3D printing as a feasible GDVN fabrication technique, it was necessary to minimize the GDVN size to optimize writing time. Taking into account the size of commercially available capillary tubing and the need to connect and secure such lines, the target device size was determined to be about 1 mm^3 (defined at the boundaries of the writing volume, and not the actual total volume of the device). The Photonic Professional GT was found to be fully capable of printing high-resolution millimeter-sized nozzles within hours. Initially, using the system described above, a

device of this size was printed in about 24 hours. To reduce the printing time further, GDVN nozzles were printed using a 25x, NA=0.8 objective lens with a slicing distance of 1 μm and hatching distance of 0.5 μm. Using these parameters, submicron resolution printing was performed within many 400 x 400 x 10 μm^3 units that were stitched together to form a 3D printed GDVN within the 1 mm^3 target volume in less than four hours.

Two design prototypes were printed and tested. Three iterations of prototype 1 were tested and did not jet properly. Following an analysis of internal structures using optical imaging in an index-matched medium, Glycerol (Montanero et al., 2010), design improvements were implemented in prototype 2. Two prototype 2 nozzles were printed using different photoresists, IP-S and IP-L, and were tested for basic GDVN functionality. Following positive jetting results in these tests, IP-S was selected as the medium for an additional set of nine nozzles, printed successively over a single weekend to test for reproducibility. Index-matching optical microscopy and X-ray tomography were used to analyze the internal structure of the prototype 2 nozzles, and improvements in reprints lead to straight jetting. Prototype 2 nozzles were used in serial crystallography experiments with the XFEL beam at the LCLS to collect X-ray diffraction patterns.

3.2 Prototype 1

3.2.1 Design

The design for prototype 1 is laid out in Figure 26, along with an SEM image of one of the actual printed nozzles. The nozzle was drawn using AutoCAD 2010 (Autodesk, Mill Valley, CA). Originally this design was made with the assumption that stitching would only be done between 400 x 400 x 400 μm^3 units. The dashed line in

Figure 26 outlines one of these volumetric units. It specifically contains the parts of the GDVN that are though to be the most important to the jetting process. The intention was to provide the best spatial resolution for these features. (Improvements to this concept were included in prototype 2 to deal with the potential problem of gas and liquid

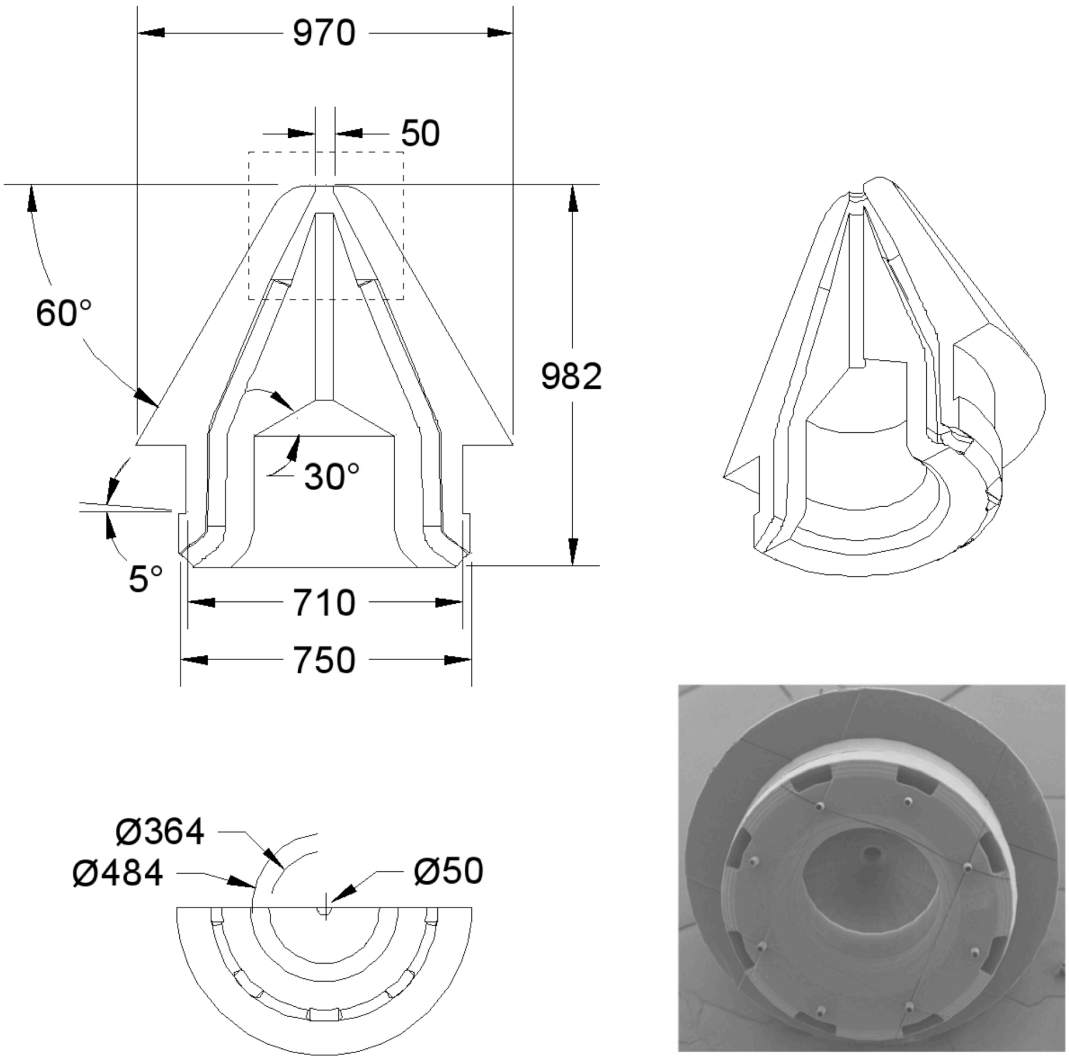

Figure 26: Prototype 1 design with SEM image of actual printed nozzle. Small pegs were added to the printed nozzle to help with removal of uncured photoresist from the central capillary receiving port.

permeation through stitched interfaces, described later.) The prototype 1 design also included a large bevel surrounding a receiving port for a 360-µm outer / 50-µm inner diameter liquid supply capillary. A bevel was placed surrounding the entrance to this port to act as a "glue-guide" to draw a drop of epoxy completely around the inserted capillary with capillary action. Eight gas ports were placed to surround this liquid supply port. At the base of the device they were intentionally bent away from the glue-guide in order to avoid contact with glue. The eight gas ports were made to extend into an accelerating gas chamber within the volume defined by the dashed line in Figure 26. After the liquid supply capillary was glued in place and the epoxy was set, the capillary was fed through a beveled stainless steel sleeve until the nozzle was brought to rest on the beveled end of the sleeve. Epoxy was then applied to fix this in place (Figure 27). A recess around the cylindrical base of the nozzle was designed to collect excess epoxy during this process. The recess was also intended to act as a hook to anchor the nozzle. This recess and hook were not included in prototype 2, and their absence was not found to be in any way detrimental. To complete the mounting process a second glass capillary was inserted into the proximal end of the gas transport tube to introduce the Helium sheath gas. Finally, the proximal end of the tube was sealed with epoxy in order to provide a gas-tight seal and to fix all capillaries in place. After the epoxy was fully cured, the stainless steel tube was attached to a standard GDVN holder, which in turn has connections to the nozzle rods used for in-vacuum sample injection (Weierstall, 2014).

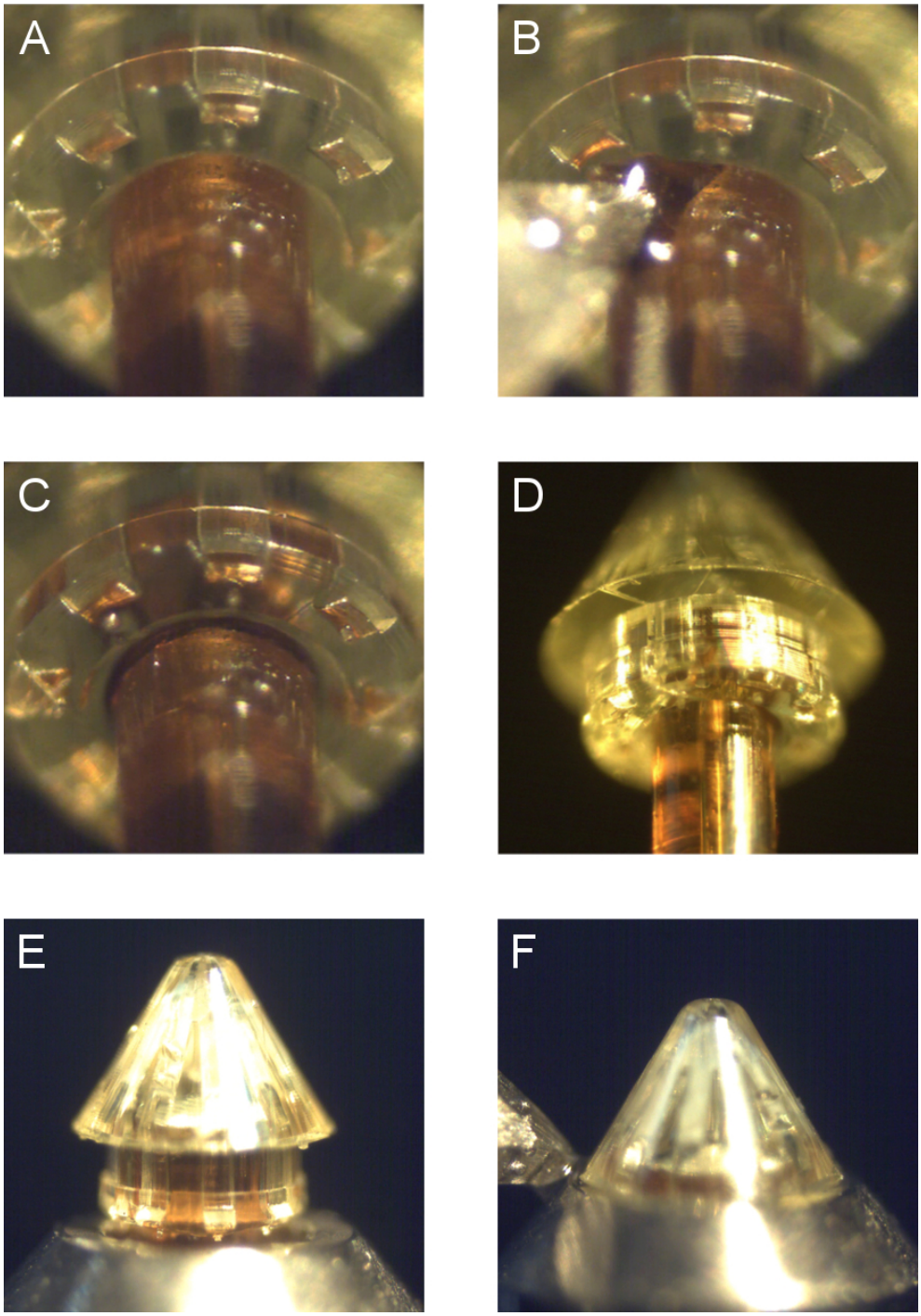

Figure 27: Gluing of the 360-µm outer diameter / 50-µm inner diameter liquid supply capillary into the prototype 1 3D printed nozzle, and subsequent gluing of the nozzle to a stainless steel sleeve: A) capillary inserted; B) gluing using the tip of a hypodermic needle attached to an electronic micromanipulator; C) epoxy is drawn completely around the capillary because of the glue-guide; D) image of nozzle glued to the capillary; E) capillary and nozzle fed into the beveled end of a stainless steel sleeve and held in place by friction; F) gluing the nozzle in place by rotating the sleeve and nozzle relative to the stationary glue applicator.

3.2.2 Results

One major problem with the fabrication of prototype 1 had to do with the difficulty of removing uncured photoresist from the gas supply and liquid channels. Small pegs were added to the design (see SEM image in Figure 26) to allow the developer access to the inner channels. Immersion of the nozzle in Acetone for 45 minutes was necessary to remove photoresist from the central lines. This aggressive solvent appeared to degrade the nozzle structure beyond this point, so that prolonged development was not reasonable. As a result, not every gas channel was free of photoresist; in one instance only a few were clear, while in another instance nearly all appeared to be clear. This was observed initially with optical microscopy, although not with definitive clarity. These nozzles were mounted and tested for jetting. As seen in Figure 28, the result was a spray instead of a jet, which only worked in atmosphere, since the spray immediately lead to icing when operating in vacuum. Another problem was that gas appeared to be leaking through the side of the outer nozzle cone (Figure 28B).

It was desirable to image the interior of the prototype 1 nozzles in order to determine the cause of failure. The indexing matching method was used (Montanero et al., 2010). Glycerol was placed in a disposable spectrometer sample holder and a backlight was used to acquire an accurate cross section of the printed nozzles as seen through an optical microscope objective lens. The mounted nozzles were immersed in the medium, and it appeared that capillary action from the liquid and gas supply lines pulled Glycerol into the interior, removing any air bubbles. This eliminated nearly all optical distortion, allowing for an accurate view of the inner sidewall profile of the

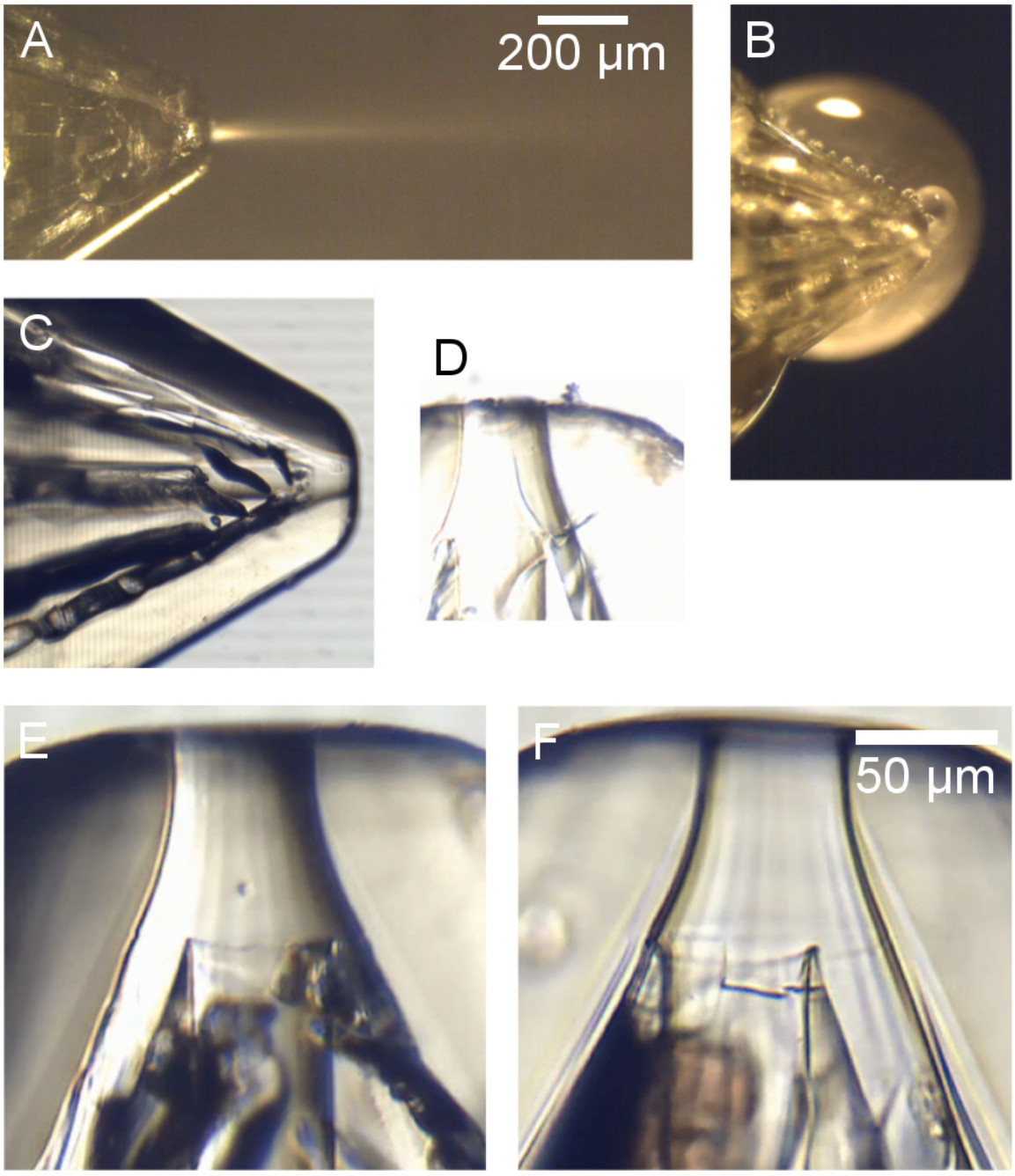

Figure 28: Testing results for prototype 1: A) jet testing resulted in a spray profile when exhausting into atmosphere (only ice resulting in vacuum); B) an array of air bubbles was visible inside of a large water drop; the individual bubbles grew in response in increasing the gas pressure, suggesting that gas may have been leaking through a stitching interface; C) imaging of the interior of the nozzle when immersed in Glycerin showing what appears to be poor formation of interior parts; D) cracking (probably due in part to abnormally high pressure tests); E) and F) view of inner cone in two separate nozzles showing the inner cone off center; in one case the tip of the cone is nearly touching the sidewall. Images C though F were acquired after jet testing.

printed nozzle (Figure 28C through F). The condition of the nozzle as seen in Figure 28 C indicated that the interior of the nozzles were not formed well. The images in Figure 28E and F indicated that the interior cone was off-center, and in one case the tip of the cone nearly touches the sidewall (Figure 28F). It was not clear whether or not this was the condition of the inner cone before jetting, since imaging was not done until after jet testing, but it certainly accounted for the spray profile seen in Figure 28A).

The exact causes of these obstructions and deformations are not known. However, possible causes include inefficient removal of photoresist and/or the deposition of residual as the developer evaporates. These ideas are discussed in more detail in the discussion regarding prototype 2.

3.3 Prototype 2

3.3.1 Design

The prototype 1 fabrication was subject to an additional adverse effect that was based on software rendering. A polygon-like surface quality had been carried through to the printing. It appeared that the extreme size of the device relative to its resolution (i.e. the LEGO®-city analogy) exceeded the limits of AutoCAD's ability to render smooth surfaces in the ".stl" format. Although not necessary a candidate cause for device failure, this was not a desirable feature. This problem was fixed for prototype 2 by importing the design into the Inventor Professional software program (Autodesk, Mill Valley, CA), which was capable of rendering the desired surface smoothness. Besides this, several fundamental changes were implemented in prototype 2.

To maintain the desired nozzle-within-a-nozzle geometry with both nozzles of ideally cylindrical symmetry while yet significantly increasing the size of the gas supply ports, a rib-like support was used to center the inner nozzle. As before, to optimize writing time, the nozzle was designed to be as small as possible, while taking into consideration the need for the device to have enough material to withstand high gas and liquid pressures and to couple feasibly to the liquid and gas supply lines. Figure 29 shows several views of the nozzle design as well as a cross section.

Since jet formation and stability are most affected by the shape and relative position of the inner and outer nozzle housing near the exit orifice, these features were modeled after the profile of the traditional GDVN shown in Figure 30, which was known to produce a straight and steady jet. This GDVN was immersed in Glycerol and the sidewall profile was traced using Logger Pro 3 (Vernier, Beaverton, OR). The plotted coordinates were put into an AutoCAD script that was used to draw the sidewall profile. To assure symmetry, only half of this traditional GDVN profile was modeled and then revolved about the flow axis when drawing in AutoCAD.

Because earlier trials with prototype 1 suggested that vertical interfacial regions between fast-written volumes were possibly permeable to gas, the structures mentioned above as well as the termination of the to-be-inserted sample capillary were all designed to be situated within the 400 x 400 x 400 μm^3 unit outlined in Figure 29B. By using a smaller supply capillary (150-μm outer / 50-μm inner diameter), the necessary size of the printed central channel was significantly reduced, allowing the volume defined by the stitched line to include the tip of the inserted glass capillary. The liquid is transferred

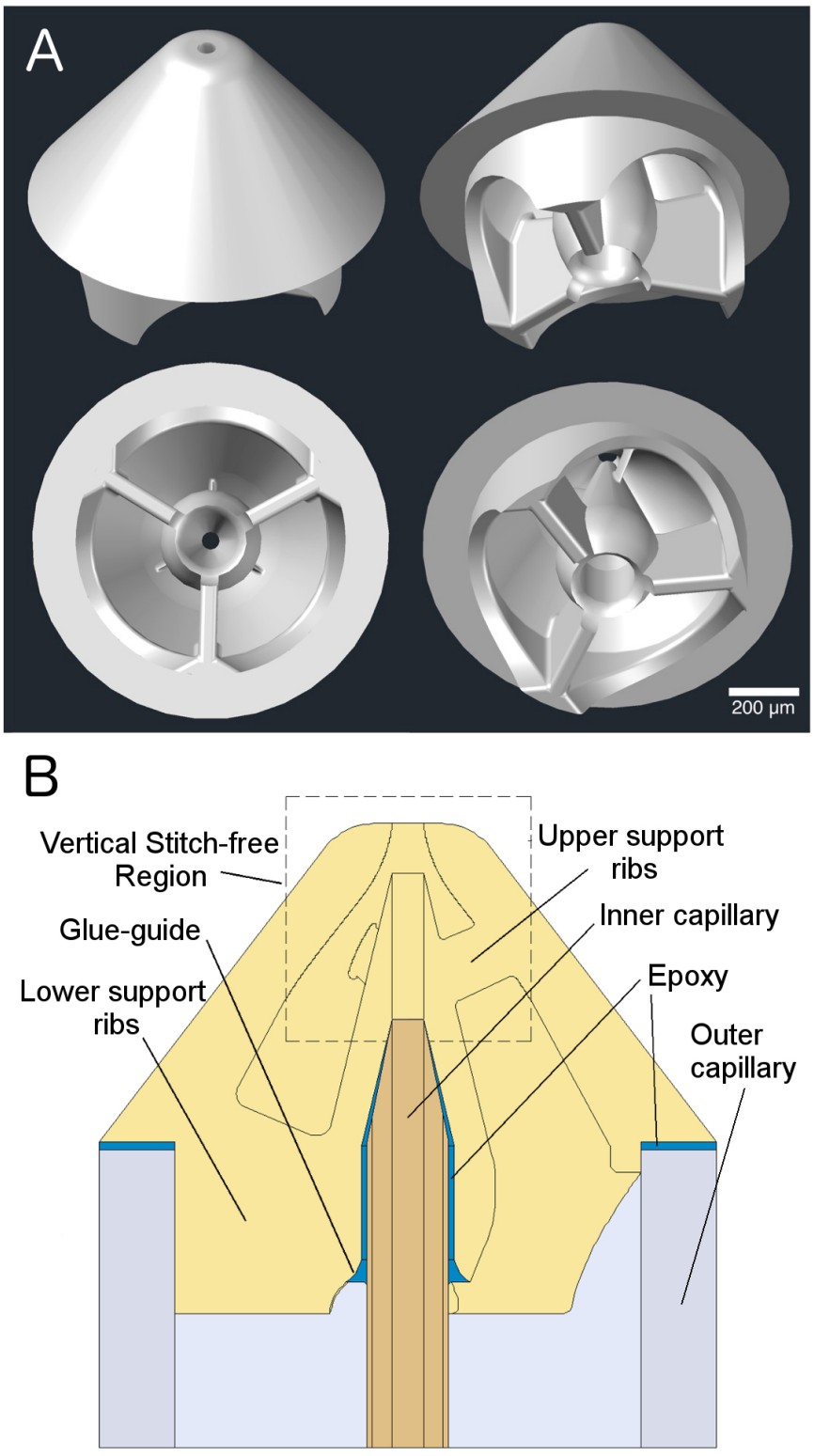

Figure 29: A) views of the prototype 2 nozzle design; B) cross section diagram of the printed nozzle with both inner and outer capillaries glued into place.

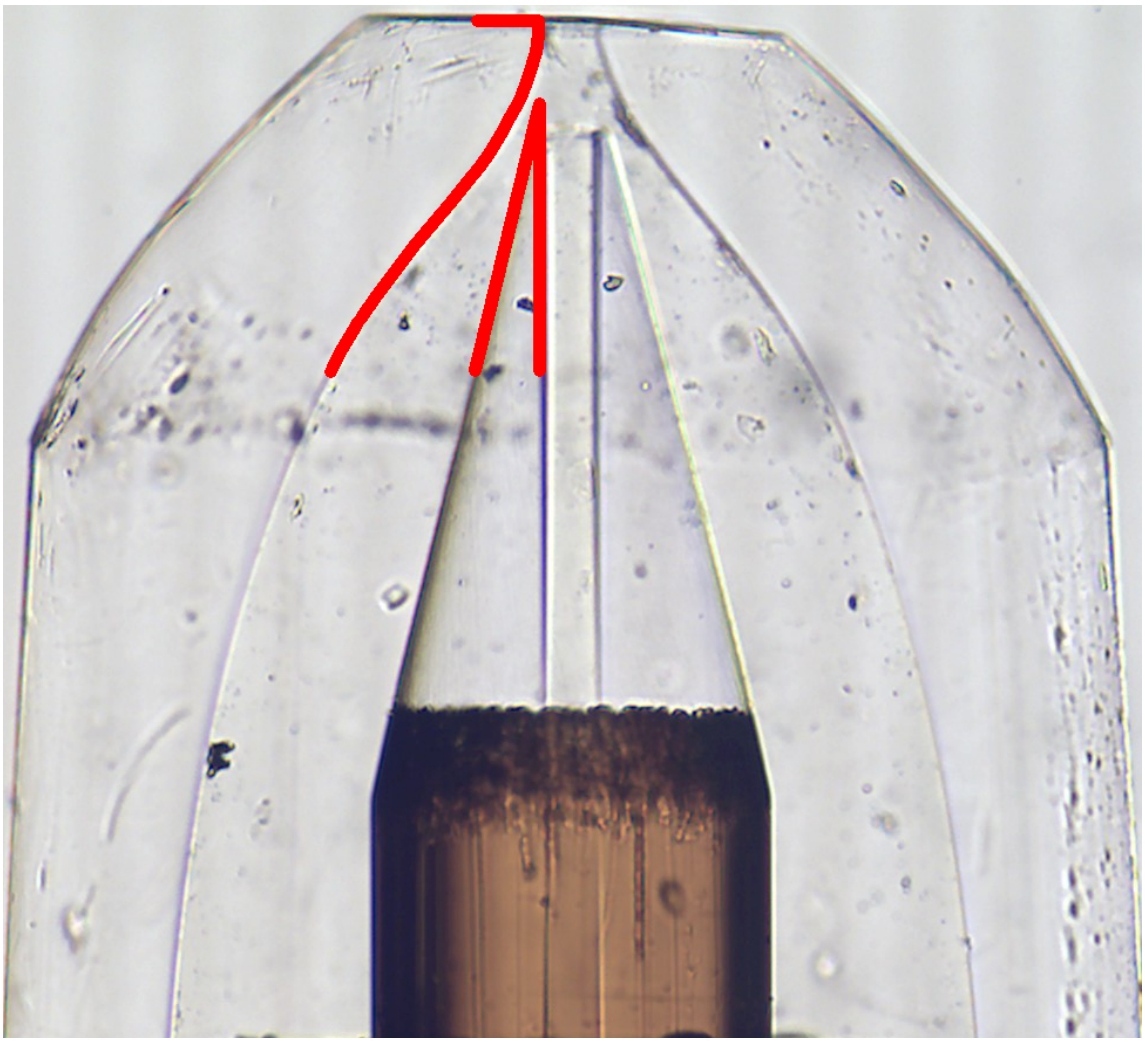

Figure 30: Image of a glass-style GDVN when immersed into an index-matched medium (Glycerol), showing an undistorted view of the gas aperture profile and inner capillary position. The contour indicated by the red line was used to derive the CAD model for prototype 2. Inner diameter of the inner capillary is 50 µm.

from the inserted capillary tip directly into this vertical-stitch-free region and exits through the following channel without leakage of either gas or liquid through the interior 3D printed wall.

As indicated previously, prototype 1 trials indicated that small channels of around 50 to 100 µm in diameter required excessively long development times using Acetone to

remove as much uncured photoresist as possible without distorting the nozzle structure. These long incubation times may have been responsible for the distorted internal nozzle structures that were observed. Several design characteristics of prototype 2 aimed to increase the efficient removal of uncured photoresist during development (Figure 29). Using a 150-μm outer / 50-μm inner diameter capillary with a cone profile allowed for more open space in the nozzle design in order to reduce development time of the printed nozzle by avoiding confinement. Further maximization of open space was accomplished by forming the lower end of the inner nozzle housing into a bulb-like profile. To avoid trapping photoresist within the gas cavity and the inner capillary receiving port, three semicircular voids were included in the cylindrical sidewall of the outer housing, and the base of the inner nozzle housing was elevated above the substrate. The outer nozzle hull was tethered to the inner nozzle housing with two sets of supports. Each set consisted of three support ribs positioned 120 degrees apart with respect to the central axis, one set being 60 degrees out of phase with respect to the other. All these aspects were implemented to provide good developer access to the internal volume to minimize development time.

The glue-guide from the prototype 1 design was used again with a fillet around the entrance of the inner capillary receiving port. Again, after the liquid supply capillary is inserted, this recess provided a pathway for a droplet of epoxy to be drawn completely around the capillary through capillary action, bypassing any need for multiple applications of glue and/or complicated movement by the applicator, nozzle, or capillary structures. The glue finds its way around the capillary at a much faster rate than the rate at which it is drawn coaxially up the much smaller cavity between the capillary outer wall

and the receiving port wall. With the circumference of the recess is filled, the glue propagates upwards in an approximately uniform manner. The amount of glue necessary can be calculated from the geometry of the receiving port for the liquid line.

However, one significant difference between the glue-guide in prototype 1 and prototype 2 was the direction of the concavity of the profile: concave-up in prototype 1 (Figure 26) and concave-down in prototype 2 (Figure 29B). Gluing using the prototype 2 glue-guide design was found to be more difficult. Presumably, with the glue on the end of an applicator forming naturally into a sphere, a concave-up curvature intersects with the incident glue sphere in a manner that increases to likelihood that the initial point of contact is within the glue-guide. This is important since glue that is applied outside of the glue-guide can find its way to unintended locations within the inner nozzle structure. The use of the concave-down profile was a significant oversight. However, this did not prove fatal, as careful use of an approach angle of the glue applicator allowed effective use of the concave-down glue-guide of prototype 2.

As before, the overhanging structure that rests upon the outer capillary abutment provides the stopping point for when the entire structure (including the glued-in sample capillary) is inserted into and glued to a tube that acts as a carrier for gas to flow coaxially around the inner capillary. The diameter of the cylindrical base was made to match the inner diameter of the gas transport tube, so that ideally the inserted nozzle would be held in place by friction while gluing.

The buoyancy of cured structures makes it possible to produce deformities if there is not sufficient anchoring of structures during the printing process. The overhanging structure that rests upon the outer capillary abutment was subject to this effect, as will be

seen below, but without any noticeable effect on nozzle performance. The unintentional production of "free-floating" structures is much more problematic. Therefore, careful attention was given to the continuous attachment of the outer housing to the inner housing with each successively written layer. Fillets were incorporated throughout the design to provide increased strength and more favorable gas flow.

3.3.2 3D Printing and Imaging

Nozzles were printed on the Photonic Professional GT system using a 25x, NA=0.8 objective lens with a slicing distance of 1 μm and hatching distance of 0.5 μm. The resolution is defined by these parameters, although theory for this objective lens predicts a voxel size generated at the beam focus based on FWHM of 0.612 μm in x-y and FWHM of 3.4 μm in z. By using the larger objective lens, a larger volume was traced out, yet with the same moving precision that is accomplished when using a smaller objective lens. Overlap of voxels according to the printing parameters mentioned above resulted in submicron resolution prints within volumetric units of up to 400 x 400 x 10 μm^3 that were stitched together to form the nozzle. Nozzles printed in IP-S resist showed better overall fabrication quality compared to a nozzle printed in IP-L resist. IP-S nozzles were developed by incubation (unstirred) in mr-DEV 600 (micro resist technology) for 45 minutes followed by an isopropanol bath for 10 min.

The vertical edges of the 400 x 400 x 400 μm^3 volume defined by the dashed line in Figure 29 were visible with optical microscopy as parabolic cross-sections through the cone of the nozzle. Thin horizontal z-stitching marks spaced

10 μm apart were also visible throughout the entire structure (Figure 31A). Optical microscopy in Glycerol confirmed the 10-μm spacing and gave a projected view of both types of stitching under certain lighting conditions (Figure 31B). The horizontal slices all look identical at this resolution. Possible disruptions in the continuity of the sidewall profile appeared as shallow 1 to 2 μm-sized dips at the edge of each horizontal stitched region (inset of Figure 31B). Positioning errors between the vertical edges of fast-written units around the circumference of the nozzle were more apparent, ranging from 1 to 5 μm (inset of Figure 31A). These errors were likely the result of upward buoyant flexing of the overhanging structure during printing (see Figure 32A), as opposed to inaccuracy of the printing system itself.

It should be noted that the nozzle shown in Figure 31B (and Figure 32B below) was unintentionally subjected to the development time of 4 hours as opposed to the 45-minute time that was used for all other prototype 2 nozzles. When tested this nozzle was the only nozzle that did not produce a jet. Whether or not this is due to the increased incubation time is not clear. The appearance of the nozzle was nearly identical to the others when viewed with the index-matching method, except perhaps slightly more defined stitched interface projections. Differences in surface smoothness and stitching errors were not detectable. This nozzle was originally provided as part of the two prototype 2 nozzles that were initially tested (it was a third nozzle). Its choice for use with the index matching technique was initially a consequence of the desire to identify differences in

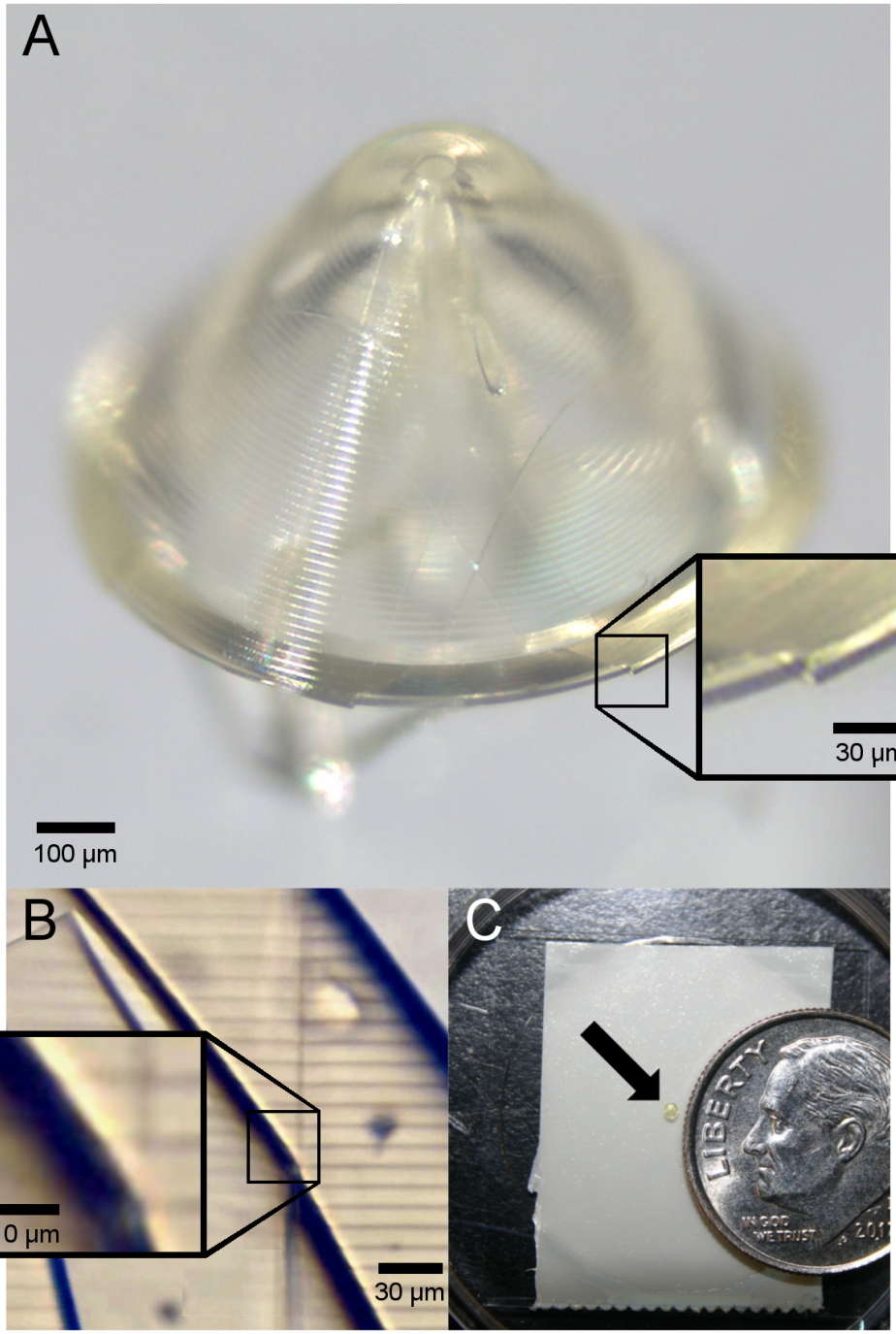

Figure 31: A) 3D printed prototype 2 GDVN attached to a glass substrate. Stitching errors between the 400x400x400 μm^3 fast-written units are visible as vertical parabolic cross sections through the device resulting in steps at the circumference as shown in the insert. B) Index-matched image (nozzle immersed in Glycerol) showing projection of both vertical and horizontal stitching lines. Horizontal stitching lines cause very little disruption to continuity of features on the inner sidewall (insert) while vertical stitching can result in larger displacements as seen in the insert of A. C) 3D printed GVDN next to a U.S. dime.

internal structure and to preserve other nozzles for use in serial crystallography tests (it is difficult to remove all Glycerol from the interior of mounted nozzles).

After the testing of the 6 from the set of 9 nozzles and also after the serial crystallography tests (all described below) two of the remaining unmounted nozzles were immersed in Glycerol to verify that Figure 31B is a fair representation. One was glued to a glass plate while the other was mounted to the inner capillary only. In both cases it was difficult to completely remove the air from within the nozzles. Suggesting that complete mounting is necessary to achieve complete removal of air from within the nozzle. Close inspection of the nozzle that was connected to the inner capillary only appeared nearly identical to the nozzles shown in Figure31B. As mentioned above, differences in surface smoothness and the stitching errors were not detectable. However, during handling the inner cone became partially disconnected from the outer cone, and it was decided that the overdeveloped nozzle more a more accurate representation for use in Figure 31. The nozzle that had been glued to a glass plate unsurprisingly did not appear to have any air removed when immersed into the Glycerol; however, this air trapping provided excellent contrast and is used in Figure 32D and E.

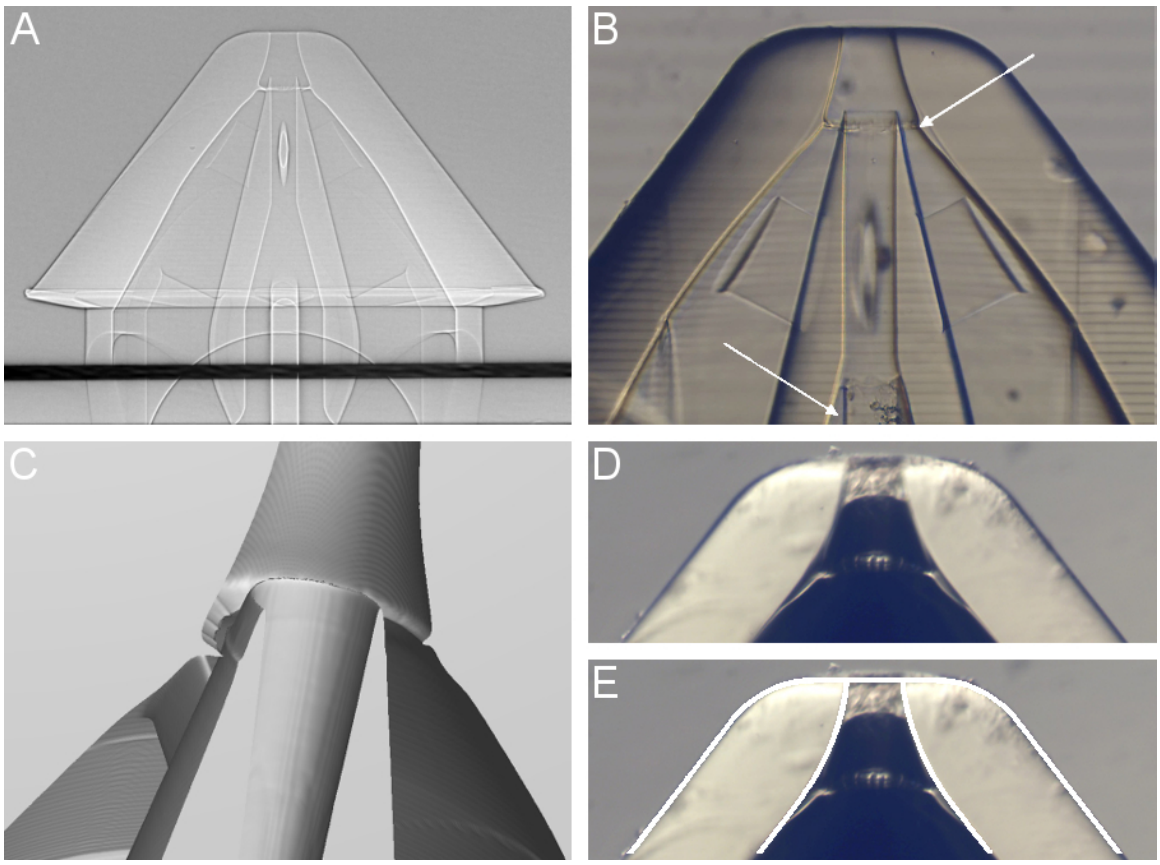

Figure 32: A) X-ray projection of a 3D printed prototype 2 nozzle on a glass substrate compared to B) an index-matched bright field microscopy image (nozzle immersed in Glycerol) of a 3D printed prototype 2 nozzle with supply lines attached (supply capillary tip visible at bottom of image, bottom arrow). In B), some remaining uncured photoresist is visible (top arrow) which accumulated in the narrowest area of the gas channel surrounding the end of the liquid line. The original edge of the sidewall profile is also visible. C) Cross sectional view from 3D surface renderings using X-ray tomography data, showing the accumulation near the tip in detail. Note that the cross section plane is not necessarily aligned with respect to the nozzle axis (the cut may be tilted). D) Nozzle in Glycerol with air bubble trapped inside. The original edge of the sidewall profile is clearly distinguished from the deposition and E) matches the sidewall profile from the original CAD file.

Figure 32 shows index-matched images and X-ray imaging data of printed nozzles. An accumulation of material was visible near the tip in every nozzle. High-resolution renderings using X-ray tomography data reveal the accumulation in detail (Figure 32C). The original edge of the printed profile can be seen in the index-matched images (Figure 32B and D), suggesting post-printing deposition

and curing. One possibility is that as the developer evaporated, residual uncured photoresist accumulated at this point and eventually hardened, a problem that might be solved with multiple development stages with fresh developer.

The tomography experiment was conducted at the TopoTomo beam line at ANKA (Rack, et al., 2009) using a filtered white beam mode with 0.5 mm Aluminum, an indirect detector consisting of an Lu(2)SiO(5) 12 μm thick scintillating screen, 10x magnification objective lens and PCO.dimax camera with an effective pixel size of 1.22 μm. Resulting projections were flat field corrected to remove background defects before the phases were retrieved (Paganin et al., 2002) to increase contrast. A filtered backprojection algorithm (Vogelgesang et al., to be submitted) was then used to reconstruct 3D volumes from the preprocessed projected thickness data.

3.3.3 Connecting Sample Lines

Prototype 2 was mounted with the same custom mounting stage used for prototype 1, in which a commercial micromanipulator was used to glue the liquid and gas supply lines into place. The 3D printed nozzle was held in place using vacuum tweezers (Figure 33c) that were fitted with a custom headpiece. A MicroTight® union from IDEX was attached to an arm extending from the face of a 3-axis micrometer stage (Figure 33e). After removing debris and liquid that accumulated in the interior of the inner capillary during the cone grinding process, the inner capillary was fed, starting with the unground end, through the union and held in place with MicroTight® fittings (Figure 33d). With the vacuum tweezers

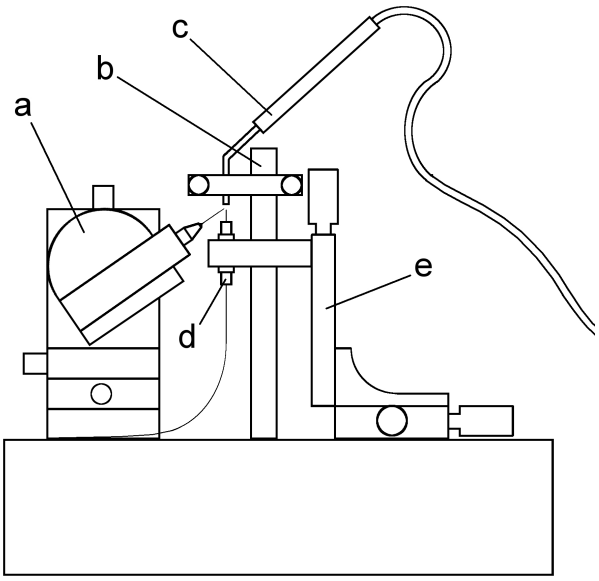

Figure 33: Diagram of mounting stage: (a) electronic micromanipulator with hypodermic needle applicator; (b) apparatus for securing (c) vacuum tweezers in place; (d) fittings for holding capillaries securely; (e) manual micromanipulator for positioning and inserting a capillary into the nozzle held by vacuum tweezers (c).

holding the 3D printed nozzle in place, the cone-end of the inner liquid capillary was inserted into the central receiving port of the printed nozzle using the micrometer stage. Once in place, the vacuum tweezers system was turned off.

By design there was a slight mismatch in angle between the inserted capillary cone and the cone profile of the receiving port. The angle of the capillary was chosen to be "sharper" to allow the glass tip of the inserted capillary to make hard contact with the nozzle structure at the capillary tip, providing a hard barrier to prevent overgluing but allowing room for glue to optimally fill in the void.

As with prototype 1, a drop of fast-curing epoxy was put in contact with the end of a hypodermic needle that was attached to the micromanipulator so that a small epoxy sphere adhered to the needle tip. The needle tip was positioned near

the gluing target with preprogrammed coordinates and then controlled manually for the gluing process (Figure 34A).

As described in section 3.3.1, the concave-down profile, in contrast with the concave-up profile from prototype 1, required a more carefully aligned approach vector. Once established, the "glue-guide" worked as intended and drew the epoxy completely around the inserted capillary with capillary action (Figure 34A). The epoxy bond between the sample capillary and the printed nozzle was allowed to fully cure overnight.

The mounting stage was then modified slightly by replacing the vacuum tweezers with the gas transport tube, and then repositioning the apparatus that formerly held the vacuum tweezers so that the applicator needle could approach the nozzle directly from the side (Figure 34B). (The first set of prototype 2 nozzles was connected to stainless steel gas transport tubes, which had previously been given a steep bevel to match or exceed the nozzle angle. Stainless steel was chosen in order to make the finished nozzle robust. The second set of prototype 2 nozzles was connected to glass gas transport tubes, so that the inside was visible. This visibility was important for the testing of reproducibility.) With the inner capillary glued in place, the nozzle inserted into the distal end of the gas transport tube and ideally held in place by friction as with prototype 1. However, although the nozzle was designed to match precisely with the stainless steel gas transport tubes, the inner diameter of the glass gas transport tubes did not match closely enough to hold the nozzles with friction and were much more difficult to glue. For the nozzles that used glass sleeves, the micromanipulator was able to glue in place

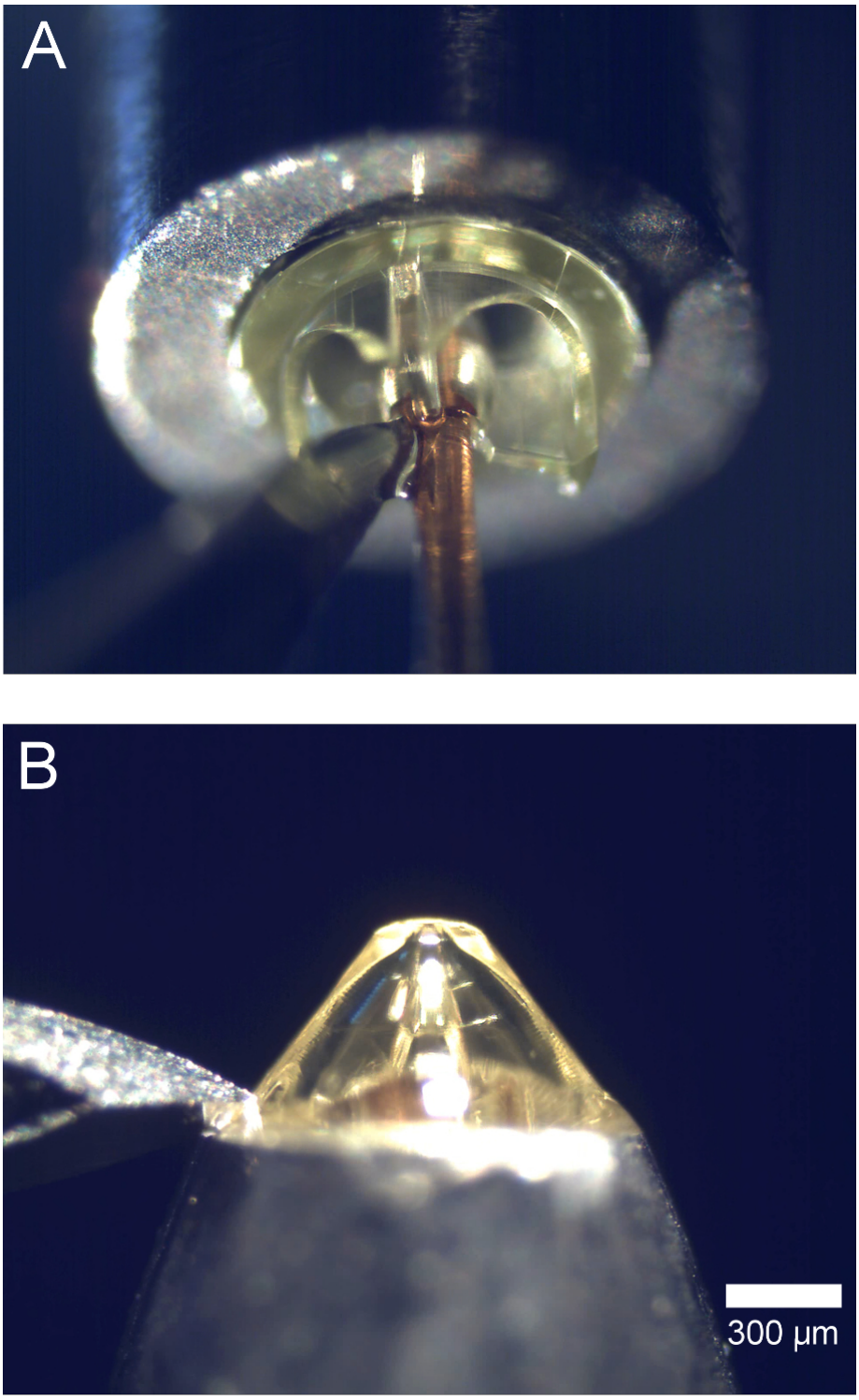

Figure 34: A) the inner capillary is glued into the 3D printed prototype 2 nozzle by applying epoxy with a micromanipulator; B) the nozzle with the attached capillary is glued into a steeply beveled stainless steel tube. This method is essentially identical to the method shown in Figure 27.

a substantial portion of the nozzle (perhaps as much as 120° about the circumference). After curing, nozzles were sufficiently secured to the glass sleeves to allow for rotation and a second gluing step. This process was repeated until the nozzles were completely glued in place. The mounting process was completed in exactly the same way as was described at the end of 3.2.1.

3.3.4 In-lab Testing

Three nozzles were tested with pure water and helium gas to determine whether the printing resolution and symmetry were sufficient to produce a straight jet and to test whether the nozzles performed in a reproducible manner without fracturing. The nozzles did not jet straight in either vacuum or atmosphere. The nozzles required very little helium gas pressure to operate compared to the traditional GDVN. A 100-μm inner diameter capillary tubing of approximately 2 meters in length was used for the gas supply line with a gas pressure for the 3D printed nozzles of about 50 psi compared to about 300 psi for traditional GDVNs as measured upstream of the supply capillary. The minimum sample flow rate was 5 μl / min, which is typical of traditional glass nozzles. The angular deviation of the jet trajectory from the nozzle axis was highly dependent on helium gas pressure. The minimum off-axis jet angle was about 8 degrees for each nozzle.

Comparative tests of the three nozzles were performed by taking videos of each nozzle jetting while rotating each nozzle slowly around its central axis. It was necessary to refocus the microscope at times due to a slight precession of the nozzle as seen from the camera frame of reference. For these tests helium gas

pressure, water flow rate, and supply capillary length were made as identical as possible by maintaining the helium gas regulator in a fixed position between nozzle changes, using an in-line digital liquid flow meter, and cutting the capillaries to equal lengths within 1 cm. Imaging points during rotation were chosen at 60-degree intervals based on centering of repeated projected nozzle features as shown in Figure 35. Collections of these images as captured in sequence were compared side-by-side and matched according to the angular deviation of the jet from the nozzle axis (Figure 35). In order to make accurate comparisons, corrective image rotations using image-editing software were performed so that the projected external nozzle cone angle was symmetric horizontally about the image window. The nozzles did jet reproducibly.

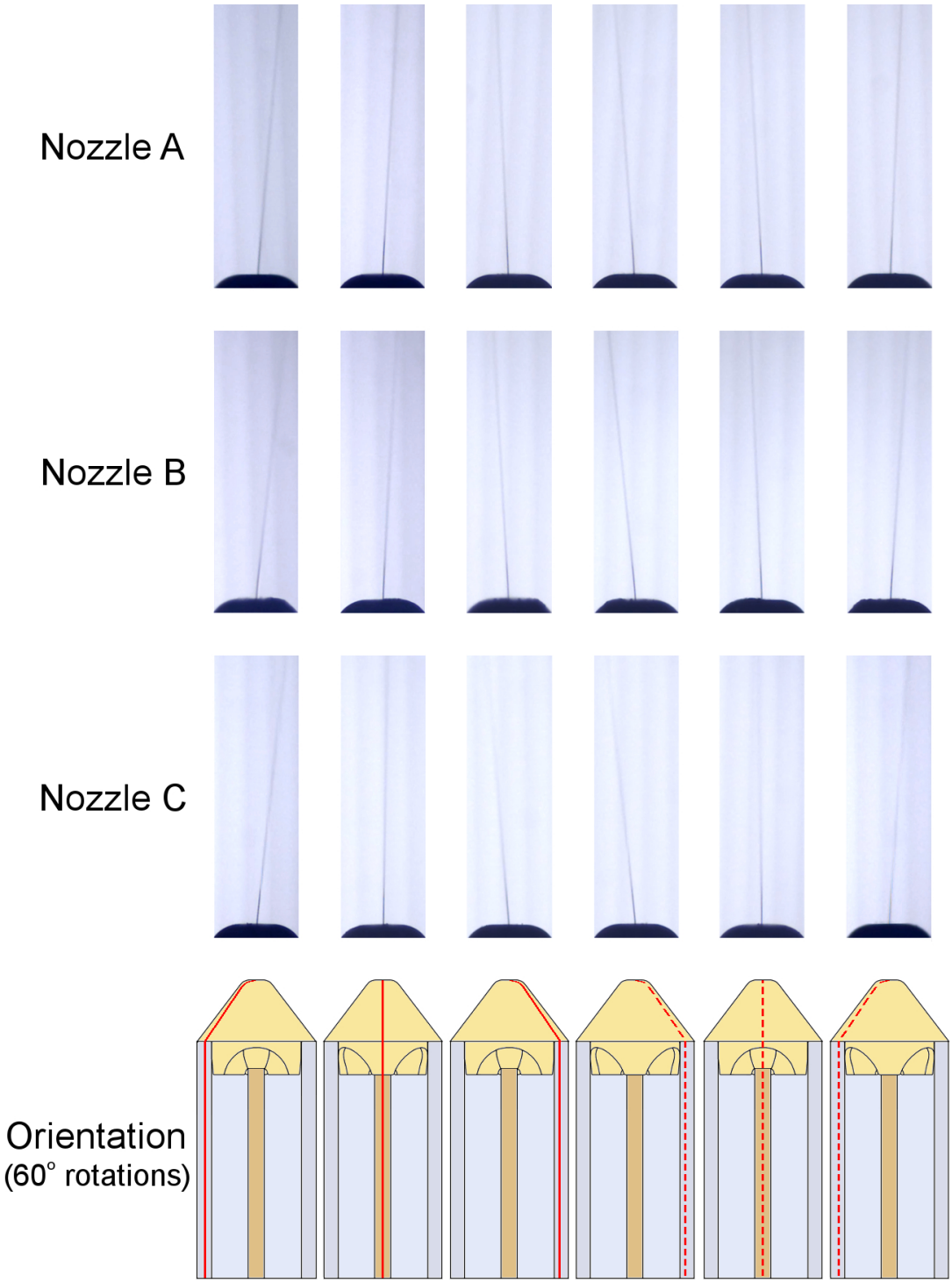

Figure 35: Reproducibility of angular deviation of the jet from the nozzle axis for 3D printed prototype 2 nozzles A, B, and C when jetting water in vacuum. The nozzles are rotated by 60 degrees between each image. A deviation angle of about 8 degrees relative to the nozzle axis was observed for all three nozzles.

3.3.5 Serial Crystallography

Two nozzles were used in actual SFX experiments at the CXI station at the LCLS to test whether the IP-S resist material was biocompatible with protein crystals and of sufficiently low background. Background produced by the nozzles when in close proximity with the x-ray beam was measured at 10% and 100% transmission. The background was found to be very similar to the background scattering from glass nozzles. Crystal screening was performed using the nozzles for two membrane proteins (undisclosed for collaborative reasons). A snapshot diffraction pattern obtained with a prototype 2 printed nozzle at CXI is shown in Figure 36, with sharp Bragg spots extending to 4-Å resolution. This pattern was collected with an X-ray energy of 8.7 keV, using 40 fs XFEL pulses, with a distance of 138 mm between sample and detector. There was no evidence of the printed nozzles affecting diffraction quality compared to patterns obtained from the same samples using standard GDVN nozzles. Overall, the 3D printed prototype 2 nozzles appeared to perform very similar to the glass-style GDVN.

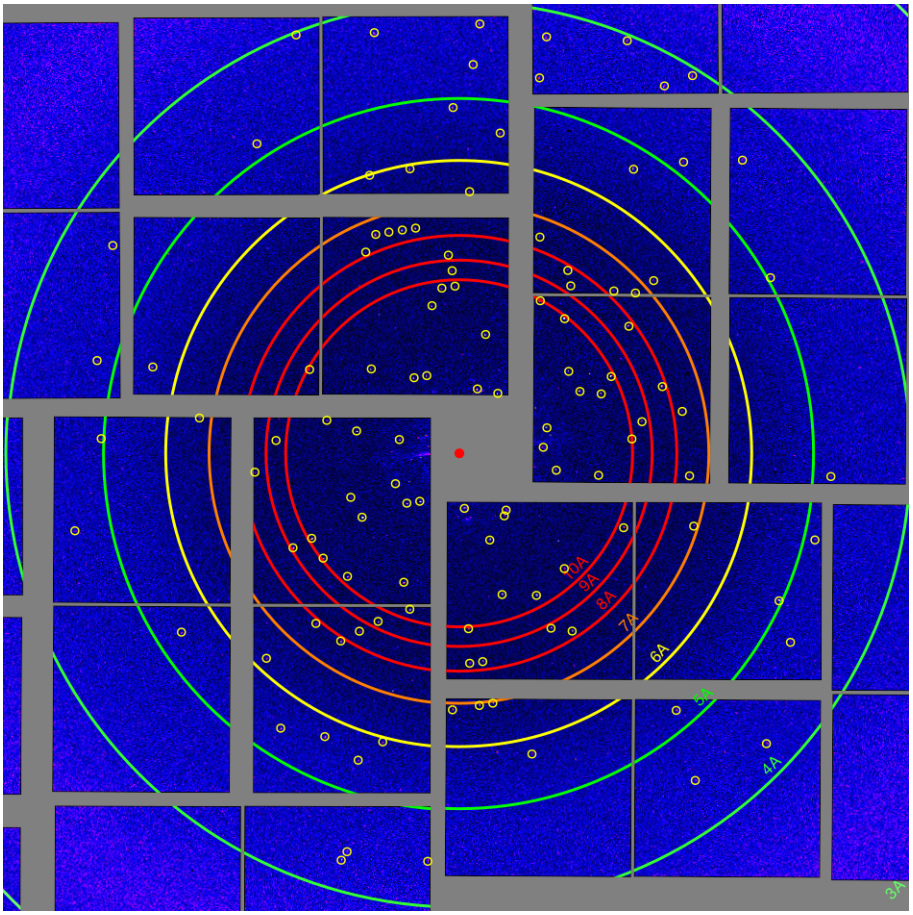

Figure 36: Example of membrane protein crystal diffraction obtained using a 3D printed nozzle, with sharp Bragg spots extending to 4 Å. Circles are superimposed around Bragg spots for visibility. No difference was observed between the quality of diffraction from samples run in the printed nozzle compared to a glass capillary GDVN.

3.4 Prototype 2 with Improved Development Procedure

Additional prototype 2 nozzles were printed, and an improved development procedure was used that resulted in the removal of the residue seen in Figure 32. Multiple rinses with fresh developer were performed. X-ray tomography was again used to examine the nozzles. Figure 37 shows the tomography images. One of these nozzles was connected to supply lines and tested with pure water. The resulting jet was straight and the gas pressure required for operation was comparable to the glass-based GDVN. The rotation procedure described previously was applied and no angular variation in the jet trajectory was observed. The jet is shown in Figure 38.

This prototype 2 nozzle was a variant nozzle in two ways. Firstly, the smaller set of rib supports were not out of phase with respect to the larger rib supports, but were rather aligned as seen in Figure 37. It is thought, though not proven, that this change does not contribute significantly to the straight jetting since the supports are symmetric about the flow axis in either case. It also is thought unlikely that this change would have a significant effect on the development procedure, whereas multiple rinses with fresh developer are thought to have been primarily responsible for complete removal of the residue. Secondly, the rendering corrections described at the beginning of section 3.3.1 were not applied. This can be seen in Figure 37 as a polygon-like surface quality. Evidently, this has no effect on the jetting quality as far as angular variation is concerned – a result that is convenient from a practical point of view since smoothly rendered surfaces result in very large CAD files that can be difficult to edit.

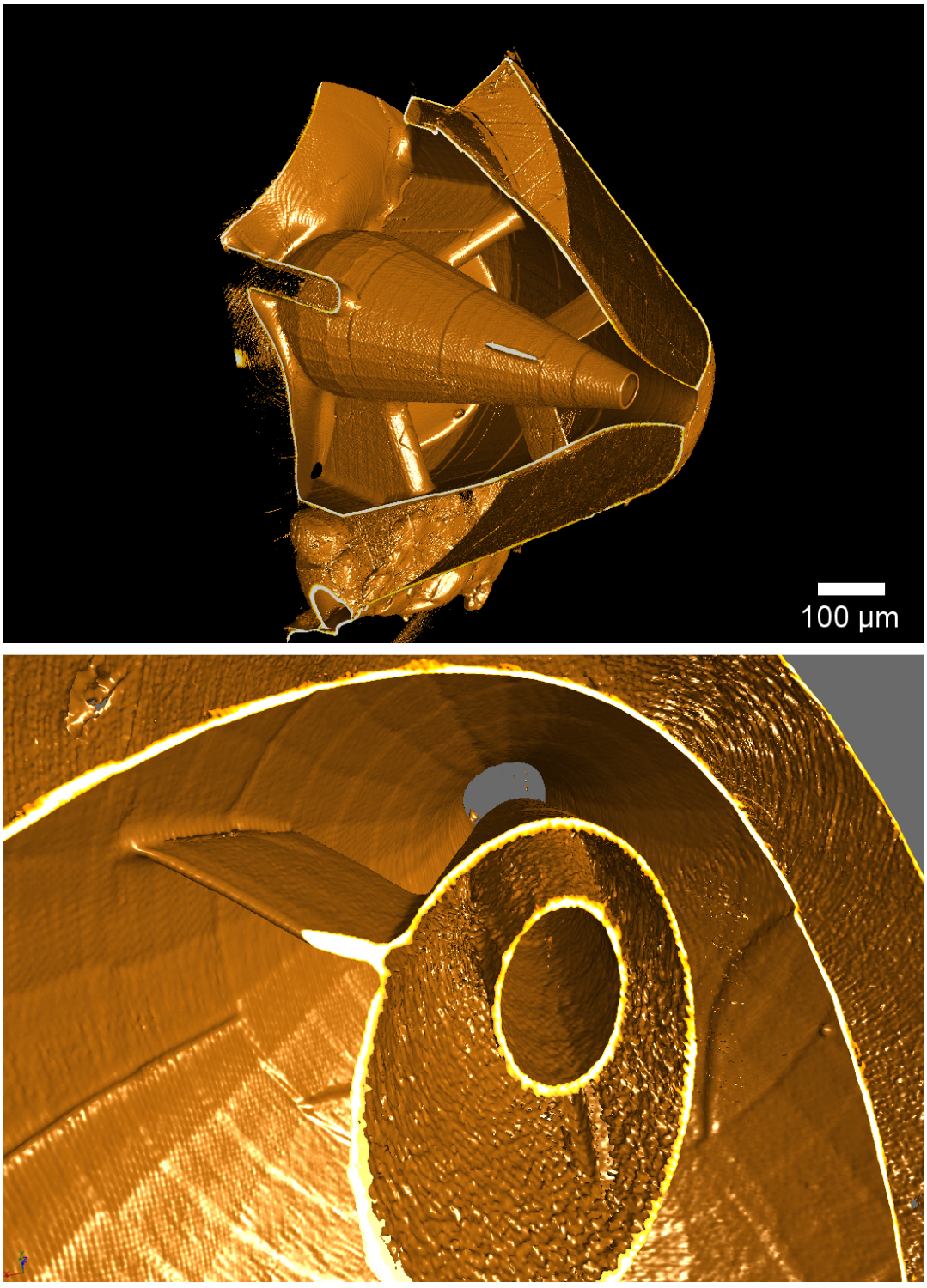

Figure 37: (Above) X-ray tomogram of prototype 2 nozzle showing the polygon-like surface structure. (Below) View showing the absence of the residue seen in Figure 32, which was accomplished by using an improved development procedure. The appearance of hollow sections that are normally solid is an effect of the data rendering: they are not physically hollow.

Figure 38: Improved prototype 2 nozzle with a straight jetting profile. No variation in angle was observed when rotating the nozzle.

3.5 Discussion and Conclusions

The obstructions seen in Figure 32 are likely responsible for the slight off-axis jetting. However, if true, then it should also be true that the deposition of unwanted photoresist is somehow reproducible, since reproducible jetting behavior was observed. These obstructions were removed with an improved development procedure. The unusually low helium gas pressures necessary for jetting may result from increased flow speed through the constriction formed by the extra material – an interesting result that may influence future designs. This effect disappeared after the residue was removed.

Index-matching and X-ray tomography proved to be an effective means for imaging interior nozzle structures. Index-matching was easy to implement and revealed the original sidewall profile beneath the suspected depositions. X-ray tomography afforded the ability to view any part of the nozzle directly in high detail. The X-ray tomography was completely non-invasive, whereas nozzles imaged in Glycerol were difficult to clean for future use. Imaging provided guidance for fabrication that lead to improved nozzle performance (straight jetting).

In actual SFX sample delivery the slight off axis jetting did not impair data collection; this is not surprising as this kind of angular deviation is not uncommon with the glass-style GDVNs used at the LCLS. It was confirmed that the photoresist material itself did not adversely affect the protein crystal diffraction for the samples used. In most respects, the prototype 2 printed nozzle performance prior to the improved development procedure was no different than the

performance of hand-ground glass GDVNs, while benefitting from the noticeable improvement in reproducibility and lower-than-normal helium gas pressure (about 6 times lower). The improved nozzles allow for reproducible straight jetting.

The successful acquisition of SFX diffraction implies that 2PP 3D printed nozzles can be a suitable alternative to conventional GDVN nozzles. Producing and testing a new design is straightforward and does not require new tooling, which in the case of injection molding may require several weeks to prepare. Hence, the 2PP 3D printing should be very useful in complementing computer simulations of nozzle jetting to iteratively optimize a new nozzle design quickly.

A particularly intriguing feature of the 2PP 3D printing process is the ability to fabricate nested structures, which are difficult or even impossible to achieve in conventional glass capillary, injection mold, or soft lithography based GDVN nozzles. This ability to overcome geometry constraints imposed by traditional fabrication processes will facilitate the development of new types of injectors such as for solution scattering, single-particle imaging, mixing nozzles, flow focusing and pulsed jets.

Further work on the nozzle design and printing conditions may facilitate improved printing speed. Additional work includes eliminating the need for the micromanipulator-assisted assembly. This may be achieved by directly printing complete nozzles that can interface seamlessly with a standardized manifold for sample injection.

4. VISCOUS INJECTOR DEVELOPMENT

4.1 Overview

The "LCP injector" immerged in large part due to a need to perform serial femtosecond crystallography with crystals made from G-protein Coupled Receptors (GPCRs) that were grown in a viscous medium called Lipidic Cubic Phase (LCP). The principles underlying the injector's development and operation are reported in detail by colleagues in recently published dissertations: Wang, 2014; especially James, 2015, and therefore they are not repeated here. The author participated in the first and subsequent applications of the injector for in-vacuum LCP extrusion for SFX studies at XFEL facilities (Liu et al., 2013; Weierstall et al., 2014; Zhang et al., 2015), and, along with others, developed methods for atmospheric LCP extrusion for serial millisecond crystallography at synchrotrons (Nogly et al., 2015). Furthermore, the author assisted in the development of Agarose as an alternative viscous sample carrier for in-vacuum operations (Conrad et al., 2015; Lawrence et al., 2015). The results of these studies are summarized in Appendix A. This chapter reports the author's development of efficient extrusion methods for helium-enriched atmospheric data collection when using full beam transmission from the LCLS at 10Hz repetition of ~45-femtosecond pulses, as well as the development of an alternative viscous media that shows promise as a crystal-carrying carrying medium for both vacuum and atmospheric operation: high molecular weight Polyethylene Glycol (PEG), also referred to as Polyethylene Oxide (PEO). PEO extrusions were successfully used for data collection in atmospheric conditions at both XFEL and synchrotron facilities. Several promising in-lab tests were performed for

sample delivery using PEO under vacuum conditions, a method to be tested at light source facilities in the very near future.

4.2 Methods for In-Air Collection with High Transmission LCLS Beam

Currently there are certain circumstances in which there may be interest in XFEL serial data collection in either ambient atmosphere or a helium environment. While vacuum operation results in lower background and is also more favorable for single-particle work, an atmospheric environment extends what can be done in the way of sample delivery. One example of this is the switching device from chapter 2, in which the switching relies on there being no vacuum (i.e. the Coandă effect). Furthermore, even if the switching could somehow be done, the sample to be recycled likely would not survive the vacuum environment. Another example is fixed-target collection, in which a non-vacuum environment is essential to the prevention of freezing.

Helium environment operation is offered at the SPring-8 Angstrom Compact Free Electron Laser (SACLA) XFEL facility in as well as at the LCLS. This section reports on the use of viscous delivery methods in a helium-enriched atmospheric environment in the CXI hutch at the LCLS, in which the use of a Rayonics detector allowed for data collection using up to 100% transmission – a mode of operation that is currently rarely used with the CSPAD detector due to the possibility of severe damage – but with only 10Hz readout rate. The LCLS beam was accordingly delivered at 10Hz pulse repetition. Because this data was collected recently, specific details about samples are not reported. This study focuses rather on the extrusion characteristics under high X-ray transmission

and how the high transmission itself can be used to efficiently collect data from poorly extruding sample mediums.

4.2.1 Low Transmission Characteristics

LCP extrusions are only mildly perturbed when using low transmission of the X-ray beam at the LCLS (transmissions of <1% up to about 20%). Figure 39 shows an example of how a 50-μm, sample-carrying LCP stream appears without the X-ray and with the X-ray at 13% transmission and a pulse repetition rate of 120 Hz as collected inside of the microfocus vacuum chamber at CXI. The X-ray interaction point is 100 to 150 μm downstream of the capillary tip (Figure 39B). In this case the sample stream is clearly affected downstream of the point of X-ray interaction. The material that has collected on the capillary tip can be a result of gradual accumulation of flying debris

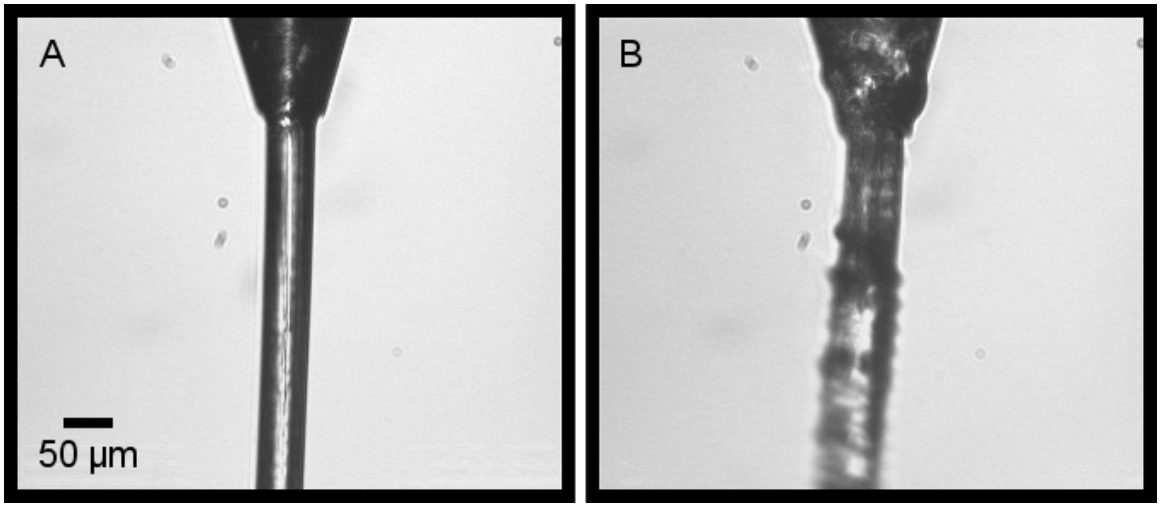

Figure 39: The effect of the X-ray beam on the extruded LCP is quite noticeable in this example of 13% beam transmission in the CXI vacuum chamber at the LCLS: A) the LCP flowing without X-ray interaction; B) with X-ray interaction. Note in B) that sample may collect on the tip of the capillary over time.

and/or sample that is deposited when the jetting is temporarily halted. Often it is the case that the sample medium upstream of this interaction point appears unaffected, with the downstream portion having clearly been affected by beam interaction. However in this special case, the sample stream appeared to form an immobile shell around the moving sample stream upstream of the interaction point, which detached itself from time to time. This effect is present in certain samples and may be attributed to dehydration from helium gas, although the effect appears much more pronounced when the X-rays are turned on. This represents a typical data collection situation at low transmission.

4.2.2 High Transmission Characteristics

Figure 40 shows a frame-by-frame sequence taken from high speed video of an LCP sample stream being hit by a single X-ray pulse when operating at 54% transmission. At 54% transmission, the displacing effect of the energy imparted by the X-ray is much more pronounced. At 13 μs a mixed exposure is seen that shows what appears to be a cloudy ball of debris that extends about 100 μm along the stream. At 26 μs this same section has become thinned, the exact cause of which is unclear. From this point forward in the sequence of frames, it is presumably (but not necessarily) the case that the high speed co-flowing helium gas that functions to steer the extrusion has taken hold of the piece and has started to pull the stream apart. That this latter separation is driven primarily by gas forces and not the energy imparted to the stream by the X-ray beam is suggested by the asymmetry of the separation from the point of interaction: everything upstream of the interaction point after 26 μs remains in place, while everything

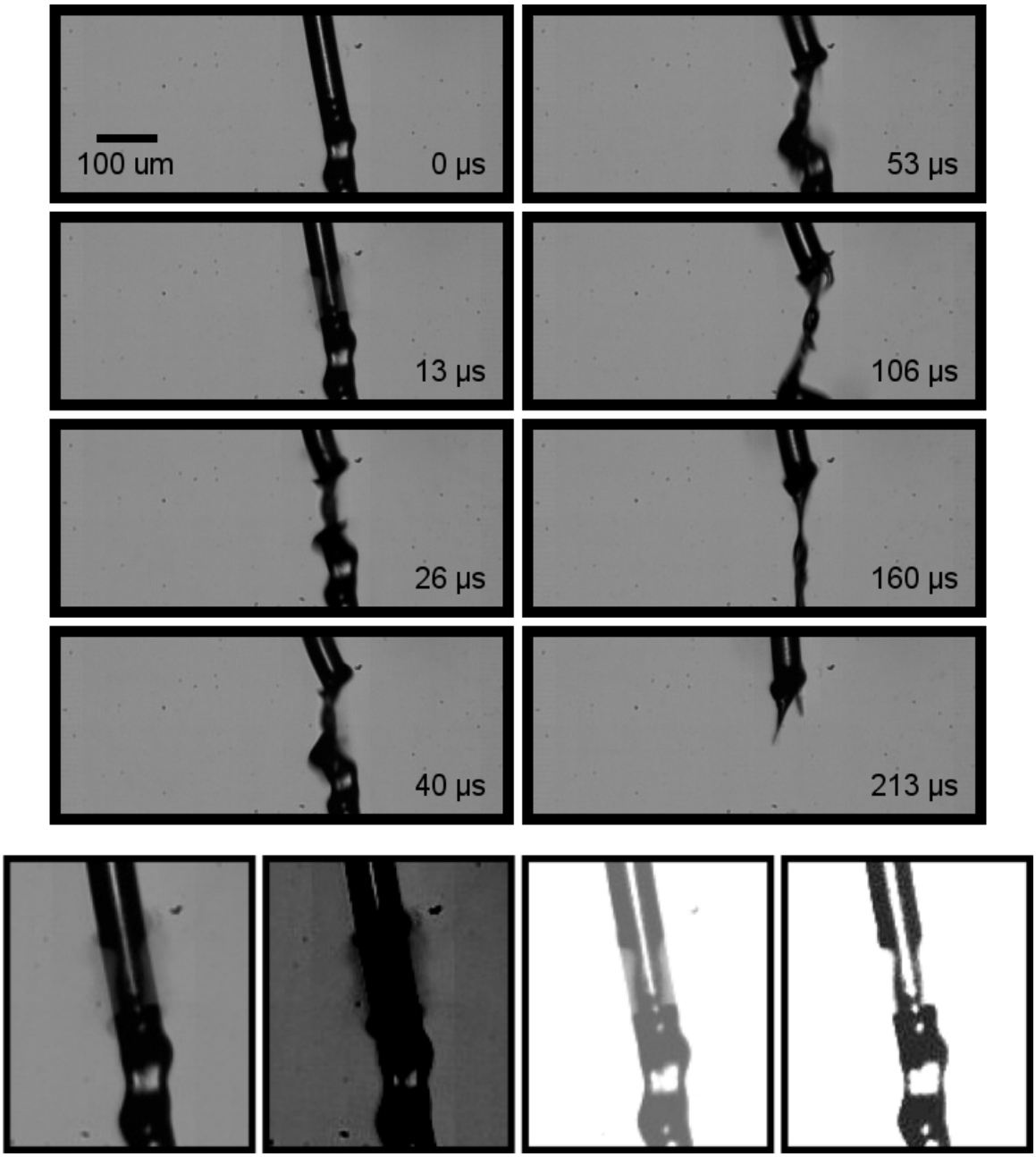

Figure 40: (Above) Frame-by-frame sequence taken from high speed video (75,000 fps) of an LCP sample stream being hit by a single X-ray pulse when operating at 54% transmission. X-rays are coming in from the right. (Below) Post-processed variations in brightness and contrast reveal discrete LCP stream orientations superimposed upon themselves within the single image, suggesting informative activity on a finer timescale. From left to right are the original image, one variation emphasizing what appears to be blast debris, another variation showing the faint exposure of the unaffected stream overlapping with the affected stream, and the affected stream seen alone at higher brightness and contrast. The upper bound on the blast radius in this example appears to be about 50 µm, assuming that the separation following the frame at 26 µs is driven by helium gas forces.

downstream of this point moves down. The frame taken at 26 μs represent at least an upper bound on the blast radius (~50 μm), with the possibility of it being significantly smaller if the gas forces have already appreciably taken effect. In fact, a closer look at the frame taken at 13 μs suggest that it may contain as many as three distinct event, all captured during the relatively "long exposure" of that frame. This is shown at the bottom of Figure 40 where different brightness/contrast settings more clearly distinguish what are at least two distinct states of the stream, seen as the overlapping of images contained in that frame. For clarity it should be stated that adjusting the bright/contrast settings did not result in a continuous change of appearance of the image, but rather in the pronunciation of completely distinct images.

Figure 41 shows a similar situation but at 100% transmission. This example is noticeably more destructive and appears to show an upper limit on the blast radius of about 75 μm, provided the assumption is true that the helium gas begins or has already began to separate the stream within 26 to 40 μs after the blast occurs. The stream takes about 580 μs to recover from the blast and it's mechanical effects. Even if operating at 120 Hz (about 8.33 milliseconds between pulses) there appears to be plenty of time for the stream to recover. It is worth noting, however, that the dampening of the pendulum-like motion described in Figure 41 likely depends on the gas dynamics, which can vary substantially from nozzle to nozzle.

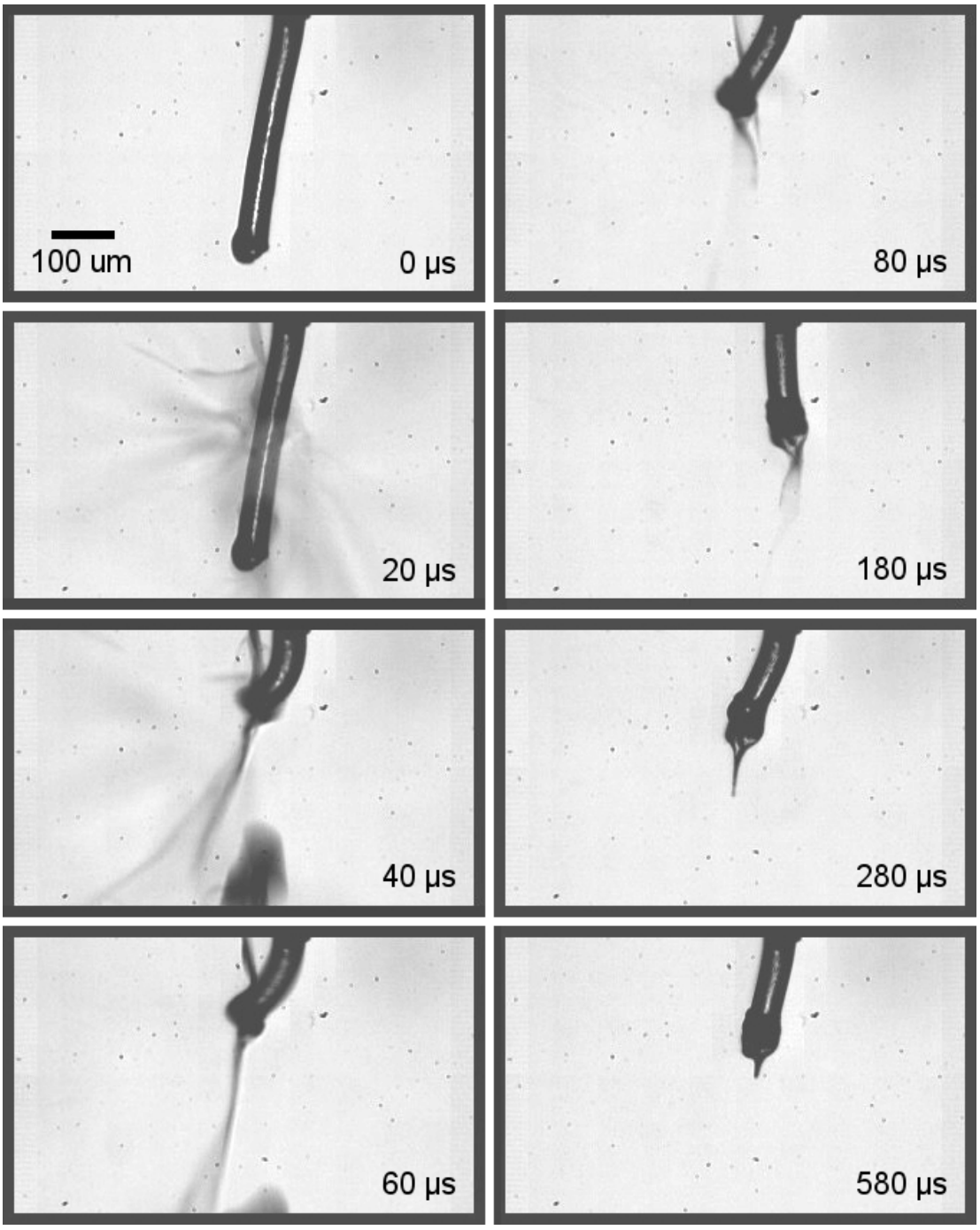

Figure 41: Similar layout to Figure 40, but at 100% X-ray transmission and taken from high speed video footage taken at 50,000 fps. X-rays are coming in from the right. The frames that follow the frame at 80 µs are given at larger time intervals and show the stationary points of a pendulum-like response after the separation of the stream and which began to dampen significantly after the frame at 280 µs, stopping at 580 µs. In this example the upper bound on the blast radius is about 75 µm, and, like in Figure 40, the actual blast radius is not clear due to limitations in time resolution.

4.2.3 Special Methods for Poorly Extruding Samples

It is sometimes the case that a certain LCP sample does not jet well. It is thought that this is most often due to the properties of the specific sample contained within the LCP medium: concentration of crystals, size and shape of individual crystals, other crystal properties, and buffers. The author is aware of no studies giving thorough evidence how these factors contribute to poor extrusion in viscous sample delivery, perhaps because the effects are very difficult to sort out. It has been observed that problems arise in both viscous and non-viscous delivery when crystals are either too large or too concentrated. Since the GDVN jet is substantially reduced in diameter, crystals can easily approach and exceed the stream size, leading to stream instability. An extrusion is different in that the extruded viscous stream is not reduced in size by the co-flowing gas. Crystals that approach the size of the extruded stream do not appear to significantly affect stream stability, while crystals that exceed the size of the extruded stream will, of course, simply clog the capillary. It is the author's observation that any additives involved, such as buffers, have the capacity to negatively affect the extrusion quality of the viscous medium. As might be expected, there is a correlation between decreasing the viscosity of the medium through buffer dilution and decreasing the extrusion quality, the result being more of a growing sphere than a linear extrusion.

Another unfavorable type of behavior in viscous injection is an extrusion that quickly goes off-axis with a tendency to fly back upon the capillary tip. The author attributes this behavior to effects of gas flow, but there is also the possibility that charging plays a role. The exact cause has not been addressed because the typical practice for dealing with this behavior is to increase the helium gas pressure, which has

the effect of cutting off the LCP extrusion to within a few hundred microns from the capillary tip. This practice is more often needed with atmospheric operations. Occasionally a given sample almost instantly curls back toward the tip, which is a situation that is not favorable during data collection at lower transmissions (from about <1% to 20%) since the growth on the tip simply grows larger. Increasing the gas pressure even further in such cases allows just a small portion of the emerging medium to be visible.

During the in-air/helium data collection at the LCLS discussed previously, the fact that the high transmission mode completely removes a portion of the extrusion was used advantageously in cases where extrusion is poor as described above. When operating at higher transmission and with a distance of from 100 to 200 μm from the nozzle tip to the X-ray interaction point, the growth formed by poor extrusions is occasionally blasted away by the X-ray beam when the "blob" on the end of the capillary tip grows sufficiently large to cross into the X-ray beam. However, by moving the capillary tip to within 25 μm from the X-ray interaction region, a more efficient means of collection is achieved. The sample-carrying medium forms a hemispherical meniscus that extends to at least 25 μm from the tip of the capillary when using a 50-μm inner diameter capillary, and adjusting the flow rate allows the X-ray to completely remove this section of the sample with each pulse. Hit rates of between 40% and 60% were achieved in the mode of operation. Figures 42 and 43 show the time interval between hits as recorded at 60 fps and 10,000 fps, respectively. In both cases the time interval between shots was 0.1 seconds, corresponding to the 10 Hz pulse frequency being used.

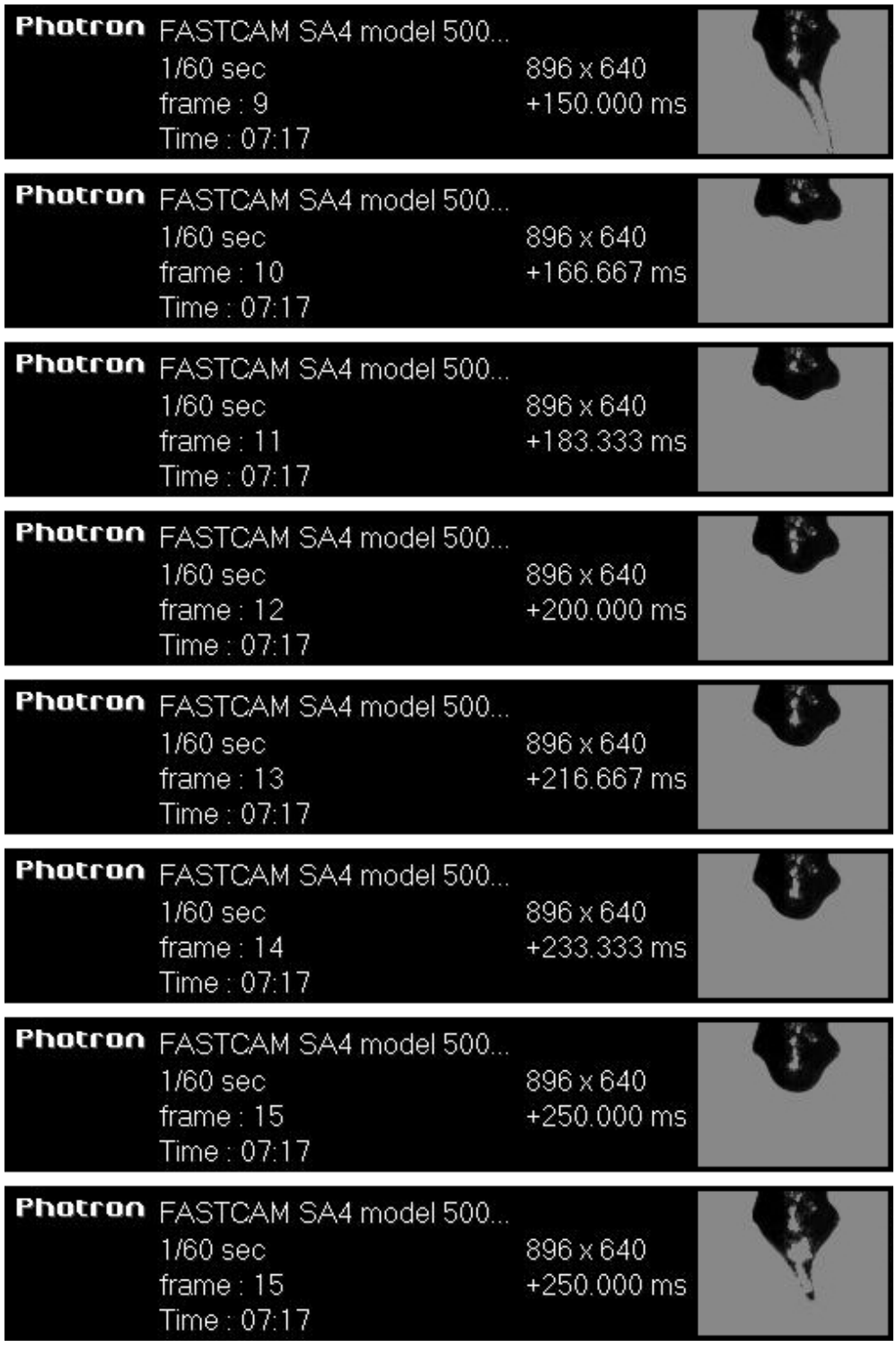

Figure 42: Sample in LCP. The X-ray is probing the stream about 25 µm from the tip of the 50-µm inner diameter capillary. The above sequence shows two hits (uppermost and lowermost frame) separated by 100 ms, corresponding to the 10 Hz LCLS pulse repetition rate that was being used.

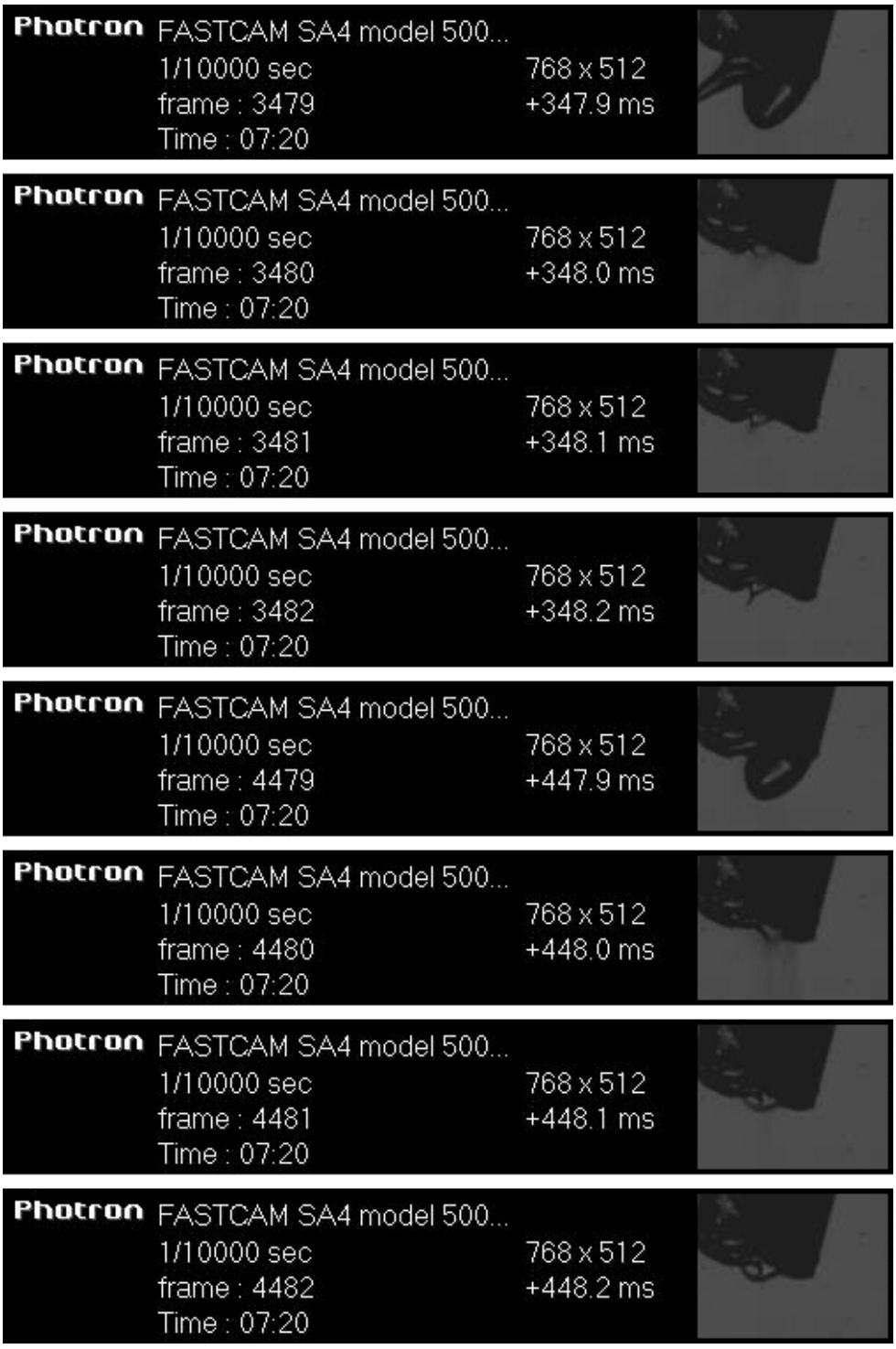

Figure 43: Another sample in LCP. The X-ray is probing the stream about 25 µm from the tip of the 50-µm inner diameter capillary. The above sequence shows two hits (second from top and sixth from top) separated by 100 ms, corresponding to the 10 Hz LCLS pulse repetition rate that was being used. Occasionally, excess debris from the hits would collect on the side of the capillary as seen in this series of images. However, this did not appear to cause a problem with data collection.

Obviously the primary concern with this method was the effect of the blast on the quality of data. A comparison of data collected using this method to data collected on the same sample using the usual method (a few hundred microns from the tip) would be a helpful way to further verify the method. Nevertheless, crystals were diffracting. These results support the idea that the actual damage-inflicting blast radius from the X-ray in the ambient air/helium environment is no larger than 50 μm, even at 100% transmission.

The situation of having the X-ray hit so near to the capillary tip is a special case in which physical displacement of the sample-carrying medium upstream of the interaction point is eliminated, since that portion of the stream is contained within the glass capillary. Assuming, based on the quality of data collected, that the physical displacement along the stream axis (as in the frame at 26 μs in Figure 40 and at 40 μs in Figure 41) is large relative to the actual damage region that propagates beyond the X-ray beam intersection, this mode of operation may provides a way to utilize sample-containing mediums that do not extrude at all, but only when operating at high transmission; lower transmission operation would not remove the excess material that would collect at the tip over time and result in higher background and possibly multiple crystal hits and data from damaged crystals.

This mode of operation may also be useful for samples that already extrude well. As seen in Figure 41, there is a significant displacement of the stream perpendicular to the stream axis in response to the explosion – pendulum-like movement that can takes as long as about 580 μs to dampen. However, as discussed earlier, this is well within the time between pulses, even at 120 Hz. But it is possible that other effects might arise

when operating at 120 Hz. High speed video of the extrusion's response to X-ray interaction under such conditions would be informative.

4.3 Extrusions using High Molecular Weight Polyethylene Glycol

4.3.1 Overview

The discovery of high molecular weight PEG as a viscous medium occurred while testing supercoiled DNA samples in PEG 8 x 10^6 (for simplicity the units g/mol are omitted when naming the PEG in this manner) for use in correlation studies. Mixtures of DNA in buffer mixed with PEG 8 x 10^6 extruded successfully in laboratory tests and during correlation studies carried out in a helium environment at the SACLA XFEL facility in Japan. In terms of extrusion, the PEG performed very well during this experiment. Actual experimental results appeared promising when the data was being collected, but have not yet been fully analyzed.

Out of interest in using the high molecular weight PEG as a crystal-carrying medium, several laboratory tests were subsequently conducted using PEGs of varying molecular weight and concentration. Initially PEGs without any crystal sample were tested in both vacuum and atmospheric condition using molecular weights of 1 x 10^5, 1 x 10^6, and 8 x 10^6 g/mol mixed with water in concentrations ranging from 7% to 18%. The results from these first tests provided the choice of PEG weight and concentration for testing a selection of protein crystals for both survival in the high molecular weight PEG and for extrusion quality. SONICC and birefringence imaging techniques were used to check the survivability of the crystals in the PEG medium. As part of a preparation for a synchrotron beamtime at PETRA-III at DESY, the extrusion tests of PEG samples

carrying crystals were conducted in atmospheric conditions. Samples diffracted successfully during the said beamtime.

4.3.2 Initial Testing and Performance at SACLA

Figure 44 shows selected frames from a video in which the viscous PEG was first confirmed as a potential candidate for sample delivery. This sample was composed of an undisclosed amount of 5.4 mg/mL DNA/Tris base mixed with an 11% concentration of PEG 8 x 10^6. At first, the sample appeared basically hopeless, collecting upon itself in what appeared to be a sticky mess. In this initial test, the tip was cleaned with water from a spray bottle, after which it continued to collect upon itself. But after the tip was sprayed with water the second time, a stable extrusion formed. As can be seen in Figure 44F, the stream is thinned, an effect that resembles the thinning seen in the non-viscous GDVN. However, instead of breaking up into a stream of droplets, the stream continued for meters. Figure 44G shows a macroscopic view of the extrusion. In this specific test the stream continued for about 2.5 meters across the laboratory, held stable by co-flowing helium gas on a course parallel to the ground until forces from ambient air currents began to dominate those from the helium gas. In exploring what flow rates were possible, it was noticed that the DNA-carrying PEG medium was capable of extruding at the lowest flow setting on the HPLC pump: 0.0001 mL/min, which corresponds to an actual flow rate of about 3 nL/min when using a viscous injector with a 34x mechanical advantage (Figure 45). No thinning was observed at this flow rate, and drying of the stream appeared to be occurring. Ramping back up to high flow rate was easily achieved.

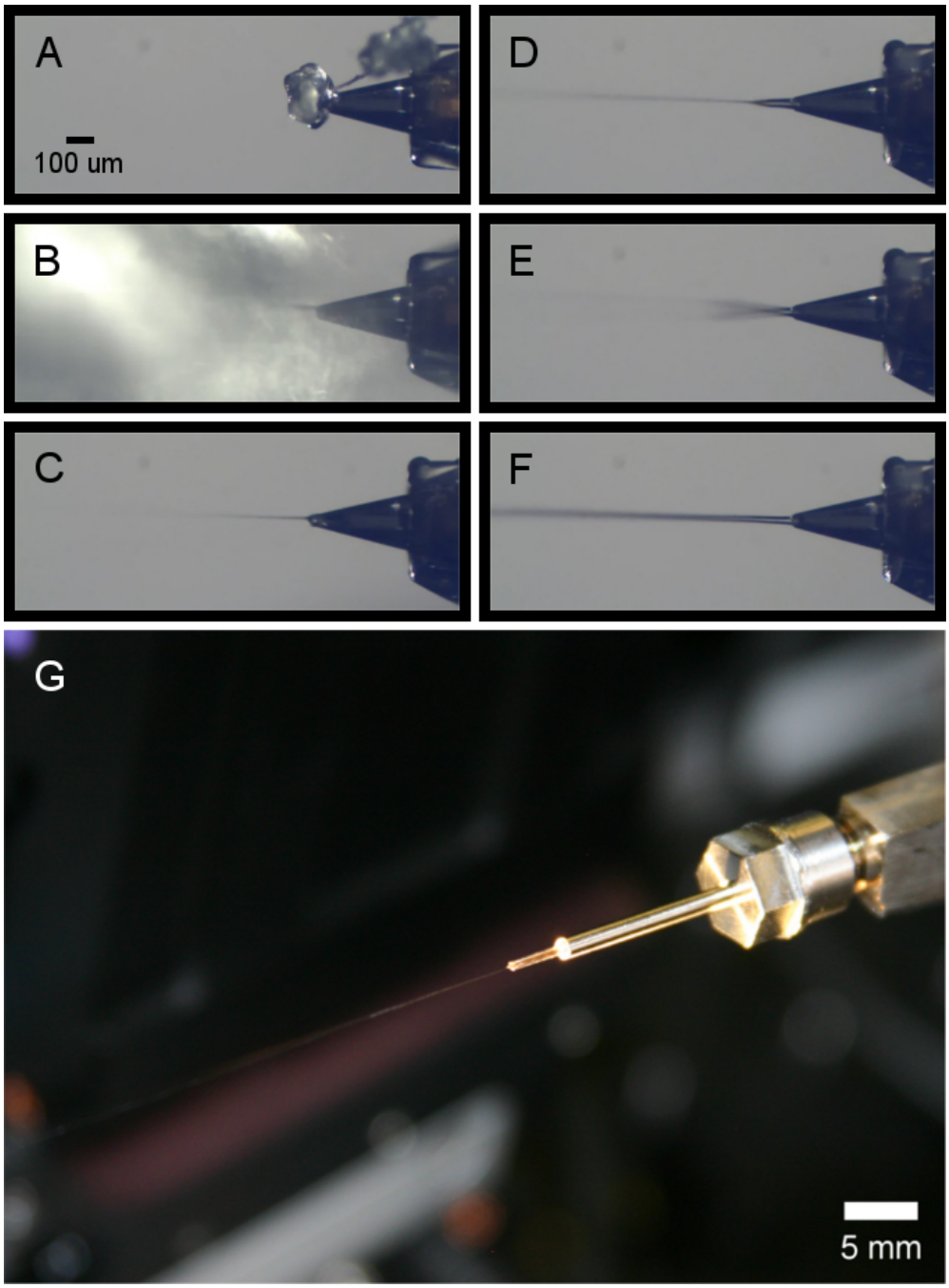

Figure 44: Footage from the first high molecular weight PEG tests, in which a solution of DNA particles mixed into PEG 8 x 10^6 was tested for operation in atmospheric conditions. PEG concentration was about 11%. A) The jet tended to flow into a mass of varying dimensions near the tip until B) being sprayed with water. C) This appeared to clear out everything except a very thin stream, presumably elongated by the co-flowing helium gas. D) From this emerged a stream matching the inner diameter of the capillary, which E) experienced flickering until F) reaching a certain length at which the stream became stable and slightly thinner than the inner diameter of the capillary. Purposefully interrupting the stream resulted in the condition of (A) and the process (B) was repeated with the same results (C) through (F). G) This stream continued unbroken for meters (just a few centimeters are shown in the figure).

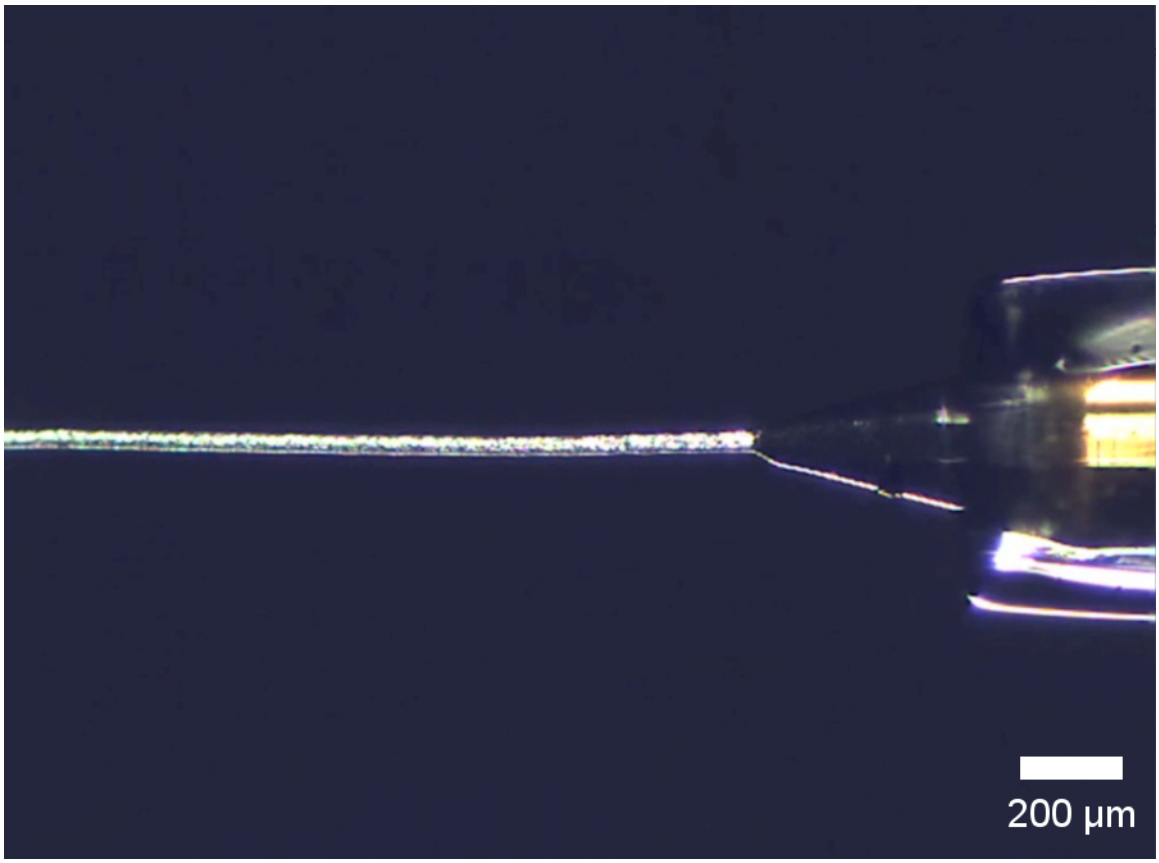

Figure 45: The same sample shown in Figure 44 running at the lowest flow rate setting on an HPLC pump: 0.0001 mL/min, which is an actual flow rate of about 3 nL/min since the injector makes use of a plunger with a 34x mechanical advantage. The low linear speed of the stream appeared to result in dehydration from the co-flowing helium gas, which in turn produced a constant diameter flow profile. Reducing flow to this rate while maintaining stability required a corresponding decrease in gas pressure. It was straightforward to ramp the flow rate back up to the 0.005 mL/min setting, which is an actual flow rate of about 150 nL/min and fine tune the gas setting again.

Clearly, however, the fact that the extrusion began only after the tip was sprayed with water presented a problem. Also, if the stream was purposefully interrupted, for example, by pulling the extrusion away by hand, an additional spray on the tip was necessary to restart the stream. This is, in general, undesirable for serial data collection from light sources. Sample media that experience regular interruptions in flow that are not fixable from outside of the experimental hutch are detrimental due to the time required to enter the hutch and restart the sample. While it was clear during these first

tests that, when not intentionally interrupted, the DNA-carrying PEG medium ran very stably, the one major component not present during these laboratory tests was the probing light source, which, and especially when using XFEL sources, can significantly disturb the stream. These samples were being characterized for use at the SACLA XFEL facility. It was found during operation at SACLA that the XFEL beam did, in fact, disturb the PEG jet, but did not actually cause a significant problem. The 40Hz X-ray pulses at 100% transmission caused the stream to expand. Interruptions in the medium flow, when experienced, were likely due to sample/medium heterogeneity. Thoroughly mixing the samples reduced the occurrence of flow interruptions almost completely.

Operation at SACLA included a few additional parameters that were not used in the prior laboratory tests. One of these was the presence of a vacuum catcher, which functioned to collect the sample but also to stabilize the extrusion. Another factor was the use of hydrated helium gas, which was intended to prevent charging effects during extrusion (Figure 46). It was noticed that restarting the PEG extrusion was easier while working in the experimental hutch, as opposed to in the laboratory. The capillary tip only needed to be wiped with a wetted cloth once before extrusion began. Another factor that may have contributed was the use of a viscous injector that was built at SACLA. This injector possessed the same basic components of the ASU injector but with dimensions and materials that were quite different. The extent to which these additional factors contributed to the ease of extrusion is difficult to ascertain without additional testing.

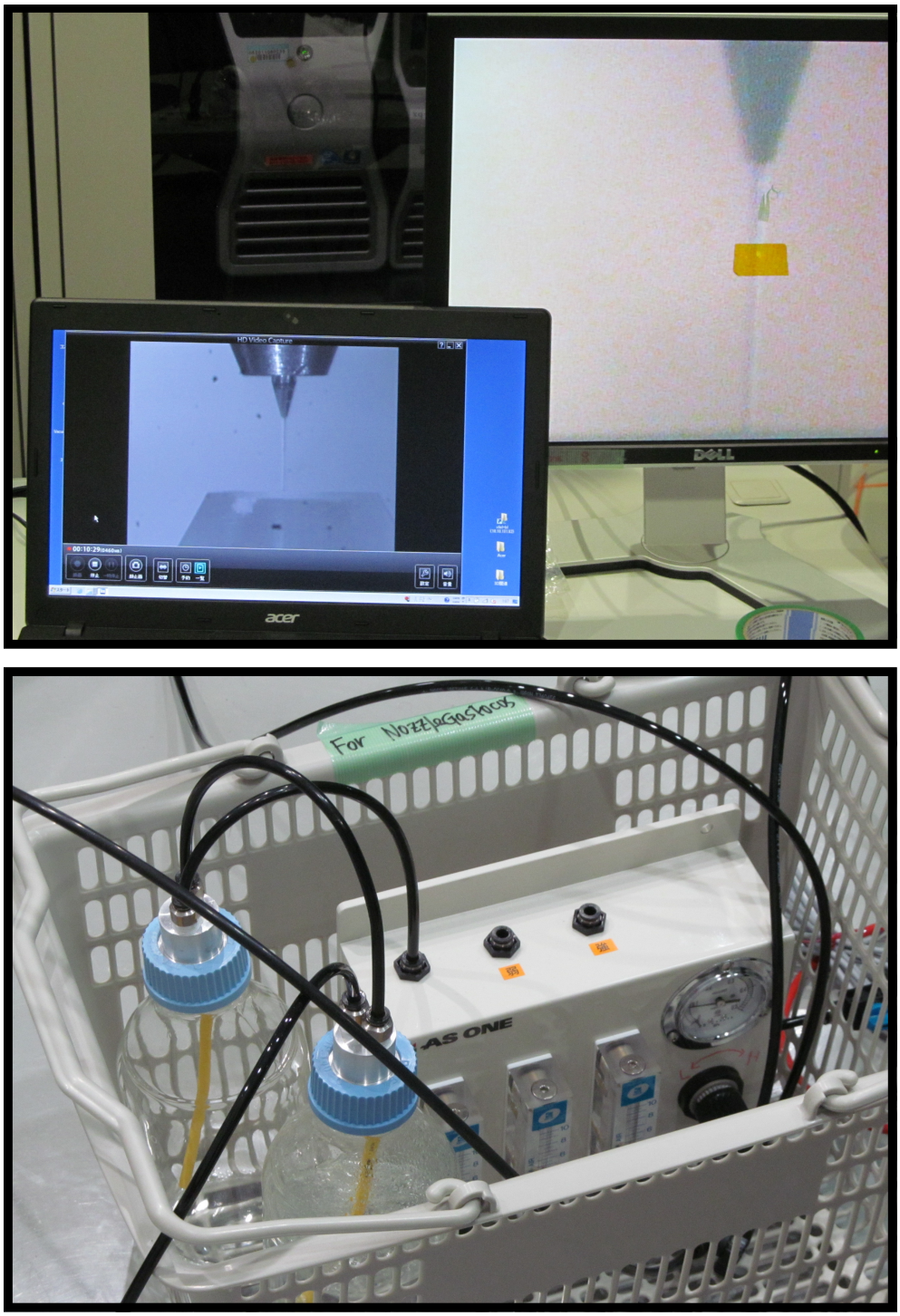

Figure 46: (Above) Monitors displaying the PEG jet used at a SACLA beamtime. The in-house viscous delivery system was used, which, along with the injector, includes a vacuum catcher, which is visible in the laptop computer monitor as a tube with a larger bevel collecting the sample, and (Below) a helium hydration system. The nozzle was housed in a large plastic helium-filled chamber with the vacuum catcher system recycling the helium gas back into the chamber.

4.3.3 PEG in Water Testing for Use as a Crystal Carrier

The successful operation of the PEG extrusion at SACLA prompted further investigation of high molecular weight PEG as a crystal-carrying medium. High molecular weight PEG comes supplied in solid form as Polyethylene Oxide (PEO). PEO is extensively used in industrial applications, and therefore is well studied. A thorough rheological study of PEO aqueous solutions of molecular weights of 1×10^5, 4×10^5, 1×10^6, and 4×10^6 g/mol at concentrations ranging from 0.1% to 10% revealed that 1×10^5 PEO was the only solution that behaved as a Newtonian fluid (Ebagninin et al., 2009). This finding correlates with what was determined in the initial stage of the testing of PEO as a general sample carrier in preparation for crystal tests. PEO/water solutions with average molecular weights of 1×10^5, 1×10^6 and 8×10^6 at concentrations ranging from 7% to 19% were tested for extrusion in order to arrive at some limits on what kind of PEG weights and concentrations can be extruded. These tests were performed in both atmospheric and vacuum conditions. The results correlate to the results in the above-mentioned study, suggesting the possible requirement (or, at least, advantage) of non-Newtonian flow characteristics in viscous injection. Only a superficial extrusion was achieved with PEG 1×10^5, whereas PEG 1×10^6 and PEG 8×10^6 both extruded in the same manner as shown in the SACLA preparation testing.

The PEG 1×10^5 superficial extrusion was achieved with the 11% concentration in vacuum with a 50-µm inner diameter capillary and with the 19 % concentration in both atmosphere and vacuum using a 20-µm inner diameter capillary (Figure 47). This superficial extrusion behavior is different from the typical extrusion behavior primarily in the way the medium attached to the nozzle tip, and it appears to depend somewhat on the

utility of dehydration of the PEG medium. For example, when using a 20-µm inner diameter capillary in atmosphere with the 19% concentration, the combination of the focusing and dehydrating effect of helium gas appeared to result in a plume-like growth profile that eventually linearized as the exterior hardened and growth occurred along the nozzle axis. The growth continued for a couple hundred microns before one of two things happened: (1) either the growth detached from the tip followed by a new growth or (2) an additional growth began somewhat offset and parallel to the first. This second type of occurrence resulted in as many as three additional plumes and did not appear to resolve itself by detachment. The first kind of growth, in which the plume detaches itself and begins anew, continued stably for several iterations. This mode of operation may still be useful for data collection, but would likely not be a preferred mode of operation.

PEG 1 x 10^6 and PEG 8 x 10^6 successfully extruded in vacuum conditions at 11% concentration (Figure 48). PEG 8 x 10^6 at 7 % concentration extruded successfully in vacuum conditions (Figure 49) with minor difficulty. PEG 8 x 10^6 at concentrations of 7% and 11% was also tested for operation in atmosphere (Figure 50). Theses atmospheric extrusions were successful but moderately difficulty to achieve. Theses difficulties and the means of overcoming them are described in detail later. PEG 1 x 10^6 was not tested in atmospheric conditions. The lower concentration limits for extrusion of these two higher molecular weight PEGs were not explored, although 7% concentration appeared to be a reasonable candidate for PEG 8 x 10^6.

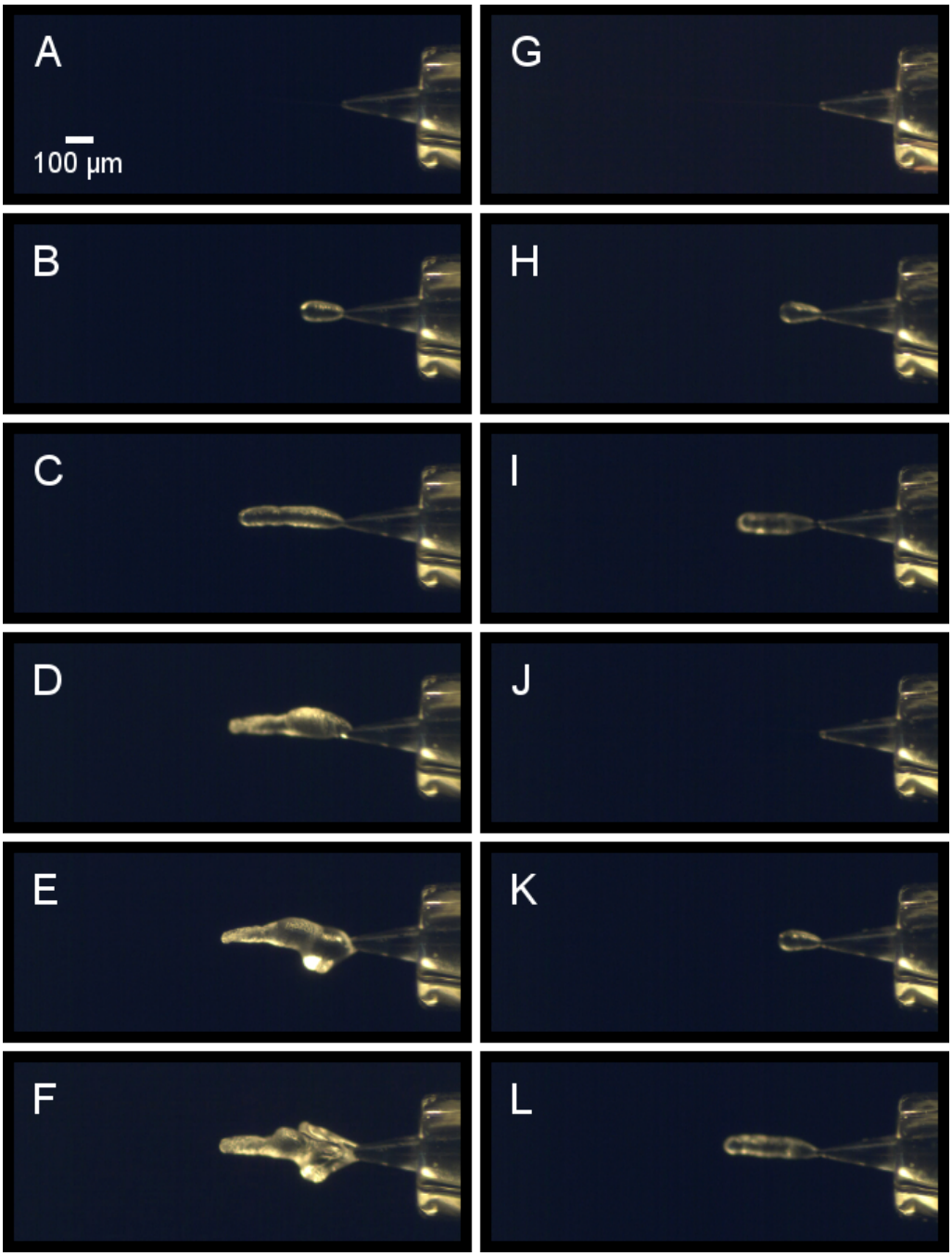

Figure 47: Two modes of a superficial extrusion of PEG 1 x 10^5 at 19% concentration in water using a 20-µm inner diameter capillary in atmospheric conditions. In one mode the plume-like extrusion extends 400 to 500 µm from the tip, (A) through (C), and stays in place while (D) another plume emerges from the tip. (E) and (F): more plumes would then emerge. In a second mode the same sequence in (A) through (C) would occur, (G) through (I), followed by a complete detachment of the first plume, and the process reoccurred: (J) through (L). These two modes occurred with the same sample, capillary, gas aperture, flow rate, and gas conditions, but each mode tended to repeat several times before switching modes.

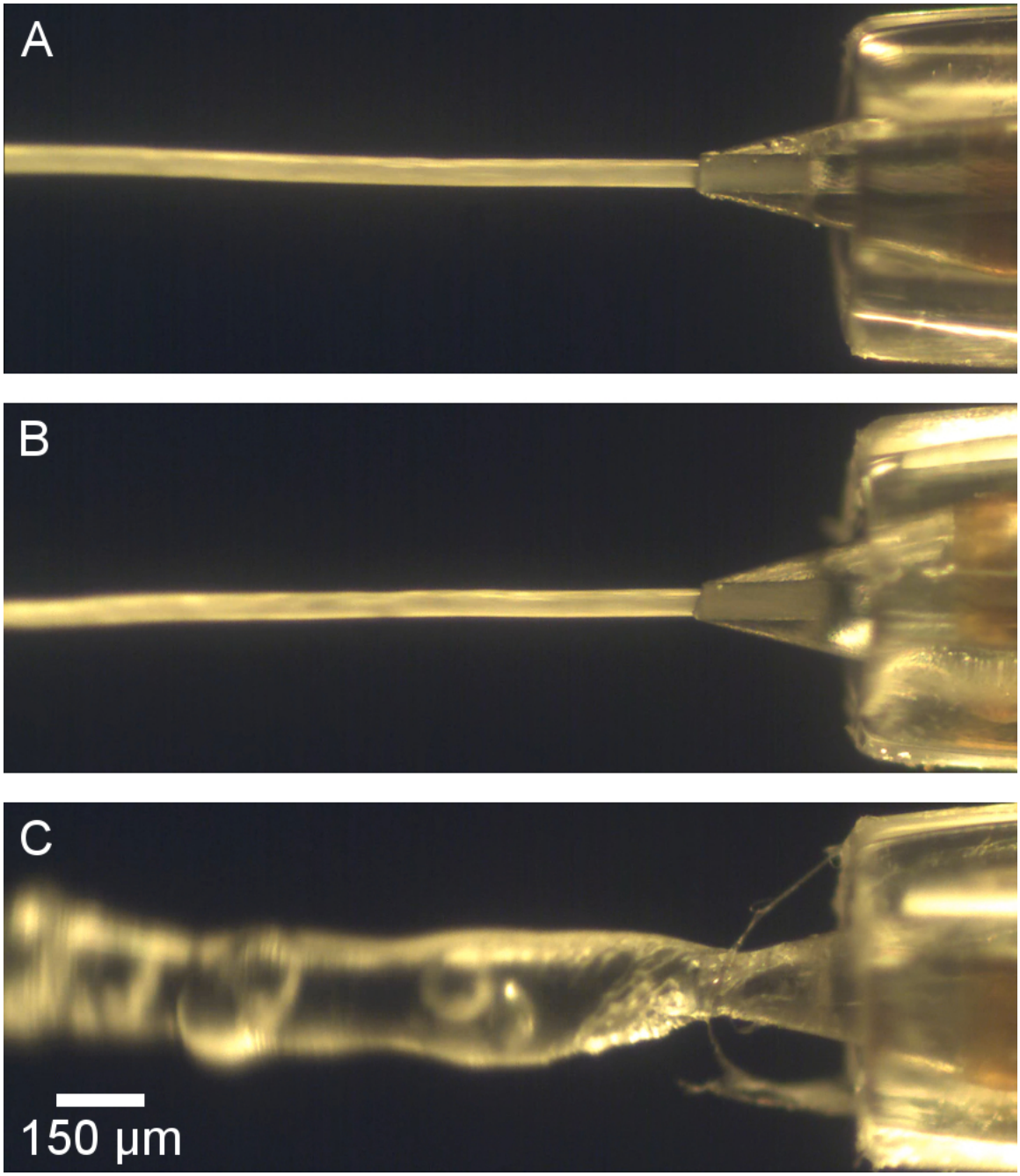

Figure 48: PEG in water solutions at 11% concentration containing no sample and extruding in vacuum with a 50-µm inner diameter capillary: A) PEG 8 x 10^6; B) PEG 1 x 10^6; C) PEG 1 x 10^5. The superficial extrusion in (C) was similar in character to the superficial extrusion from Figure 47, except that a repeated detachment mode was not observed.

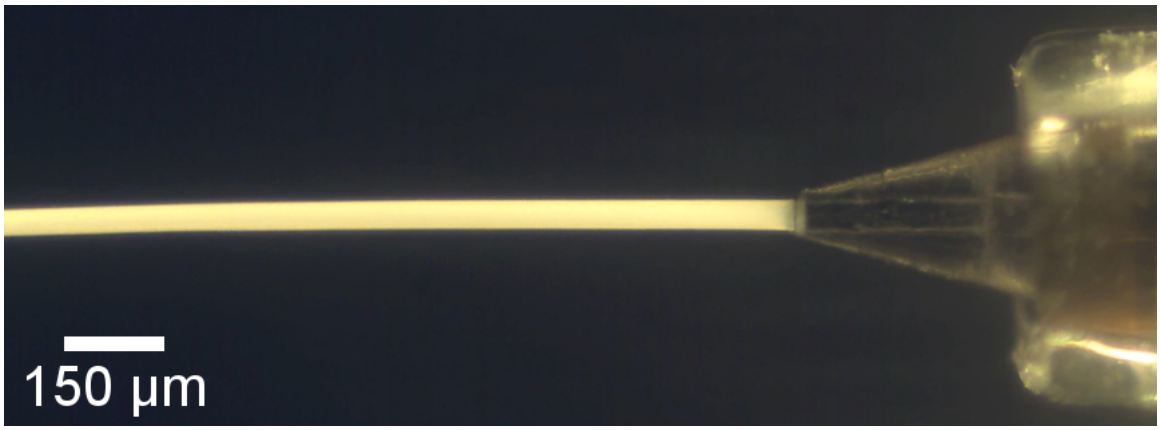

Figure 49: PEG 8 x 10^6 in water solution at 7% concentration containing no sample and extruding in vacuum with a 50-µm inner diameter capillary.

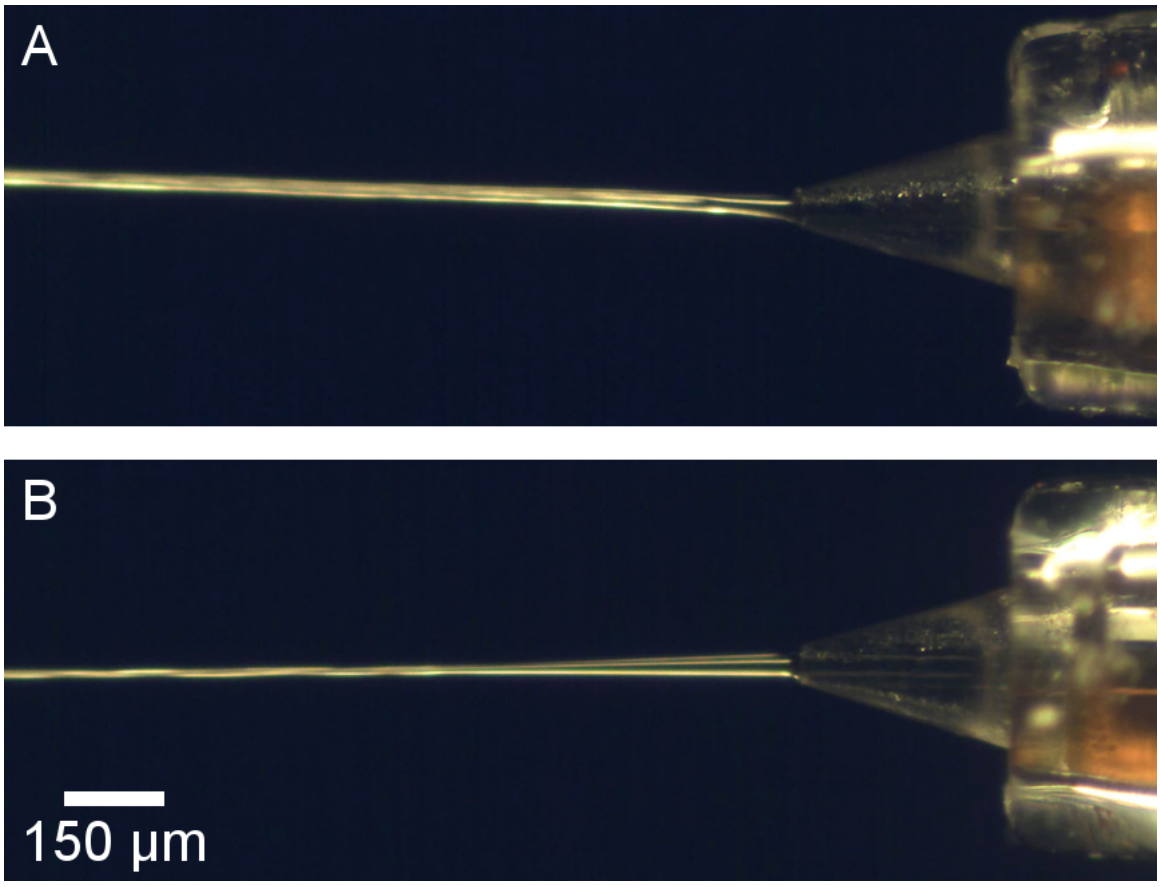

Figure 50: A) PEG 8 x 10^6 in water solution at 11% concentration containing no sample and extruding in atmosphere with a 50-µm inner diameter capillary. B) PEG 8 x 10^6 in water solution at 7% concentration containing no sample and extruding in atmosphere with a surface treated (hydrophobic coating) 50-µm inner diameter capillary.

4.3.4 PEG Extrusion Tests with Protein Crystals

Four types of crystal samples were tested with PEG 8 x 10^6 in water as a carrier in atmospheric conditions. PS-I, PS-II, Phycocyanin, and FLPP3 crystals in their native buffers were added to high concentrations of the PEG 8 x 10^6 and water solutions to achieve PEG concentrations that were near to those used in the sample-free extrusion tests. As might be expected, the extrusion behavior of these samples varied from that of the sample-free tests, when making a comparison based on PEG concentration only. The samples introduced buffers and the crystals themselves, the properties of which likely change the medium characteristics that have a bearing on flow behavior.

A batch of FLPP3 crystals ranging in size from 10 to 50 μm in their mother liquor was mixed with a PEG 8 x 10^6 in water solution for an overall PEG 8 x 10^6 concentration of 9.6%. A 75-μm capillary was used. Extrusion behavior was very similar to the 7% concentration tests with PEG only. Extrusion was accomplished only in a special circumstance shown in Figure 51. This represents an extreme case in which repeatedly spraying the PEG-sample medium with water and wiping with a wet cloth eventually forms a remarkably uneven meniscus, one side of which extends a few hundred microns inside of the capillary and the other side of which forms a thin extrusion. By slowly reducing the co-flowing helium gas pressure the stream could be brought into a more typical extrusion profile.

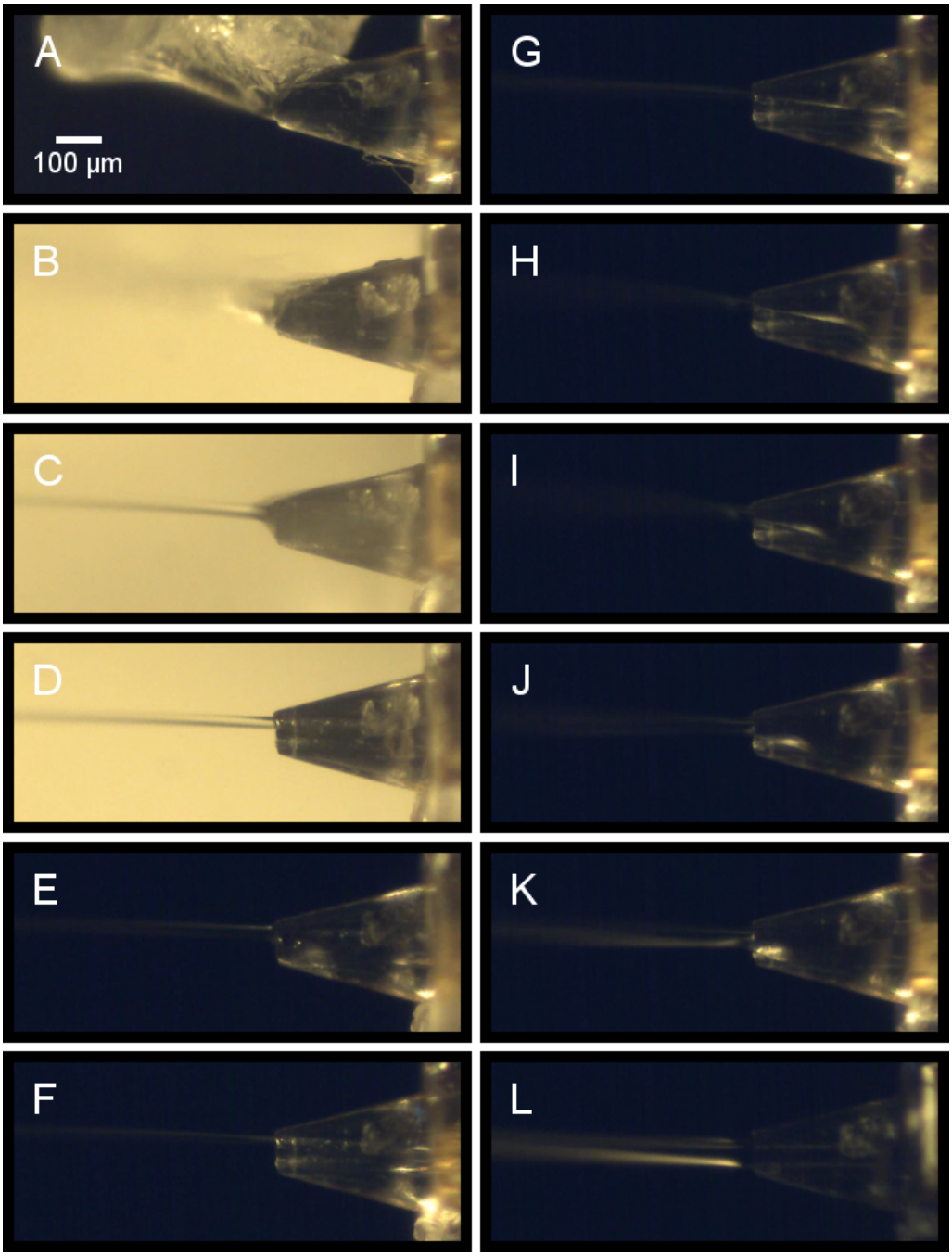

Figure 51: Extrusion of a batch of FLPP3 crystals ranging in size from 10 to 50 µm in their mother liquor mixed with a PEG 8 x 10^6 / water solution for an overall PEG 8 x 10^6 concentration of 9.6%. Extrusion behavior was very similar to the 7% concentration tests with PEG that contained no sample. This sequence of images shows the process of initiating extrusion using a wetted cloth (B through D). Of particular notice in this sequence is that the meniscus in (E) on the bottom part of the capillary extends to the right, inside of the capillary, out of the frame. By reducing the helium gas pressure gradually (F through K), the bottom part of the meniscus attachment point was brought to match with the top attachment point, and the stream was thereby brought to the match the thickness of the inner diameter of the capillary in (L).

Phycocyanin crystals were tested at a PEG 8 x 10^6 concentration of 13%. These crystals ranged in size from 2 to 30 μm, and a 50-μm capillary was used. This extrusion behaved well, as expected, with the exception of a bulbous growth that gradually formed immediately downstream of the capillary tip. Eventually the bulbous growth would fall off. When using a surface treated capillary, this bulbous growth detached more frequently (after only growing a small amount) but eventually behaved similarly to the extrusion with an untreated capillary (Figure 52). Another batch of small crystals at a more moderate crystal concentration and a PEG 8 x 10^6 concentration of 9.65% was tested in an untreated 50-μm inner diameter capillary. The bulbous growth did not occur with this sample.

A sample of PS-I crystals of about 2 μm in size was combined with PEG 8 x 10^6 in water for an overall PEG 8 x 10^6 concentration of 13.78% and tested with a 50-μm inner diameter capillary. Contrary to what was expected, this extrusion resembled that of the 7% PEG 8 x 10^6 concentration more so than that of the 11% PEG 8 x 10^6 concentration. The sample of PS-II crystals, which contained crystals ranging in size from 2 to 20 μm and which was mixed to a final PEG 8 x 10^6 concentration of 13.8% and tested in a 50-μm inner diameter capillary, performed very similarly to the 11% PEG 8 x 10^6 concentration tests with PEG only. This sample was purposefully interrupted several times at different flow rates and recovered without any assistance. A 20-μm inner diameter capillary was used with the same sample with similar results (Figure 53).

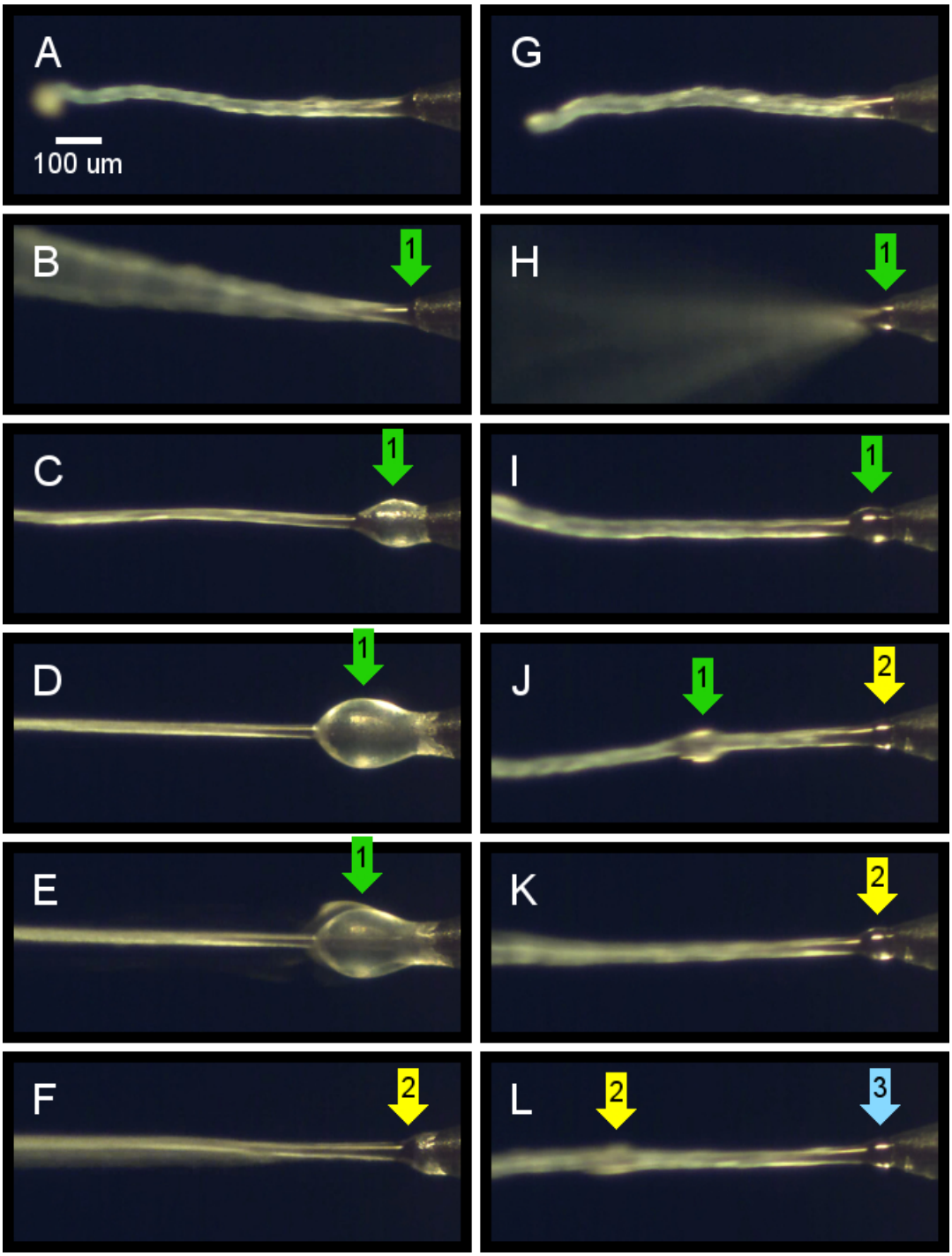

Figure 52: A phycocyanin crystal sample mixed with PEG 8 x 10^6 in water for an overall PEG 8 x 10^6 concentration of 13% was tested with an untreated (left column) and a treated (right column) 50-µm inner diameter capillary. The bulbous growth that gradually formed at the capillary tip grew large when using an untreated capillary (A through F); the growth was small and detached more frequently when using a treated capillary (G through L), although the effect appeared to diminish with time. The colored/numbered arrows track the growths in each situation.

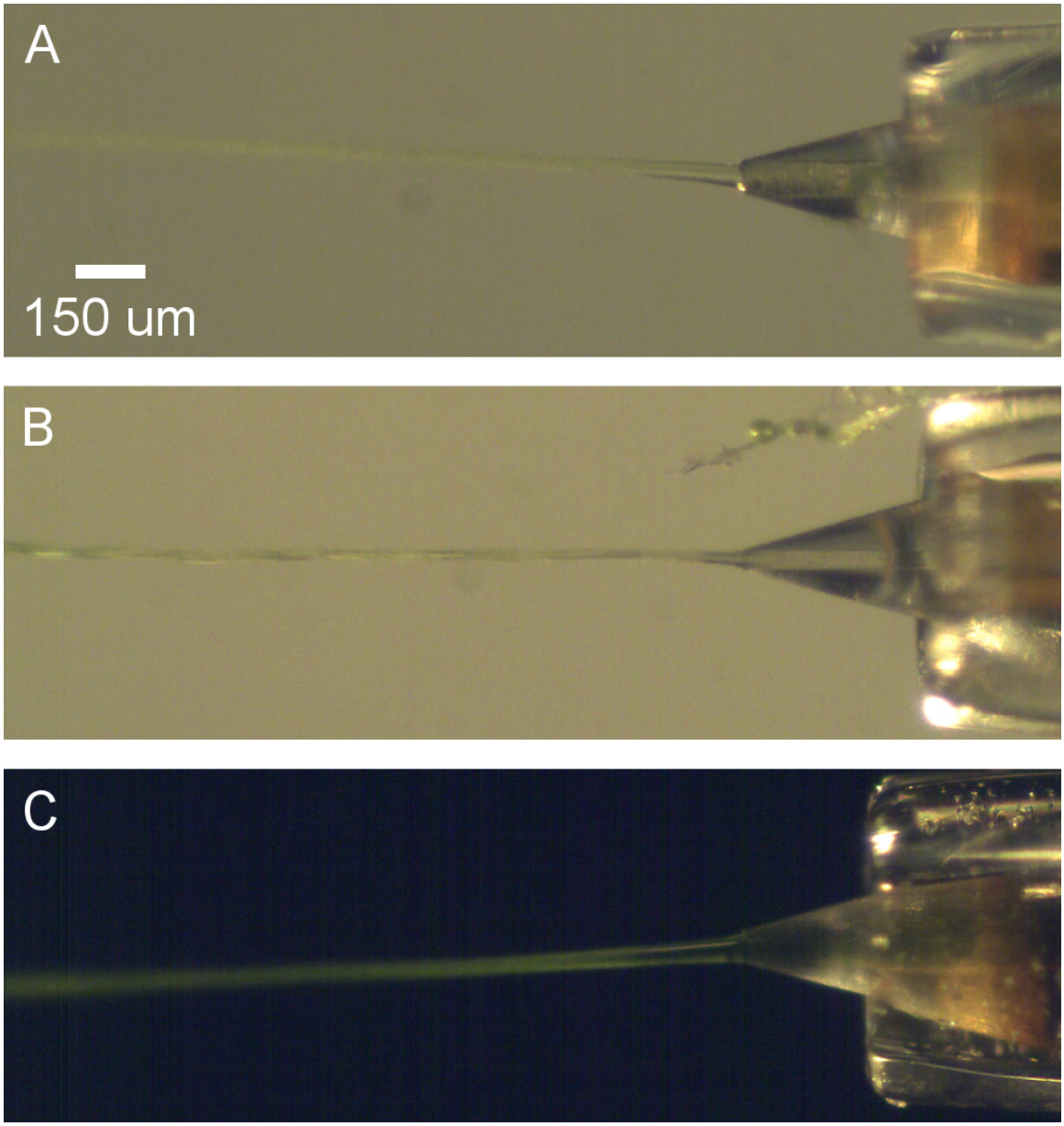

Figure 53: A) Extrusion of PS-II crystals mixed with PEG 8 x 10^6 to a final PEG 8 x 10^6 concentration of 13.8% using a 50-µm inner diameter capillary in atmospheric conditions. The performance of this extrusion was similar to the 11% PEG 8 x 10^6 in water tests with PEG only. This extrusion was purposefully interrupted several times while flowing at different flow rates and restarted remotely each time without any special assistance. B) A 20-µm inner diameter capillary was used with the same sample with similar results. C) A sample of PS-I crystals of about 2 µm in size was combined with PEG 8 x 10^6 at an overall PEG 8 x 10^6 concentration of 13.78% and tested with a 50-µm inner diameter capillary. In contrast to the PS-II tests, this extrusion resembled that of the 7% PEG 8 x 10^6 in water tests with PEG-only more so than that of the 11% PEG 8 x 10^6 in water tests with PEG-only.

PS-1 and PS-II crystals mixed with 13.5% PEG 8 x 10^6, Phycocyanin crystals mixed with 11% and 12% PEG 8 x 10^6, and FLPP3 crystals mixed with at 12% PEG 8 x 10^6 were imaged with an optical microscope to test for appearance and birefringence. SONICC images were also taken. The imaging tests indicated that all protein crystals survived after being mixed with PEG 8 x 10^6. These images are contained in Appendix B.

4.3.5 Discussion and Conclusions

For the sample-free 7% PEG 8 x 10^6 in water concentrations and for some of the crystal samples, the tendency of the high molecular weight PEG mediums to "blob up" on the tip of the capillary could be seen in both vacuum and atmosphere and could be categorized in at least two ways: (1) the emerging medium immediately adheres to the capillary tip and then continues to grow; (2) the medium emerges a few hundred microns and then flips back onto the tip, obstructing flow and causing collection at the tip. The first situation appeared to be attributable to the medium itself: i.e. too low PEG concentration. The second situation is likely a result of issues related to the gas flow, although charging may be involved in the "flipping" of the stream backward toward the nozzle tip. In both cases, flow rate may have an effect (i.e. starting with too low of a flow rate as pressure on the HPLC pump slowly builds). However, there were cases when ramping up pressure very quickly showed no improvement.

Effects (1) and (2) were in tests of sample-free PEG 8 x 10^6 in water at 7% concentration were remotely correctable when operating in vacuum by utilizing certain combinations of gas pressure and flow rate extremes, whereas in atmospheric operation steady extrusions were not accomplished for this condition. Capillaries that were surface

treated to be hydrophobic were tested during this trial for comparison. The tendencies described earlier as (1) and (2) were still present but to a lesser extent. Stable extrusion in atmospheric conditions was possible with water spraying and hand wiping of the capillary tip when using the treated capillary. Behavior in vacuum improved as well. The benefits of surface treatments would be better ascertained with additional trials with as careful control of experimental variables as possible (the geometry of the gas aperture and capillary both in terms of their individual shape and relative position is currently difficult to reproduce). However, the aim of this phase of the study was not to thoroughly characterize the effect of surface treatments, but rather to explore a single condition of PEG weight and concentration. Had the effect of surface treatments been more pronounced, further work in this direction may have been pursued.

Sample-free PEG 8 x 10^6 at 11% concentration in water did not appear to have a problem with either of these situations, (1) or (2), in either atmosphere or vacuum. Sample-free PEG 1 x 10^6 at 11% concentration in water was tested in vacuum conditions only and also did not appear to have a problem with (1) or (2).

The precious nature of crystal samples hinders a more extensive study of flow behavior with a specific sample. Nevertheless, with these results it is clear that the high molecular weight PEG shows promise as a versatile crystal-carrying medium. The crystals mixed in PEG 8 x 10^6 were imaged at PETRA-III, and were found to diffract as expected.

Many variables still need to be explored, such as the effect of dehydration from both helium flow and the vacuum environment, especially as it relates to background levels that may be experienced when probing the stream under vacuum conditions. How

the dehydration effects may affect the survivability of crystals is also an important question to be addressed. Presumably this is only answerable by in-vacuum diffraction experiments. The usefulness of surface treating the capillary is also a rich area of exploration.

REFERENCES

Abdallah, et al. (2015). Microfluidic sorting of protein nanocrystals by size for X-ray free-electron laser diffraction. *Structural Dynamics*, *2*(4), 041719.

Abdallah, B. G., Chao, T. C., Kupitz, C., Fromme, P., and Ros, A. (2013). Dielectrophoretic sorting of membrane protein nanocrystals. *ACS nano*, 7(10), 9129-9137.

Bae, B., Han, J., Masel, R., and Shannon, M. (2007). A bidirectional electrostatic microvalve with microsecond switching performance. *Microelectromechanical Systems, Journal of*, 16(6), 1461-1471.

Beyerlein, K. R., et al. (2015) Ceramic Micro-Injection Molded Nozzles for Serial Femtosecond Crystallography Sample Delivery. Currently in review.

Bogan, M. J. (2013). X-ray free electron lasers motivate bioanalytical characterization of protein nanocrystals: serial femtosecond crystallography. *Analytical chemistry*, 85(7), 3464-3471.

Botha, S., et al. (2015). Room-temperature serial crystallography at synchrotron X-ray sources using slowly flowing free-standing high-viscosity microstreams. *Acta Crystallographica Section D: Biological Crystallography*, D71, 387-397.

Boutet, S., et al. (2012). High-resolution protein structure determination by serial femtosecond crystallography. *Science*, 337(6092), 362-364.

Burmeister, W. P. (2000). Structural changes in a cryo-cooled protein crystal owing to radiation damage. *Acta Crystallographica Section D: Biological Crystallography*, 56(3), 328-341.

Carugo, O., and Carugo, K. D. (2005). When X-rays modify the protein structure: radiation damage at work. *Trends in biochemical sciences*, 30(4), 213-219.

Chapman, H. N., et al. (2011). Femtosecond X-ray protein nanocrystallography. *Nature*, 470(7332), 73-77.

Conrad, C. E., et al. (2015). A novel inert crystal delivery medium for serial femtosecond crystallography. *IUCrJ*, 2(4), 421-430.

DePonte, D. P., Mckeown, J. T., Weierstall, U., Doak, R. B., and Spence, J. C. H. (2011). Towards ETEM serial crystallography: electron diffraction from liquid jets. *Ultramicroscopy*, 111(7), 824-827.

DePonte, D. P., Weierstall, U., Schmidt, K., Warner, J., Starodub, D., Spence, J. C. H., and Doak, R. B. (2008). Gas dynamic virtual nozzle for generation of microscopic droplet streams. *Journal of Physics D: Applied Physics*, 41(19), 195505.

Doak, R. B., et al. (2012). Microscopic linear liquid streams in vacuum: Injection of solvated biological samples into X-ray free electron lasers. In *AIP Conference Proceedings-American Institute of Physics* (Vol. 1501, No. 1, p. 1314).

Ebagninin, K. W., Benchabane, A., and Bekkour, K. (2009). Rheological characterization of poly (ethylene oxide) solutions of different molecular weights. *Journal of colloid and interface science*, 336(1), 360-367.

Echelmeier, A, et al. (2015) Biphasic droplet-based sample delivery of protein crystals for serial femtosecond crystallography with an X-ray free electron laser. To be published in proceeding of *MicroTAS 2015 Conference*.

Fraser, J. S., van den Bedem, H., Samelson, A. J., Lang, P. T., Holton, J. M., Echols, N., and Alber, T. (2011). Accessing protein conformational ensembles using room-temperature X-ray crystallography. *Proceedings of the National Academy of Sciences*, 108(39), 16247-16252.

Gañán-Calvo, A. M. (1998). Generation of steady liquid microthreads and micron-sized monodisperse sprays in gas streams. *Physical Review Letters*, *80*(2), 285.

Ganán-Calvo, A. M. (2004). Perfectly monodisperse microbubbling by capillary flow focusing: An alternate physical description and universal scaling. *Physical Review E*, 69(2), 027301.

Ganán-Calvo, A. M. and Gordillo, J. M. (2001). Perfectly monodisperse microbubbling by capillary flow focusing. *Physical review letters*, 87(27), 274501.

Han, M., Lee, W., Lee, S. K., and Lee, S. S. (2004). 3D microfabrication with inclined/rotated UV lithography. *Sensors and Actuators A: Physical*, 111(1), 14-20.

James, D. (2015). Injection Methods and Instrumentation for Serial X-ray Free Electron Laser Experiments (Doctoral dissertation, Arizona State University).

Kelly, R. T, Wang, C., Rausch, S. J., Lee, C. S., and Tang, K. (2014). Pneumatic Microvalve-Based Hydrodynamic Sample Injection for High-Throughput, Quantitative Zone Electrophoresis in Capillaries. *Analytical chemistry*, 86(13), 6723-6729.

Kirian, R. A. (2012). Structure determination through correlated fluctuations in x-ray scattering. *Journal of Physics B: Atomic, Molecular and Optical Physics*, 45(22), 223001.

Lawrence, R. M., et al. (2015). Serial femtosecond X-ray diffraction of enveloped virus microcrystals. *Structural Dynamics*, *2*(4), 041720.

Li, Y., Zhang, D., Feng, X., Xu, Y., and Liu, B. F. (2012). A microsecond microfluidic mixer for characterizing fast biochemical reactions. *Talanta*, 88, 175-180.

Liu, W., et al. (2013). Serial femtosecond crystallography of G protein–coupled receptors. *Science*, 342(6165), 1521-1524.

Mao, X., Juluri, B. K., Lapsley, M. I., Stratton, Z. S., and Huang, T. J. (2010). Milliseconds microfluidic chaotic bubble mixer. *Microfluidics and Nanofluidics*, 8(1), 139-144.

McNeil, B. W., and Thompson, N. R. (2010). X-ray free-electron lasers. *Nature photonics*, 4(12), 814-821.

Montanero, J. M., Acero, A. J., and Vega, E. J. (2010). Micrometer glass nozzles for flow focusing. *Journal of Micromechanics and Microengineering*, 20(7), 075035.

Mueller, M., Jenni, S., and Ban, N. (2007). Strategies for crystallization and structure determination of very large macromolecular assemblies. *Current opinion in structural biology*, 17(5), 572-579.

Neutze, R., Wouts, R., van der Spoel, D., Weckert, E., and Hajdu, J. (2000). Potential for biomolecular imaging with femtosecond X-ray pulses. *Nature*, 406(6797), 752-757.

Nguyen, N. T. (2011). *Micromixers: fundamentals, design and fabrication*. NY: William Andrew Inc.

Nogly, P., et al. (2015). Lipidic cubic phase serial millisecond crystallography using synchrotron radiation. *IUCrJ*, 2(2), 0-0.

Paganin, D., Mayo, S. C., Gureyev, T. E., Miller, P. R., and Wilkins, S. W. (2002). Simultaneous phase and amplitude extraction from a single defocused image of a homogeneous object. *Journal of microscopy*, 206(1), 33-40.

Parida, O. P., and Bhat, N. (2009). Characterization of optical properties of SU-8 and fabrication of optical components. In *Proceedings of the International Conference on Optics and Photonics*, Chandigarh, India (Vol. 30).

Qin, D., Xia, Y., and Whitesides, G. M. (2010). Soft lithography for micro-and nanoscale patterning. *Nature protocols*, 5(3), 491-502.

Lord Rayleigh. (1879). On the capillary phenomena of jets. *Proceedings of the Royal Society of London*, 29, 71-97.

Rack, A. et al. (2009). The micro-imaging station of the TopoTomo beamline at the ANKA synchrotron light source. *Nuclear Instruments and Methods in Physics Research Section B: Beam Interactions with Materials and Atoms*, *267*(11), 1978-1988.

Reba, I. (1966). Applications of the Coanda effect. *Scientific American*, 214, 84-92.

Sato, H., Yagyu, D., Ito, S., and Shoji, S. (2006). Improved inclined multi-lithography using water as exposure medium and its 3D mixing microchannel application. *Sensors and Actuators A: Physical*, 128(1), 183-190.

Schlichting, I., and Miao, J. (2012). Emerging opportunities in structural biology with X-ray free-electron lasers. *Current opinion in structural biology*, 22(5), 613-626.

Shapiro, D. A., et al. (2008). X-Ray Powder Diffraction from Sub-Micron Crystals of Photosystem-1 Membrane Protein. arXiv preprint arXiv:0803.4027.

Solem, J.S. (1986). Imaging biological specimens with high-intensity soft x rays *J. Opt Soc Am*. **3**, 1551.

Spence, J. C. H., Weierstall, U., and Chapman, H. N. (2012). X-ray lasers for structural and dynamic biology. *Reports on Progress in Physics*, 75(10), 102601.

Spence, J. C. H. and Doak, R. B. (2004). Single Molecular Imaging. *Phys Rev Letts*, 92, 198102

Sugahara, M. et al. (2015). Grease matrix as a versatile carrier of proteins for serial crystallography. *Nature methods*, 12(1), 61-63.

Taylor, G. I. (1934). The formation of emulsions in definable fields of flow. *Proceedings of the Royal Society of London. Series A, Containing Papers of a Mathematical and Physical Character*, 501-523.

Tesař, V. (2009). Fluidic control of reactor flow—Pressure drop matching. *Chemical Engineering Research and Design*, 87(6), 817-832.

Thompson, R. (1971). Supersonic fluidic switch. U.S. Patent 3,570,512.

Thorslund, S., Johannesson, N., Nikolajeff, F., and Bergquist, J. (2007). A simplified method for capillary embedment into microfluidic devices exemplified by sol-gel based preconcentration. *Electrophoresis*, 28(24), 4758-4764.

Thorsen, T., Roberts, R. W., Arnold, F. H., and Quake, S. R. (2001). Dynamic pattern formation in a vesicle-generating microfluidic device. *Physical review letters*, 86(18), 4163.

Trebbin, M., Krüger, K., DePonte, D., Roth, S. V., Chapman, H. N., and Förster, S. (2014). Microfluidic liquid jet system with compatibility for atmospheric and high-vacuum conditions. *Lab on a chip*, 14(10), 1733-1745.

Vogelgesang, M., et al. Real-time Image Processing and Reconstruction for Synchrotron Experiments. To be submitted to *Journal of Synchrotron Radiation.*

Wang, D. (2014). Methods and Instrumentation of Sample Injection for XFEL Experiments. Doctoral dissertation, Arizona State University.

Weierstall, U. (2014). Liquid sample delivery techniques for serial femtosecond crystallography. *Philosophical Transactions of the Royal Society of London B: Biological Sciences*, 369(1647), 20130337.

Weierstall, U. et al. (2014). Lipidic cubic phase injector facilitates membrane protein serial femtosecond crystallography. *Nature communications*, 5.

Weierstall, U., Doak, R. B., and Spence, J. C. H. (2011). A pump-probe XFEL particle injector for hydrated samples. arXiv preprint arXiv:1105.2104.

Zhang, H. et al. (2015). Structure of the Angiotensin Receptor Revealed by Serial Femtosecond Crystallography. *Cell*, 161(4), 833-844.

Zhang, Y. L., Chen, Q. D., Xia, H., and Sun, H. B. (2010). Designable 3D nanofabrication by femtosecond laser direct writing. *Nano Today*, 5(5), 435-448.

APPENDIX A

ADDITIONAL APPLICATIONS IN SERIAL CRYSTALLOGRAPHY

1. Serial femtosecond X-ray diffraction of enveloped virus microcrystals

(Lawrence et al., 2015)

Serial femtosecond crystallography (SFX) using X-ray free-electron lasers has produced high-resolution, room temperature, time-resolved protein structures. We report preliminary SFX of Sindbis virus, an enveloped icosahedral RNA virus with 700 A˚ diameter. Microcrystals delivered in viscous agarose medium diffracted to 40 A˚ resolution. Small-angle diffuse X-ray scattering overlaid Bragg peaks and analysis suggests this results from molecular transforms of individual particles. Viral proteins undergo structural changes during entry and infection, which could, in principle, be studied with SFX. This is an important step toward determining room temperature structures from virus microcrystals that may enable time-resolved studies of enveloped viruses.

2. **Microfluidic sorting of protein nanocrystals by size for X-ray free-electron laser diffraction**

(Abdallah, et al., 2015)

The advent and application of the X-ray free-electron laser (XFEL) has uncovered the structures of proteins that could not previously be solved using traditional crystallography. While this new technology is powerful, optimization of the process is still needed to improve data quality and analysis efficiency. One area is sample heterogeneity, where variations in crystal size (among other factors) lead to the requirement of large data sets (and thus 10–100mg of protein) for determining accurate structure factors. To decrease sample dispersity, we developed a high-throughput

microfluidic sorter operating on the principle of dielectrophoresis, whereby polydisperse particles can be transported into various fluid streams for size fractionation. Using this microsorter, we isolated several milliliters of photosystem I nanocrystal fractions ranging from 200 to 600 nm in size as characterized by dynamic light scattering, nanoparticle tracking, and electron microscopy. Sorted nanocrystals were delivered in a liquid jet via the gas dynamic virtual nozzle into the path of the XFEL at the Linac Coherent Light Source. We obtained diffraction to 4 A˚resolution, indicating that the small crystals were not damaged by the sorting process. We also observed the shape transforms of photosystem I nanocrystals, demonstrating that our device can optimize data collection for the shape transform-based phasing method. Using simulations, we show that narrow crystal size distributions can significantly improve merged data quality in serial crystallography. From this proof-of-concept work, we expect that the automated size-sorting of protein crystals will become an important step for sample production by reducing the amount of protein needed for a high quality final structure and the development of novel phasing methods that exploit inter-Bragg reflection intensities or use variations in beam intensity for radiation damage-induced phasing. This method will also permit an analysis of the dependence of crystal quality on crystal size.

3. **A novel inert crystal delivery medium for serial femtosecond crystallography**

(Conrad et al., 2015)

Serial femtosecond crystallography (SFX) has opened a new era in crystallography by permitting nearly damage-free, room-temperature structure determination of challenging proteins such as membrane proteins. In SFX, femtosecond X-ray free-electron laser pulses produce diffraction snapshots from nanocrystals and microcrystals delivered in a liquid jet, which leads to high protein consumption. A slow-moving stream of agarose has been developed as a new crystal delivery medium for SFX. It has low background scattering, is compatible with both soluble and membrane proteins, and can deliver the protein crystals at a wide range of temperatures down to 4C. Using this crystal-laden agarose stream, the structure of a multi-subunit complex, phycocyanin, was solved to 2.5 A˚resolution using 300 mg of microcrystals embedded into the agarose medium post-crystallization. The agarose delivery method reduces protein consumption by at least 100-fold and has the potential to be used for a diverse population of proteins, including membrane protein complexes.

4. **Batch crystallization of rhodopsin for structural dynamics using an X-ray free-electron laser**

Wu, W., et al. (2015). Batch crystallization of rhodopsin for structural dynamics using an X-ray free-electron laser. *Acta Crystallographica Section F: Structural Biology Communications*, *71*(7), 856-860.

Rhodopsin is a membrane protein from the G protein-coupled receptor family. Together with its ligand retinal, it forms the visual pigment responsible for night vision. In order to perform ultrafast dynamics studies, a time-resolved serial femtosecond crystallography method is required owing to the nonreversible activation of rhodopsin. In such an approach, microcrystals in suspension are delivered into the X-ray pulses of an X-ray free-electron laser (XFEL) after a precise photoactivation delay. Here, a milliliter batch production of high-density microcrystals was developed by four methodical conversion steps starting from known vapor-diffusion crystallization protocols: (i) screening the low-salt crystallization conditions preferred for serial crystallography by vapor diffusion, (ii) optimization of batch crystallization, (iii) testing the crystal size and quality using second-harmonic generation (SHG) imaging and X-ray powder diffraction and (iv) production of milliliters of rhodopsin crystal suspension in batches for serial crystallography tests; these crystals diffracted at an XFEL at the Linac Coherent Light Source using a liquid-jet setup.

5. **Structure of the Angiotensin Receptor Revealed by Serial Femtosecond Crystallography**

(Zhang et al., 2015)

Angiotensin II type 1 receptor (AT1R) is a G protein- coupled receptor that serves as a primary regulator for blood pressure maintenance. Although several anti-hypertensive drugs have been developed as AT1R blockers (ARBs), the structural basis for AT1R ligand-binding and regulation has remained elusive, mostly due to the difficulties of growing high-quality crystals for structure determination using synchrotron radiation. By applying the recently developed method of serial femtosecond crystallography at an X-ray free-electron laser, we successfully deter- mined the room-temperature crystal structure of the human AT1R in complex with its selective antagonist ZD7155 at 2.9-A˚ resolution. The AT1R-ZD7155 complex structure revealed key structural features of AT1R and critical interactions for ZD7155 binding. Docking simulations of the clinically used ARBs into the AT1R structure further elucidated both the common and distinct binding modes for these anti- hypertensive drugs. Our results thereby provide fundamental insights into AT1R structure-function relationship and structure-based drug design.

6. **Lipidic cubic phase serial millisecond crystallography using synchrotron radiation**

(Nogly et al., 2015)

Lipidic cubic phases (LCPs) have emerged as successful matrixes for the crystallization of membrane proteins. Moreover, the viscous LCP also provides a highly effective delivery medium for serial femtosecond crystallography (SFX) at X-ray free-electron lasers (XFELs). Here, the adaptation of this technology to perform serial millisecond crystallography (SMX) at more widely available synchrotron microfocus beamlines is described. Compared with conventional microcrystallography, LCP-SMX eliminates the need for difficult handling of individual crystals and allows for data collection at room temperature. The technology is demonstrated by solving a structure of the light-driven proton- pump bacteriorhodopsin (bR) at a resolution of 2.4 A˚. The room-temperature structure of bR is very similar to previous cryogenic structures but shows small yet distinct differences in the retinal ligand and proton-transfer pathway.

7. **Lipidic cubic phase injector facilitates membrane protein serial femtosecond crystallography**

(Weierstall et al., 2014)

Lipidic cubic phase (LCP) crystallization has proven successful for high-resolution structure determination of challenging membrane proteins. Here we present a technique for extruding gel-like LCP with embedded membrane protein microcrystals, providing a continuously renewed source of material for serial femtosecond crystallography. Data

collected from sub- 10-mm-sized crystals produced with less than 0.5mg of purified protein yield structural insights regarding cyclopamine binding to the smoothened receptor.

8. **Serial Femtosecond Crystallography of G Protein–Coupled Receptors**

(Liu et al., 2013)

X-ray crystallography of G protein–coupled receptors and other membrane proteins is hampered by difficulties associated with growing sufficiently large crystals that withstand radiation damage and yield high-resolution data at synchrotron sources. We used an x-ray free-electron laser (XFEL) with individual 50-femtosecond-duration x-ray pulses to minimize radiation damage and obtained a high-resolution room-temperature structure of a human serotonin receptor using sub-10-micrometer microcrystals grown in a membrane mimetic matrix known as lipidic cubic phase. Compared with the structure solved by using traditional microcrystallography from cryo-cooled crystals of about two orders of magnitude larger volume, the room-temperature XFEL structure displays a distinct distribution of thermal motions and conformations of residues that likely more accurately represent the receptor structure and dynamics in a cellular environment.

APPENDIX B

IMAGES OF CRYSTAL SAMPLES MIXED WITH PEG 8 X 10^6

11 % PEG 8 x 10^6 in water mixed with Phycocyanin crystal solution:

Optical microscopy

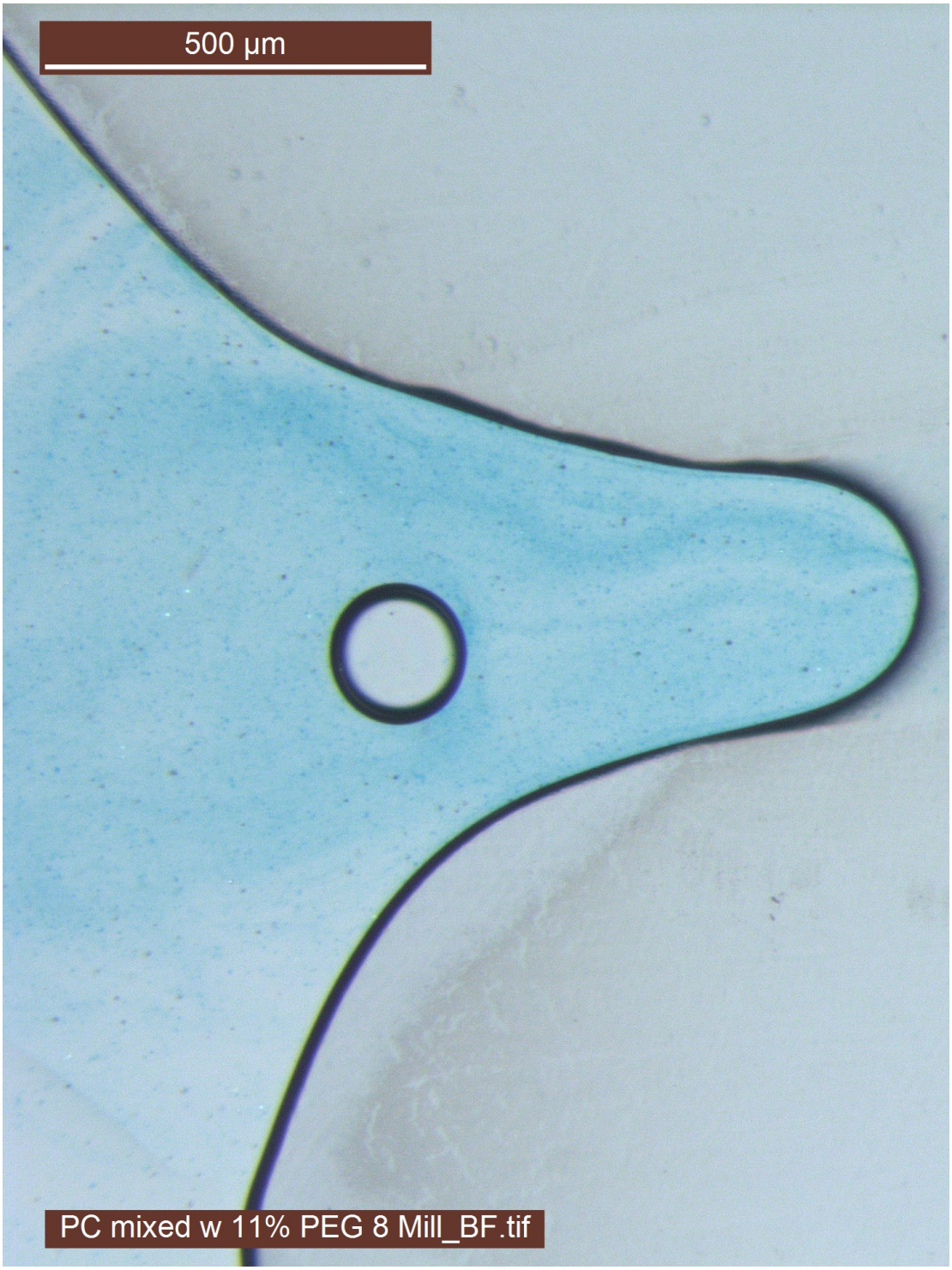

11 % PEG 8 x 10^6 in water mixed with Phycocyanin crystal solution:

Birefringence

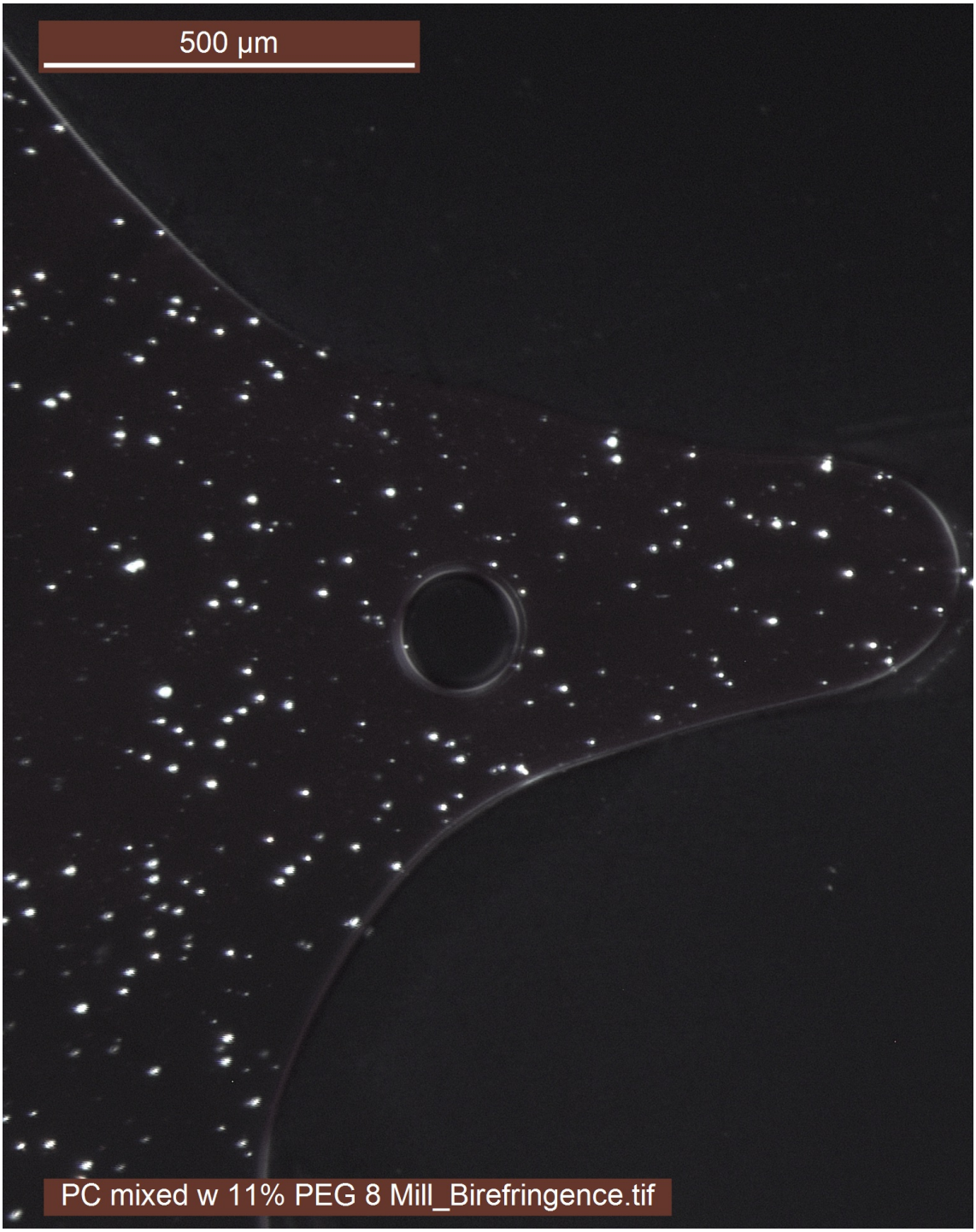

12 % PEG 8 x 10^6 in water mixed with Phycocyanin crystal solution:

Close view of crystals

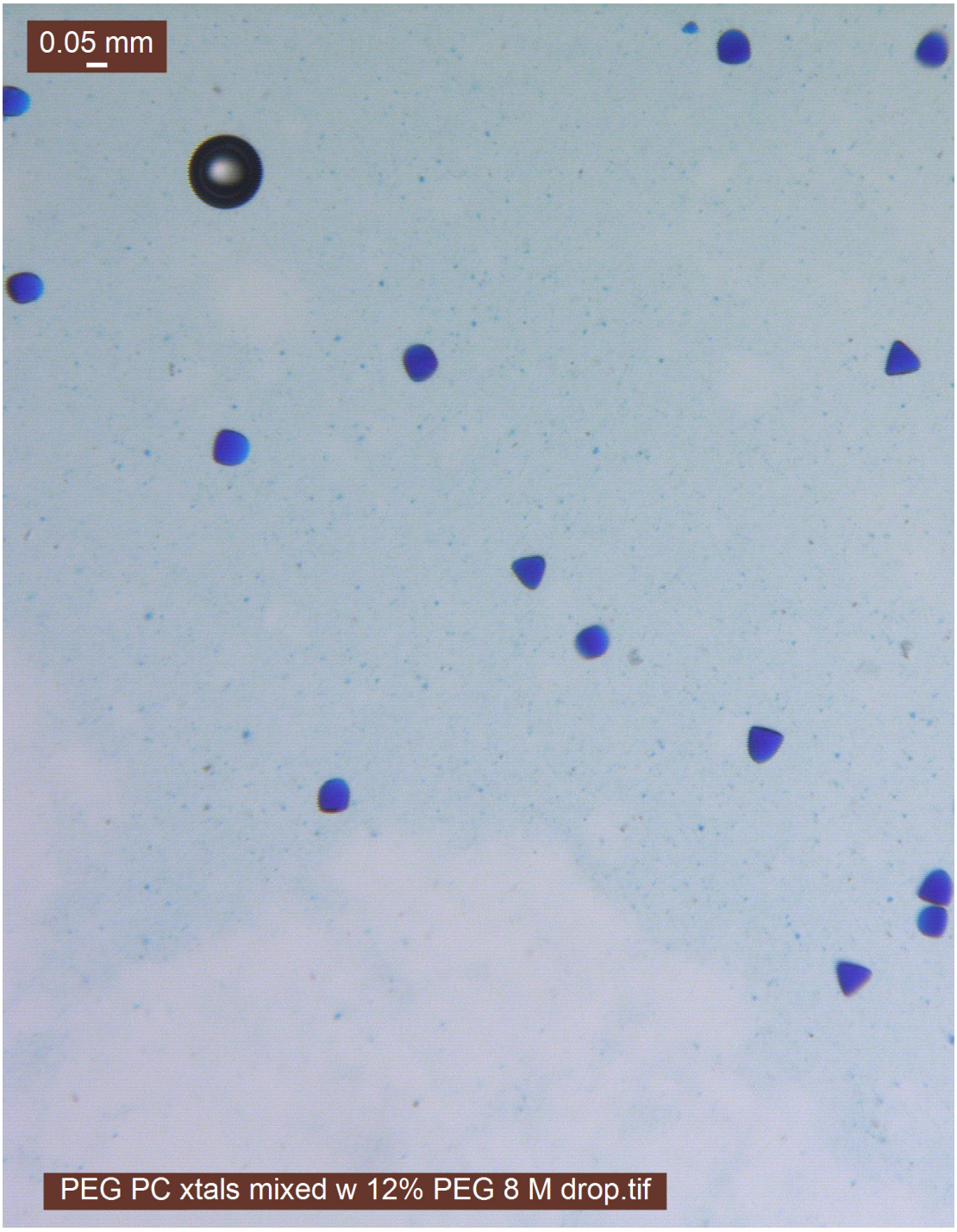

PEG 8 x 10^6 in water mixed with Phycocyanin crystal solution:

In loading syringe

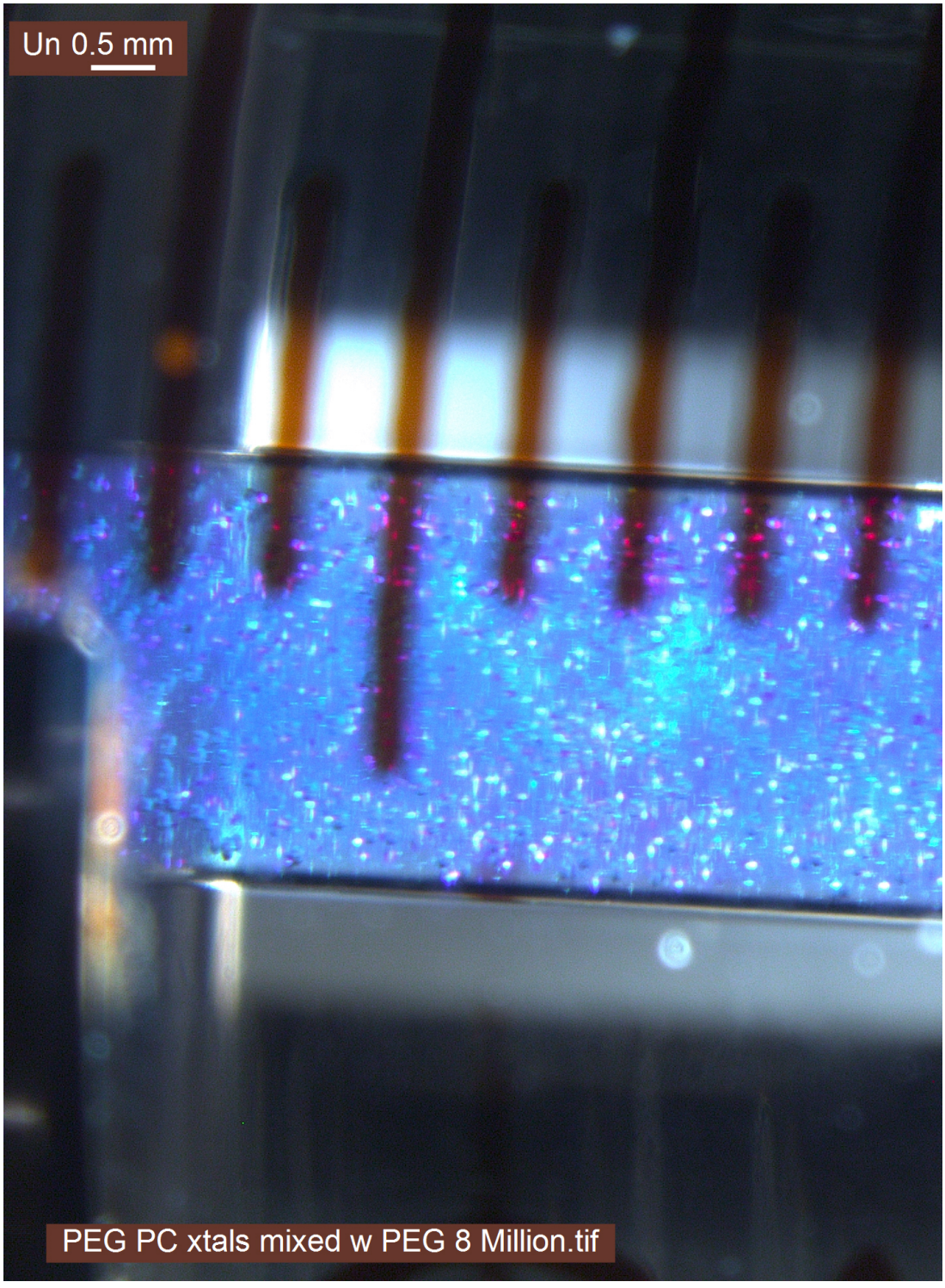

12% PEG 8 x 10^6 in water mixed with FLPP3 crystal solution:

SONICC prep

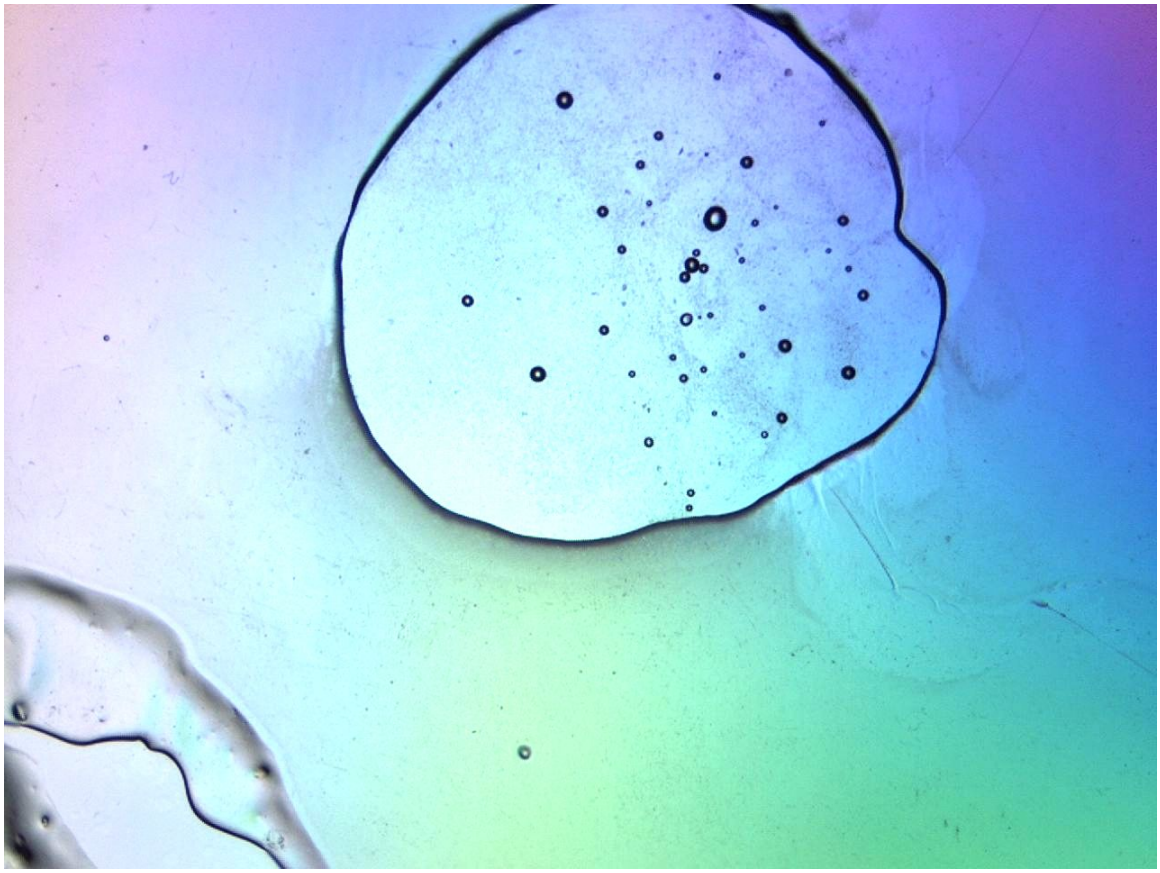

12% PEG 8 x 10^6 in water mixed with FLPP3 crystal solution:

SONICC signal

13.5% PEG 8 x 10^6 in water mixed with PS-II crystal solution 18 hours after:

Optical microscopy

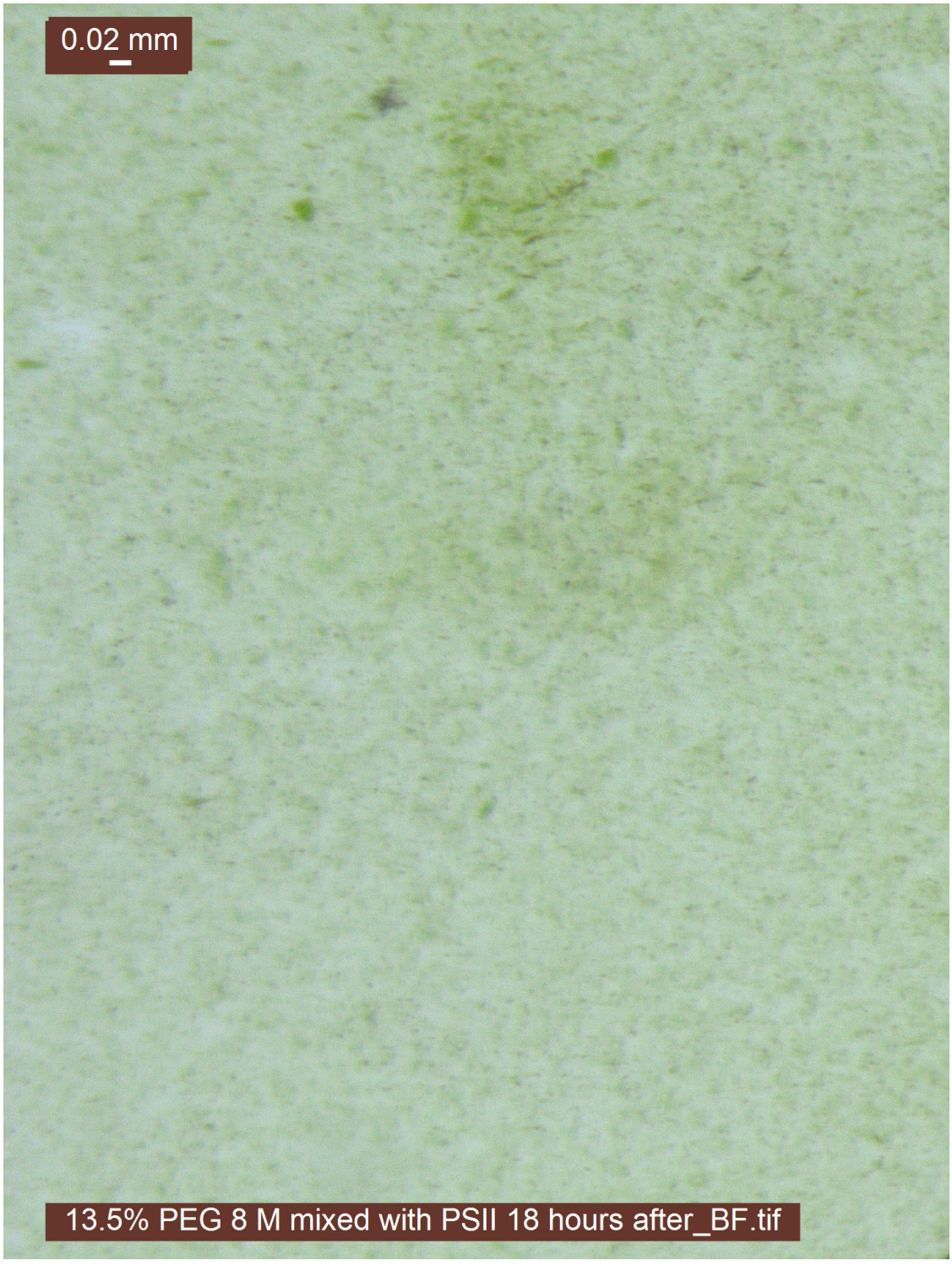

13.5% PEG 8 x 10^6 in water mixed with PS-II crystal solution 18 hours after:

Birefringence

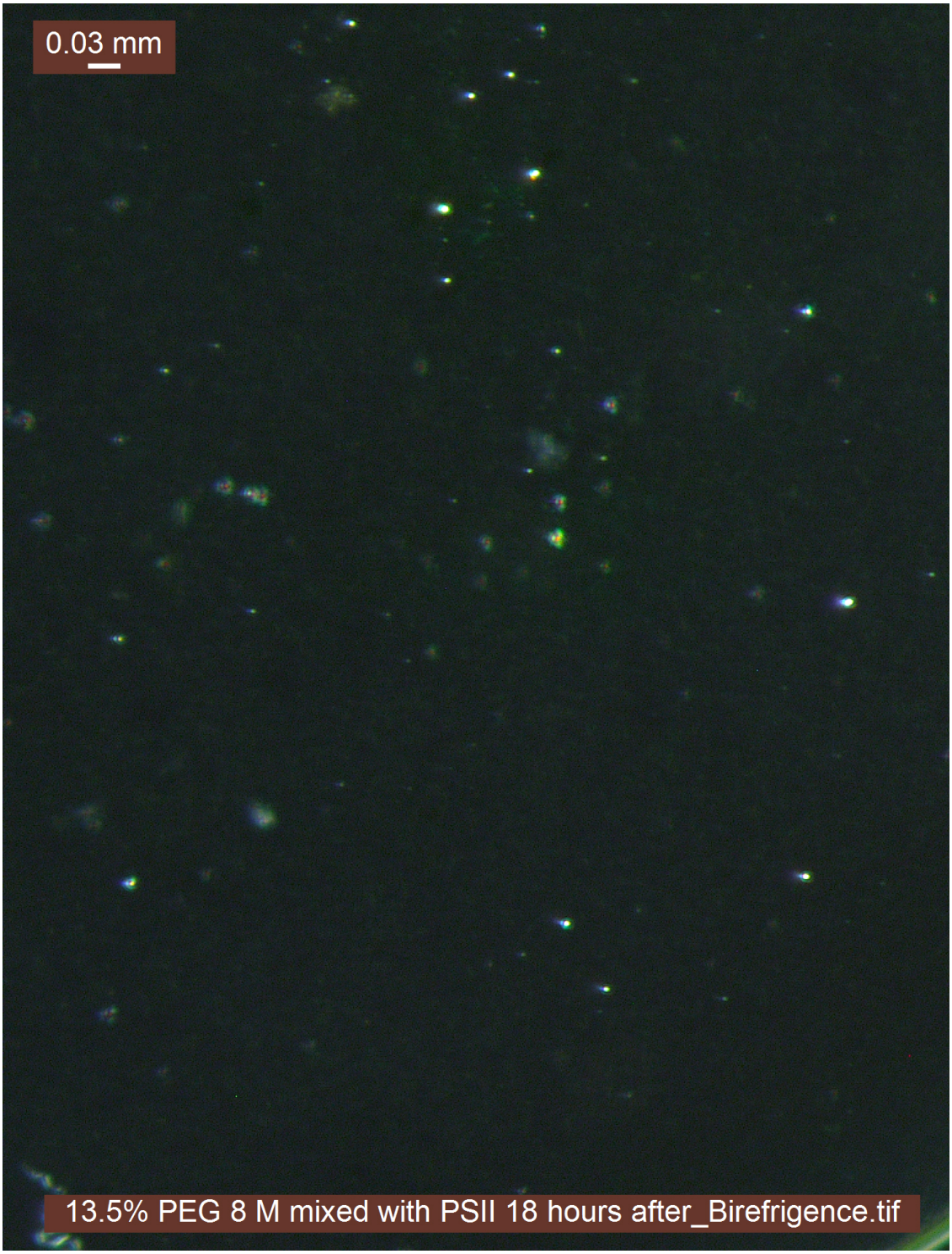

13.5% PEG 8 x 10^6 in water mixed with PS-I crystal solution after 18 hours:

Optical microscopy

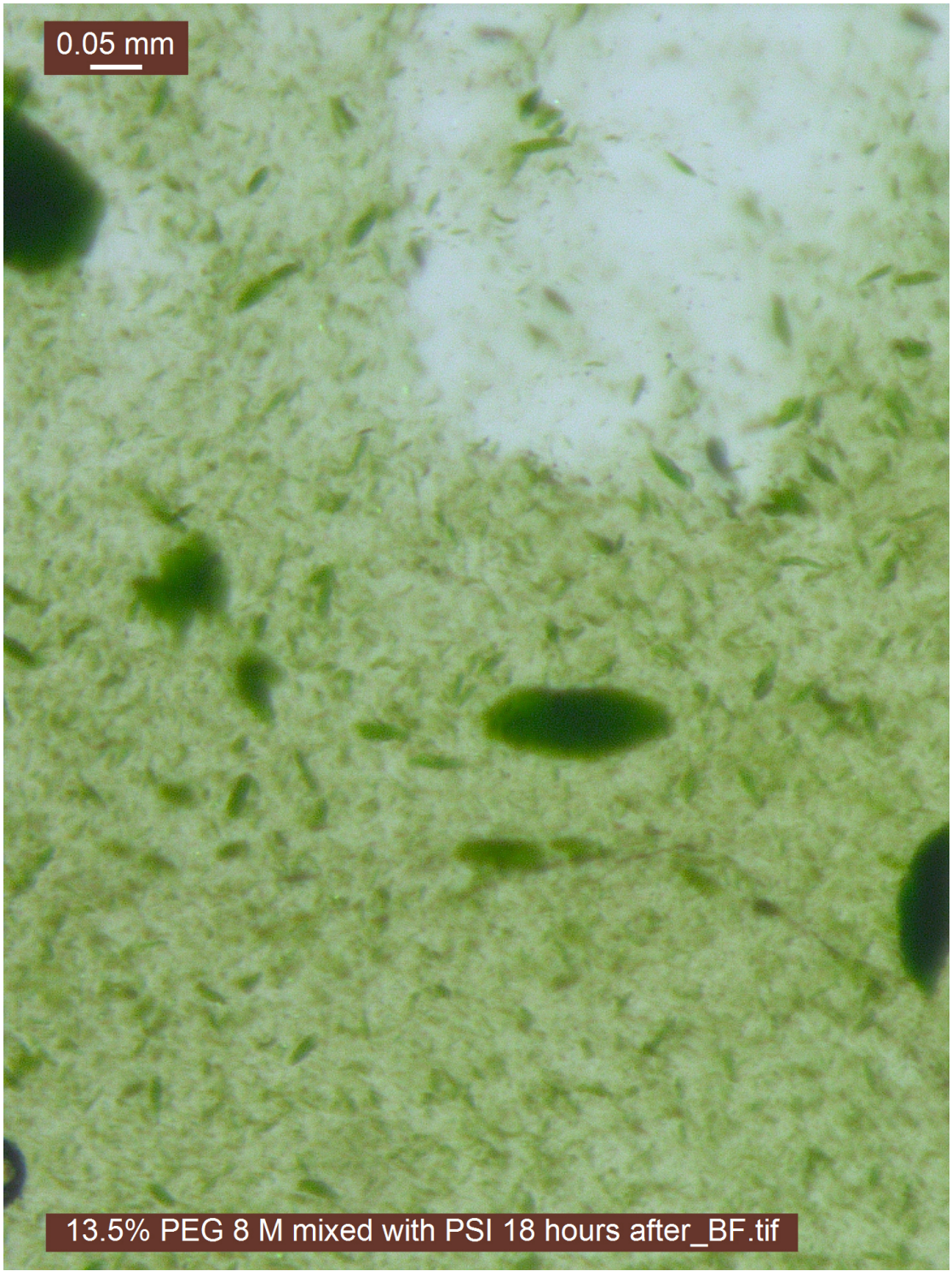

13.5% PEG 8 x 10^6 in water mixed with PS-I crystal solution after 18 hours:

Birefringence

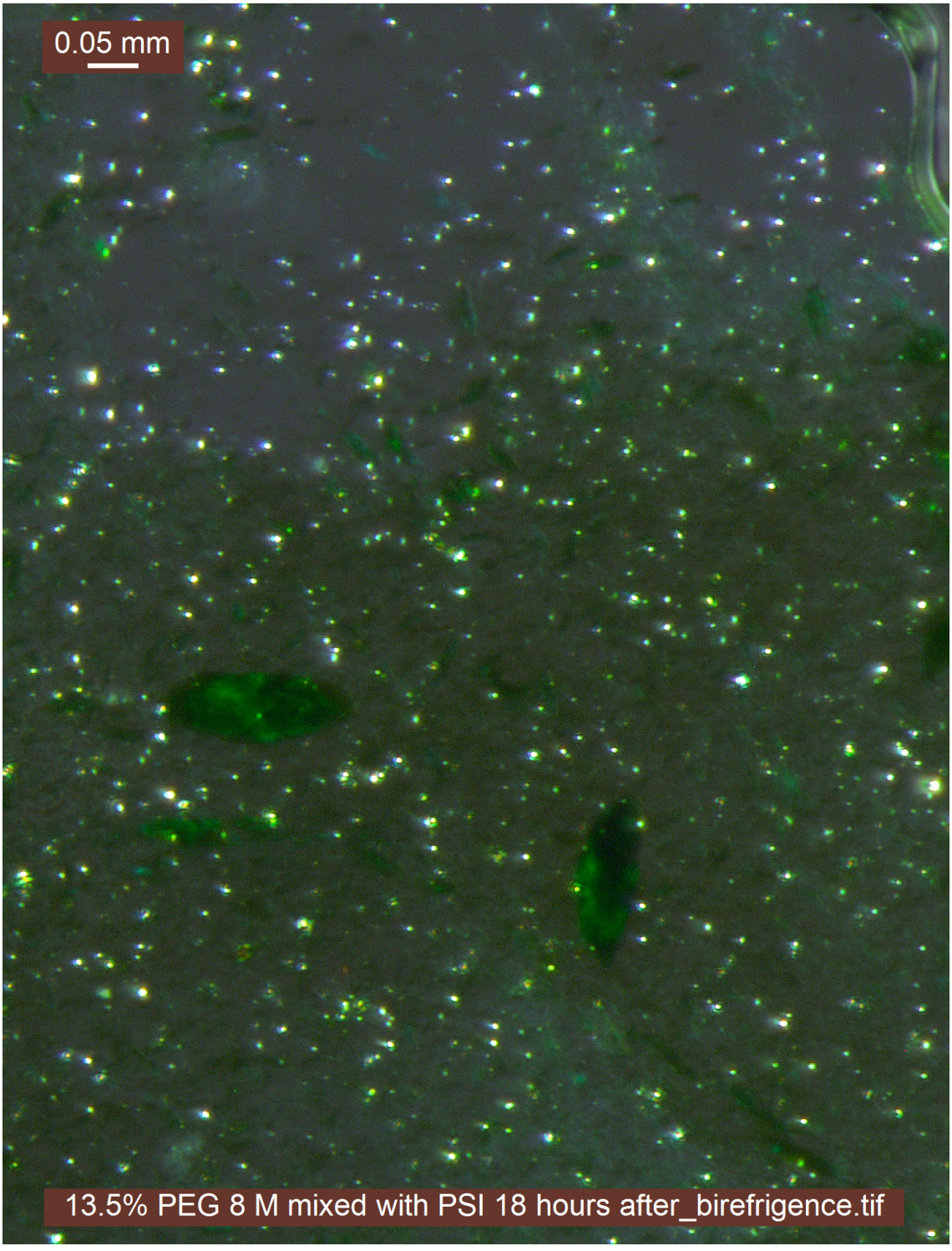

15% PEG 8 x 10^6 in water mixed with PS-I crystal solution:

SONICC prep

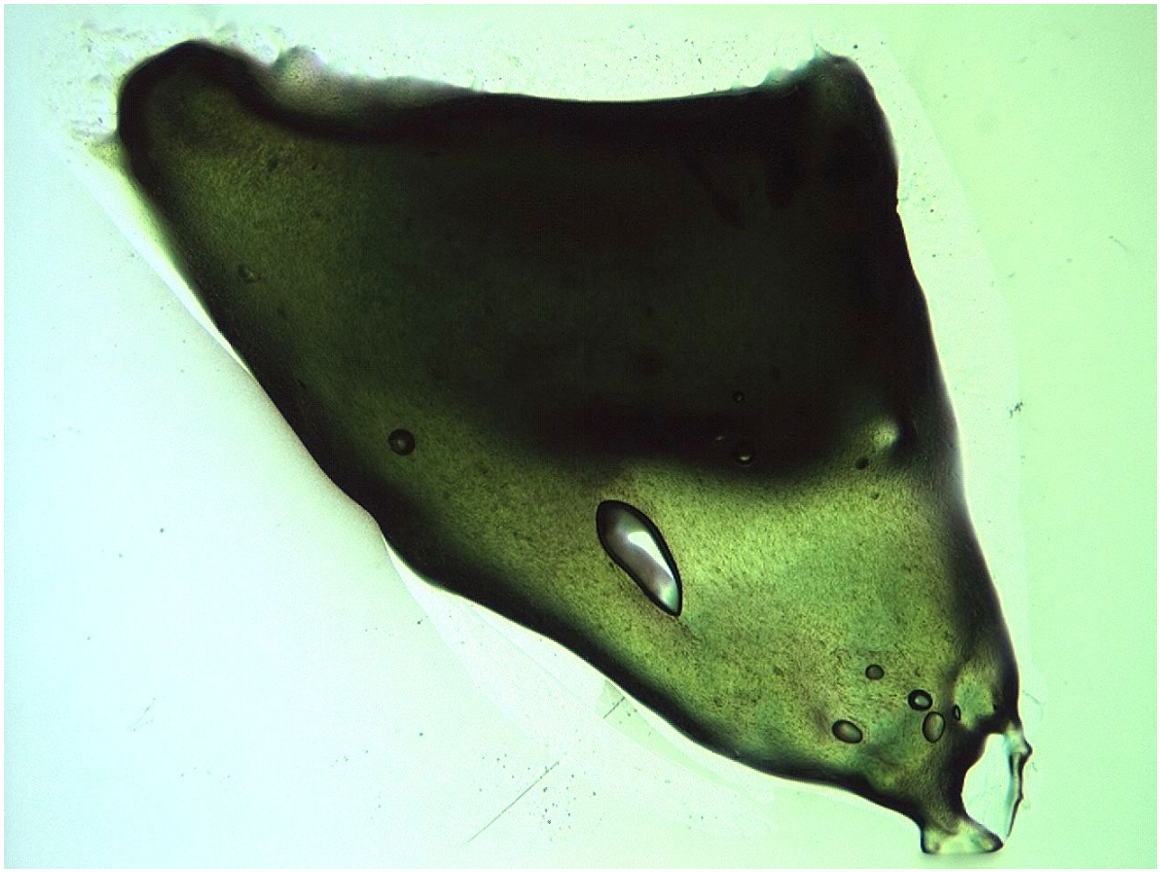

15% PEG 8 x 10^6 in water mixed with PS-I crystal solution:

SONICC signal